A Primer on Pulsed Power and Linear Transformer Drivers for High Energy Density Physics Applications

R. D. McBride, *Member, IEEE*, W. A. Stygar, *Member, IEEE*, M. E. Cuneo, *Fellow, IEEE*,

D. B. Sinars, *Senior Member, IEEE*, M. G. Mazarakis, *Life Member, IEEE*, J. J. Leckbee, *Member, IEEE*,

M. E. Savage, *Member, IEEE*, B. T. Hutsel, *Member, IEEE*, J. D. Douglass, *Member, IEEE*, M. L. Kiefer,

B. V. Oliver, *Fellow, IEEE*, G. R. Laity, *Member, IEEE*, M. R. Gomez, *Member, IEEE*,

D. A. Yager-Elorriaga, *Member, IEEE*, S. G. Patel, *Member, IEEE*, B. M. Kovalchuk, A. A. Kim,

P.-A. Gourdain, S. N. Bland, *Member, IEEE*, S. Portillo, *Member, IEEE*,

S. C. Bott-Suzuki, *Member, IEEE*, F. N. Beg, *Fellow, IEEE*, Y. Maron, *Fellow, IEEE*,

R. B. Spielman, *Member, IEEE*, D. V. Rose, D. R. Welch, *Member, IEEE*, J. C. Zier,

J. W. Schumer, *Senior Member, IEEE*, J. B. Greenly, A. M. Covington, A. M. Steiner, *Member, IEEE*,

P. C. Campbell, *Member, IEEE*, S. M. Miller, *Member, IEEE*, J. M. Woolstrum, *Member, IEEE*,

N. B. Ramey, *Member, IEEE*, A. P. Shah, B. J. Sporer, N. M. Jordan, *Member, IEEE*,

Y. Y. Lau, *Fellow, IEEE*, and R. M. Gilgenbach, *Life Fellow, IEEE*

(Invited Paper)

Abstract—The objectives of this tutorial are as follows: 1) to help students and researchers develop a basic understanding of how pulsed-power systems are used to create high-energy-density (HED) matter; 2) to develop a basic understanding of a new, compact, and efficient pulsed-power technology called linear transformer drivers (LTDs); 3) to understand why LTDs are an attractive technology for driving HED physics (HEDP) experiments; 4) to contrast LTDs with the more traditional Marx-generator/pulse-forming-line approach to driving HEDP experiments; and 5) to briefly review the history of LTD technology as well as some of the LTD-driven HEDP research presently underway at universities and research laboratories across the globe. This invited tutorial is part of the Mini-Course on Charged Particle Beams and High-Powered Pulsed Sources, held in conjunction with the 44th International Conference on Plasma Science in May of 2017.

Index Terms—Equation of state, high-energy-density physics (HEDP), inertial confinement fusion (ICF), laboratory astrophysics, linear transformer driver (LTD), magnetized liner inertial fusion (MagLIF), material properties, pulsed power, radiation effects, radiation science, radiation sources.

I. INTRODUCTION

HIGH-ENERGY-DENSITY PHYSICS (HEDP) is defined as the study of matter and radiation at extreme conditions, where the energy density is about 10^{11} J/m^3 or higher. Noting that the units of pressure *are* the units of energy density (i.e., 1 Pa = 1 N/m^2 = 1kg/(m · s^2) = 1 J/m^3), HEDP material pressures are often at or above 1 Mbar ($\approx$1 million atmospheres). To drive matter to such an extraordinary state requires a high-power, high-energy, high-pressure driver system. These systems often come in the form of large pulsed-power facilities or large laser facilities. Present state-of-the-art HEDP facilities include the Z Pulsed-Power Facility at Sandia National Laboratories [1], [2], the OMEGA and OMEGA-EP laser facilities at the University of Rochester's Laboratory for Laser Energetics [3], [4], and the National Ignition Facility (NIF) at Lawrence Livermore National Laboratory [5], [6]. These facilities support a variety of programs in stockpile stewardship and basic science. For example, the pulsed-power facilities at Sandia presently support stockpile stewardship experiments in inertial confinement fusion (ICF) [7]–[10], material properties [11], [12], radiation physics [13], [14], radiation effects testing [15], [16], and advanced radiography development [17], [18], as well as basic science programs in material properties [19], radiation physics [20], planetary science [21], and laboratory astrophysics [22].
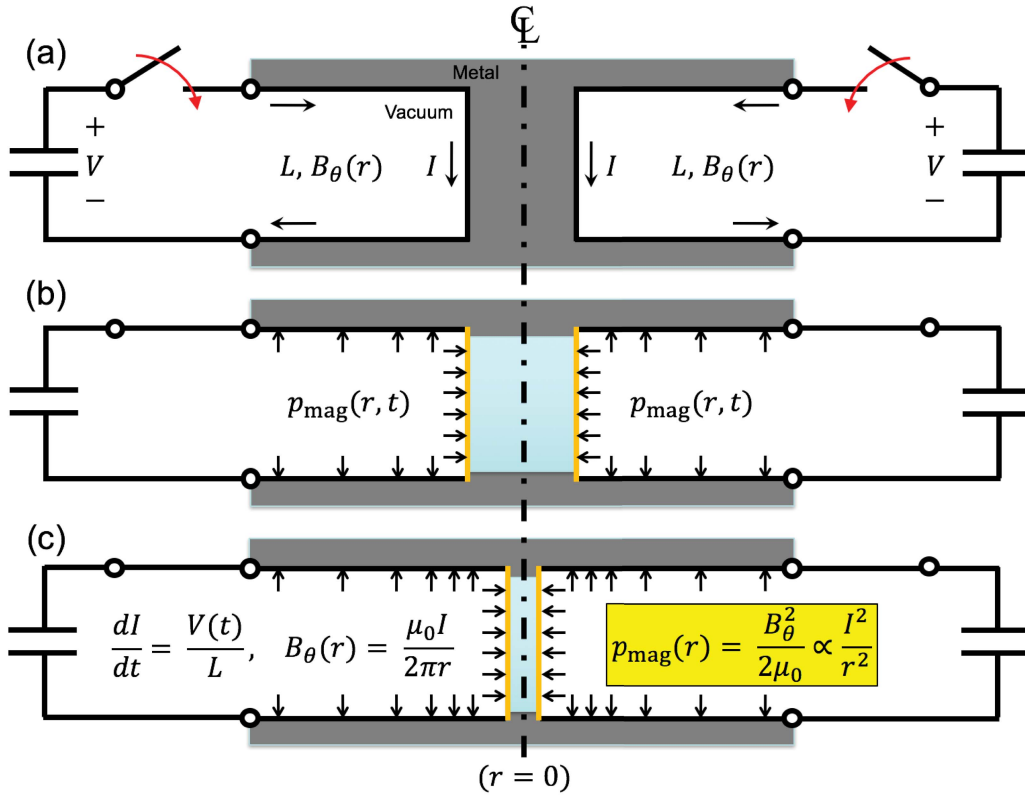
Fig. 1. Schematic illustration of a basic pulsed-power system discharging into a cylindrically symmetric, vacuum-filled metal cavity. As the switches close, a *surface* current ramps up at a rate $dI/dt = V/L$, where L is the inductance of the cavity (dependent on the volume and geometry of the cavity) and V is the discharge voltage. The cylindrically symmetric, radially converging current flow along the cavity's metal surfaces generates an azimuthal magnetic field $B_\theta(r) = \mu_0 I/(2\pi r)$. The $B_\theta(r)$ field permeates the vacuum region and is excluded from the metal regions because of the fast rise time of the current pulse, which is $\sim$100 ns in modern pulsed-power-driven HEDP experiments. The resulting magnetic pressure (i.e., the magnetic energy density) in the vacuum region is $p_{\mathrm{mag}} = B_\theta^2/(2\mu_0) \propto I^2/r^2$. This pressure can be used to drive a cylindrical implosion if the central metal stalk in (a) is hollowed out into the metal tube shown in (b) and (c) and the walls of the tube are thin enough (have a low enough mass) to be accelerated/imploded on the time scale of the current pulse $I(t)$.

In this tutorial, we will focus solely on pulsed-power technology for driving HEDP experiments. We will first establish a basic, general picture of a pulsed-power-driven HEDP experiment. We will then use this picture to understand a relatively new pulsed-power technology for HEDP called linear transformer drivers (LTDs) [23]–[38]. To provide a basis for comparison, we will also briefly describe the more traditional Marx-generator/pulse-forming-line approach to driving HEDP experiments. As we will see, LTDs offer compact, efficient, and fully enclosed packaging of the pulsed-power components (e.g., capacitors and switches) as well as a highly modular design to enable the construction of large LTD-based systems. Finally, we will briefly review the LTD's history and provide some examples of recent LTD-driven HEDP research from across the globe. It is our hope that the picture of pulsed-power-driven HEDP presented in this tutorial will complement the pictures presented previously in other similar review articles [39].

II. SIMPLE PICTURE OF A PULSED-POWER-DRIVEN HEDP EXPERIMENT

In its simplest form, a basic pulsed-power-driven HEDP experiment begins with a cylindrically symmetric, vacuum-filled, metal cavity [see Fig. 1(a)]. Around the perimeter of

this cavity, we want to apply a large voltage V in order to drive a very fast rising, high-amplitude current pulse $I(t)$. For simplicity, we will assume that the metal is perfectly conducting (which is a reasonable approximation in modern pulsed-power-driven HEDP experiments). We will also assume that all initial currents and magnetic fields are zero. Because the metal is perfectly conducting, the only thing that limits the electrical current (or more specifically the rise rate of the electrical current) is the inductance of the metal cavity, L. Later, we will show some simple techniques for evaluating L, but for now, it suffices to say that L depends on the volume and geometry of the cavity (generally L increases as the cavity volume increases and as the inner cylindrical radius of the cavity decreases). Now, since we are essentially applying a voltage to an inductor, we know from basic physics/circuits that $V = L(dI/dt)$, and thus the current will rise at a rate given by

$$\dot{I} \equiv \frac{dI}{dt} = \frac{V}{L}. \tag{1}$$

In modern pulsed-power-driven HEDP experiments, the current rise times are often $\sim$100 ns, and the electrodes are often made from materials such as stainless steel, aluminum, brass, copper, and gold. On 100-ns time scales, these materials have
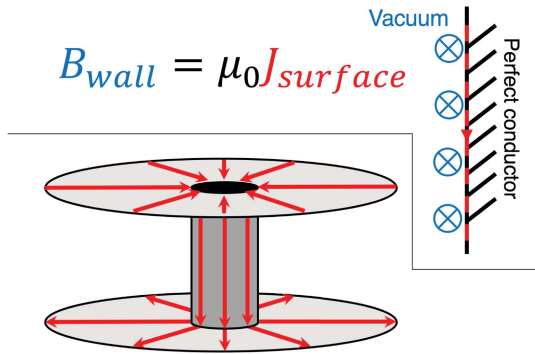
$$B_{wall} = \mu_0 J_{surface}$$

Fig. 2.   Illustration of how perfectly conducting boundary conditions and a radially convergent surface current density $\mathbf{J}_s(r)$ in cylindrical geometry lead to the expression in (3). The red arrows indicate the surface current density along the surface of the perfectly conducting metal, and the blue circles with crosses indicate the tangential magnetic field going into the page in the vacuum region immediately adjacent to the perfectly conducting metal surface. The magnetic field and current density inside the bulk of the perfect conductor is zero.

skin depths

$$\delta_{\text{skin}} = \sqrt{\frac{4\rho_e \tau_r}{\pi \mu_0}} \sim 100 \ \mu\text{m} \qquad (2)$$

where $\rho_e \sim 100$ n$\Omega \cdot$m is the electrical resistivity of the metal electrodes, $\tau_r \sim 100$ ns is the rise time of the driving current pulse, and $\mu_0 = 4\pi \times 10^{-7}$ H/m is the permeability of free space. In contrast with $\delta_{\text{skin}} \sim 100 \ \mu$m, the anode–cathode (A–K) gaps and imploding cylindrical targets in pulsed-power-driven HEDP experiments typically have spatial dimensions ~ 1 cm. Thus, the current pulse $I(t)$ is indeed a surface current, and the perfectly conducting electrode assumption is reasonable.

Because of the cylindrical symmetry assumption, the zero initial field assumption, and the perfect conductor assumption, the magnetic field generated by the rising current pulse is purely an azimuthal field that exists only in the vacuum regions of the cavity (i.e., this field is excluded from the metal regions). This field can be represented in the vacuum region as

$$\mathbf{B} = B_\theta(r)\hat{\boldsymbol{\theta}} = \frac{\mu_0 I}{2\pi r}\hat{\boldsymbol{\theta}}. \qquad (3)$$

This expression can be understood with the help of Fig. 2. Because of the perfect conductor boundary condition, we know from fundamental electricity and magnetism that the surface current density $\mathbf{J}_s$ (a linear current density in units of A/m running along the metal surface) is essentially equivalent to the value of the tangential magnetic field $\mathbf{B}$ at the metal surface (the equivalence is given through the proportionality constant μ_0, which is the magnetic permeability of free space—see Fig. 2). Additionally, we must keep in mind that for perfect conductors, the direction of the surface current density is perpendicular to the direction of the magnetic field at the metal surface ($\mathbf{J}_s \perp \mathbf{B}$) and that both $\mathbf{J}_s$ and $\mathbf{B}$ have only tangential components (their components normal to the metal surfaces are zero everywhere). Putting this all together, we have

$$B_\theta = \mu_0 J_{sz} \qquad (4)$$

where $\mathbf{J}_s = J_{sz}\hat{\mathbf{z}}$, and

$$B_\theta = \mu_0 J_{sr} \qquad (5)$$

where $\mathbf{J}_s = J_{sr}\hat{\mathbf{r}}$. Now, since we are supplying a total current I, the magnitude of the surface current density must be given by

$$J_s(r) = \frac{I}{2\pi r} \qquad (6)$$

so that integrating $J_s(r)$ over a circumference of $2\pi r$ correctly returns the known total current $I = J_s(r) \cdot 2\pi r$ (remember that J_s is a *linear* current density in units of A/m; it is not the standard areal current density in A/m^2). Plugging (6) into either (4) or (5) gives (3).

It is important to note that (3) does *not* require an infinitely thin, infinitely long, current carrying wire to be valid. Equation 3 only requires that the system be cylindrically symmetric and that the current I be the total current enclosed by a circle of radius r [i.e., $I = I_{\text{enclosed}}(r)$]. Pulsed-power drivers for HEDP applications are usually very cylindrically symmetric systems, so (3) is important to remember. For a more formal derivation of (3), see Appendix A.

One may recall from fundamental electrodynamics that there exists a force density $\mathbf{F} = \mathbf{J} \times \mathbf{B}$ (a force per unit volume), which is often referred to simply as the "*J cross B force*." This force density comes from the magnetic part of the Lorentz force equation ($\mathbf{F} = q\mathbf{v} \times \mathbf{B}$, where q is the electrical charge of a particle and $\mathbf{v}$ is the velocity of the charged particle) and summing over the motions of all the charged particles in the conductors ($\mathbf{J} = \sum_i n_i q_i \mathbf{v}_i$). Here, $\mathbf{J}$ is the standard (areal) current density in units of (C/s)/m^2 = A/m^2. Because we have assumed perfect conductors and zero initial fields, we know that we will always have $\mathbf{J} \to \mathbf{J}_s$ and $\mathbf{J}_s \perp \mathbf{B}$, and thus, from simple units analysis with $\mathbf{J} \to \mathbf{J}_s$, the $\mathbf{J} \times \mathbf{B}$ force density becomes a force per unit area, which is a pressure p. Using the right-hand rule, we find that this pressure is applied normal to the metal cavity surfaces in the direction from the vacuum region to the metal regions. This means that in Figs. 1 and 2, the top electrodes will be pushed upwards, the bottom electrodes will be pushed downwards, and the central cylindrical metal stalks will be compressed (or imploded) radially inwards. In other words, the vacuum region is pushing outward on all of the metal surfaces as if the vacuum region were pressurized. In fact, this phenomenon can be described in terms of a *magnetic pressure*. From fundamental electricity and magnetism, we know that the magnetic field has an associated energy density of $\mathcal{E}_B = B^2/(2\mu_0)$. And since energy density is equivalent to pressure (i.e., the units of pressure are Pa = J/m^3), we can write

$$p_{\text{mag}} = \frac{B^2}{2\mu_0}. \qquad (7)$$

For two alternative approaches to deriving (7), see Appendix B. Also note that, like the magnetic field, the electric field $\mathbf{E}$ has an associated energy density $\mathcal{E}_E = \epsilon_0 E^2/2$, where ϵ_0 is the electric permittivity of free space. However, the central metal stalk in the cavity is essentially a short-circuit load, and thus the electrical resistance/impedance is practically zero

at the stalk. This means that, near the stalk, the system is high current (high **B**) and low voltage (low **E**), and thus the magnetic field dominates the system dynamics.

If we now substitute (3) into (7), we find that

$$p_{\mathrm{mag}} = \frac{\mu_0 I^2}{8\pi^2 r^2} \propto \frac{I^2}{r^2}. \tag{8}$$

Thus, if we want to apply the highest pressures to objects of interest, then we need to get as much current as possible to as small of a radius as possible. This is especially important because (I/r) is squared in (8), and therefore the magnetic pressure diverges rapidly as $r \rightarrow 0$. Moreover, if the central cylindrical metal stalk is hollowed out and made into a tube with thin enough walls (walls with low enough mass), then this tube can be made to implode [see Fig. 1(b) and (c)]. This is referred to as a *fast Z-pinch* implosion [40], and the imploding metal tube is often referred to as an imploding *liner*. Furthermore, if one fills the tube with fusion fuel (i.e., either pure deuterium or deuterium-tritium mixtures), then this fuel can be compressed and heated by the imploding/converging metal liner. The fast (100-ns) imploding liner-fuel system can then be considered an ICF "*target*." Imploding a metal liner containing fuel is the technique employed by the magnetized liner inertial fusion (MagLIF) concept [7], [8] presently being investigated numerically [7], [8], [41]–[44] and experimentally [9], [10], [45]–[52] using the Z facility at Sandia.

As described by (8), when a liner implodes, $r(t) \rightarrow 0$, and the magnetic drive pressure at the liner's outer surface can grow very rapidly to extreme values. In MagLIF, drive pressures can well exceed 100's of Mbar (100's of millions of atmospheres). For example, on Z, when $I = 20$ MA and $r = 0.5$ mm, the magnetic drive pressure is $p_{\mathrm{mag}} = 250$ Mbar. To put this number into perspective, 140 Mbar is the radiation drive pressure produced on the NIF. This is one very important reason why imploding liner loads are attractive options for ICF targets.

The very large magnetic pressures that can be obtained by channeling very large current pulses to very small radii, particularly when employing implosion techniques, are useful not only to ICF concepts like MagLIF, but also to radiation source development and material properties experiments. For example, rather than imploding a metal liner, the cylindrical metal tube can be approximated by a cylindrical array of fine metal wires very closely spaced together (called a wire-array Z-pinch [15]) or an annular puff of gas (called a gas-puff Z-pinch [16], [53]). Due to the intense heating from the electrical current pulse, these approximately cylindrical loads quickly vaporize and ionize into conducting plasma channels (at least near the radially outermost regions). Like metals, these plasma tubes can conduct large currents and significantly exclude the driving magnetic field from penetrating the tube's interior. Wire-array Z-pinches and gas-puff Z-pinches are primarily used for generating X-rays (and sometimes neutrons, in the case of deuterium gas-puff Z-pinches). The radiation is produced when the imploding plasma tube stagnates on itself near the cylindrical axis of symmetry (near $r = 0$). At this point, the plasma kinetic energy is converted into thermal energy, while the magnetic pressure continues to

drive plasma compression (further heating the plasma), to the point where X-ray generation is excited (and/or fusion neutron events become probable). This X-ray (and sometimes neutron) radiation is then used in HEDP experiments that are designed to study fundamental radiation transport processes (e.g., measuring the X-ray transmission and opacity of materials at extreme temperatures and densities) and to test the radiation "hardness" of various electronics equipment (i.e., radiation effects testing). This self-pinching effect can also be used to generate radiation for advanced radiographic capabilities [17]; these capabilities are then used to image HEDP experiments.

In material properties experiments, cylindrically converging/imploding liners have been used to obtain measurements at some of the highest material pressures to date. In these imploding experiments, the material sample *is* the metallic liner (or is at least part of a composite multimaterial liner). For example, cylindrically imploding liner techniques have been used to probe the equation of state in Be out to 5.5 Mbar [11] and in Ta, Cu, and Al out to 10 Mbar [12].

As mentioned above, the magnetic pressure pushes outward on all of the metal cavity surfaces. The fact that this pressure wants to compress or implode the central metal stalk is merely a consequence of the cylindrically convergent and/or coaxial geometry of the cavity. In fact, to meet various experimental objectives, pulsed-power-driven HEDP experiments can be executed where the objects of interest are placed in either the imploding or exploding portions of the cavity. Above, we discussed examples of imploding objects of interest (or "*targets*"), and, to be sure, implosions are the way to access the highest drive pressures. However, there are times when one desires: 1) more spatially uniform magnetic field pressures; 2) diverging plasma flows; and/or 3) better diagnostic access. In these cases, exploding experimental geometries can be (and are) used (see Fig. 3) [19], [21].

The pulsed-power-driven techniques discussed above can also be used to drive HEDP experiments to study laboratory astrophysics [20], [22] and other fundamental science [19], [21]. For example, to drive laboratory astrophysics experiments, the wires in a cylindrical wire-array Z-pinch can be angled to form a *conical* wire array [54]. The conical angle is obtained, for example, by having the wires connect to a larger radius on the top electrode than on the bottom electrode. With this configuration, the magnetic pressure accelerates the plasma radially inwards as well as axially upwards. As the plasma collects on axis, the residual axial momentum leads to the formation of axial plasma jets (upwards in our example). The plasma jets produced can be used to emulate astrophysical jets. Similarly, if the uppermost horizontal portion of the electrode structure shown in Fig. 3 (where the magnetic pressure pushes upwards on the electrode structure) is replaced with thin wires, then a *radial* wire array is formed [55]. If the wires of a radial wire array are replaced with a thin foil, then a *radial foil* is formed [56]–[59]. Any of these configurations (conical wire arrays, radial wire arrays, or radial foils) can be used to accelerate plasmas axially and to create plasma jets that can be used to study astrophysical jets. One final configuration that should be mentioned is the *inverse* (or *exploding*) wire array [60]. If the material sample in the exploding portion

For axial plasma jet experiments, replace these uppermost electrode sections with radial (spoke-like) wires for a "radial" wire array load or with a thin foil for a "radial foil" load

Velocimetry/Doppler Fibers

Receive Fiber

Send Fiber

Material Sample for a Material Properties Experiment

(Replace material sample with many thin vertical wires for an "inverse" wire-array load for a lab astrophysics experiment)

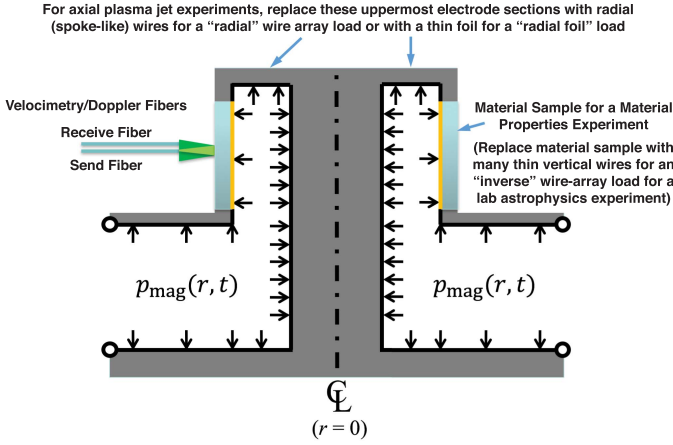$p_{\text{mag}}(r,t)$ $p_{\text{mag}}(r,t)$

$\mathcal{CL}$

$(r = 0)$

Fig. 3. Illustration of a pulsed-power-driven experiment in an exploding configuration. This setup is similar to that used in planar dynamic material properties experiments, where the material sample under test is placed in the coaxial "return-current" path. The material sample's response to the pressure pulse (e.g., its motion) is tracked using fiber-based Doppler velocimetry techniques. The elevated coaxial pedestal allows for diagnostic access and for a uniform magnetic pressure to be applied to the sample (since $p_{\text{mag}} = p_{\text{mag}}(r) = B_\theta^2(r)/(2\mu_0)$ and $r = $ constant along the sample height). This figure also illustrates how the electrode hardware can be modified to drive a radial wire-array load, a radial foil load, or an inverse wire-array load, which are load configurations often used for laboratory astrophysics experiments.

(in the "return-current" portion) of Fig. 3 is replaced with thin wires, then an inverse wire array is formed. If the wires are thick enough so that they don't move on the time scale of the experiment, then they can be used to supply steady streams of outward flowing ablated plasma. Two such inverse wire-arrays, with their ablation streams directed towards one another, have been used recently to drive magnetic reconnection experiments on the MAGPIE generator at Imperial College London [61].

All of the applications discussed above, including both programatic/defense-related missions and fundamental science, depend on *pulsed-power technology*. By pulsed-power technology, we mean the arrangement of switches and capacitors used to drive the voltage and current pulses into the inductive cavities shown in Figs. 1–3. We will discuss two different arrangements of switches and capacitors in Sections IV and V, but before doing this, we first review a simple LC model of a generic pulsed-power system.

III. Simple LC Model of a Generic Pulsed-Power System

Related to our discussion on driving an inductive cavity in Section II, we will want to keep the following in mind to achieve the highest pressures.

1) To pump energy $\mathcal{E}$ into the cavity as fast as possible (to obtain a high energy density), we need to generate a large electrical power P_{electric}. This means that we need to generate both high voltage V and high current I because

$$\frac{d\mathcal{E}}{dt} = P_{\text{electric}} = V \times I.$$

2) We need lots of stored charge Q, because $I = dQ/dt$.

3) We need lots of charge storage capacity (capacitance) C, because $Q = CV$.

4) Since capacitance adds in parallel, we need many storage capacitors n, each with a capacitance C_i, arranged in parallel to get $C = nC_i$. To visualize this arrangement, think of two huge parallel metal plates, each with a surface area A, separated by a small A–K gap spacing d that is filled with a dielectric material with a permittivity of ϵ. These huge metal plates could be broken up into smaller sections, each with a surface area A_i and a gap spacing of d, to get

$$C = \frac{\epsilon A}{d} = n\frac{\epsilon A_i}{d} = nC_i. \tag{9}$$

5) From (1) ($dI/dt = V/L$), we need a small inductance L.

The question now becomes: how do we evaluate and minimize L? We can actually evaluate L two different ways. Referring to Fig. 1, the first way is to integrate the flux density, B_θ, over the cross-sectional area A of the vacuum region of the cavity to get the total azimuthal flux

$$\Phi = \int_A \mathbf{B} \cdot d\mathbf{A} = \int_{r_{\text{in}}}^{r_{\text{out}}} \int_0^h \left(\frac{\mu_0 I}{2\pi r}\right) dz \, dr$$
$$= \frac{\mu_0 I h}{2\pi} \int_{r_{\text{in}}}^{r_{\text{out}}} \frac{1}{r} \, dr$$
$$= \frac{\mu_0 I h}{2\pi} \ln\left(\frac{r_{\text{out}}}{r_{\text{in}}}\right). \tag{10}$$

Then, by definition, the inductance is given by

$$L \equiv \frac{\Phi}{I} = \frac{\mu_0 h}{2\pi} \ln\left(\frac{r_{\text{out}}}{r_{\text{in}}}\right). \tag{11}$$

The second way to calculate L is to integrate the magnetic energy density, $B_\theta^2/(2\mu_0)$, over the entire volume V of the cavity's vacuum region to get the total magnetic energy stored in the cavity

$$\mathcal{E}_B = \int_V \left(\frac{B^2}{2\mu_0}\right) \cdot dV$$
$$= \int_{r_{\text{in}}}^{r_{\text{out}}} \int_0^{2\pi} \int_0^h \frac{1}{2\mu_0} \left(\frac{\mu_0 I}{2\pi r}\right)^2 \cdot r \, d\theta \, dr \, dz$$
$$= \frac{1}{2\mu_0} \frac{\mu_0^2 I^2}{4\pi^2} \cdot 2\pi h \int_{r_{\text{in}}}^{r_{\text{out}}} \frac{1}{r} \, dr$$
$$= \frac{\mu_0 h I^2}{4\pi} \ln\left(\frac{r_{\text{out}}}{r_{\text{in}}}\right). \tag{12}$$

Then, by equating this expression to the defining expression for the magnetic energy stored in an inductor, we have

$$\frac{1}{2}LI^2 \equiv \mathcal{E}_B = \frac{\mu_0 h I^2}{4\pi} \ln\left(\frac{r_{\text{out}}}{r_{\text{in}}}\right) \tag{13}$$

$$\Rightarrow L = \frac{\mu_0 h}{2\pi} \ln\left(\frac{r_{\text{out}}}{r_{\text{in}}}\right). \tag{14}$$

Thus, these two methods for calculating L return the same result, which is always the case if the current is a surface current. If the current is distributed in the metal, then care
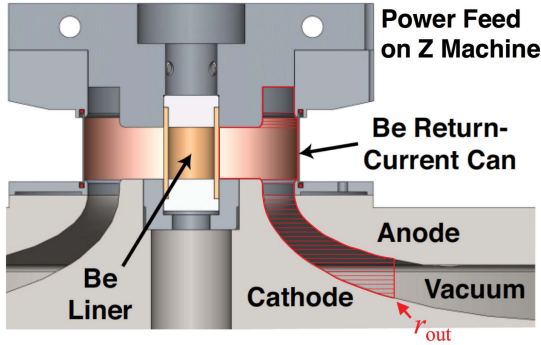
Fig. 4. Illustration of the final power feed and a cylindrical liner load on the Z machine. The overlaid red lines illustrate how, in regions with large slopes or curvatures (i.e., large dr/dz and/or large d^2r/dz^2), we can break up the power feed into slices with very short dz so that we can calculate dL and L using (15). (Source: [47] and [48].)

Fig. 5. A simple LC circuit model that can be used to describe the process of pulsing the inductive cavity shown in Fig. 1. For $t < 0$, the switch is open and the capacitor is charged to V_0. For $t > 0$, the switch is closed and the system discharges into L. Because there are no dissipative elements, the energy simply oscillates back and forth between the capacitor (voltage/electric field energy) and the inductor (current/magnetic field energy). The system is an LC resonant circuit, with a resonant frequency of $\omega = 1/\sqrt{LC}$.

must be taken to interpret these two methods correctly, as they will not generally give the same result [42].

Note that this inductance L is simply the inductance of a coaxial transmission line [62], assuming that: 1) $\mu = \mu_0$; 2) the metal is perfectly conducting; and 3) the length of the line is the height h of our vacuum cavity. Also note that this result depends somewhat arbitrarily on where we set r_{in}, r_{out}, and h. In fact, by manipulating these limits, we can break up an inductance calculation into pieces and then sum the pieces to get the total. Of course, to calculate/simulate an actual circuit response, we are going to need the total inductance, meaning, we are going to need to account for every bit of flux generated in the current loop that includes everything from the source capacitors to the load. Nevertheless, the point here is that we can break up the total inductance *calculation* into pieces [63].

As an example of why this is useful, particularly for azimuthally symmetric systems, consider the image presented in Fig. 4. In (11) and (14), we can let h become arbitrarily small, so that $h \rightarrow dh \rightarrow dz$, and thus we can rewrite (11) and (14) as

$$L = \frac{\mu_0 h}{2\pi} \ln\left(\frac{r_{out}}{r_{in}}\right) \Rightarrow dL = \frac{\mu_0}{2\pi} \ln\left(\frac{r_{out}}{r_{in}}\right) dh$$

$$L = \int_{z_1}^{z_2} dL = \frac{\mu_0}{2\pi} \int_{z_1}^{z_2} \ln\left[\frac{r_{out}(z)}{r_{in}(z)}\right] dz. \quad (15)$$

Thus, as long as the anode and cathode curves, $r_{out}(z)$ and $r_{in}(z)$, are known, and as long as the feed is azimuthally symmetric, we can easily evaluate L using a simple computer algorithm. Note the arbitrary reference point labeled as r_{out} in Fig. 4. A circuit simulation would of course require the total inductance for everything upstream and downstream of r_{out} in Fig. 4. The upstream inductance (i.e., the "*machine inductance*") could be quite involved; however, this value likely doesn't change from one experiment to the next, and thus this inductance only needs to be evaluated once (perhaps using experimental measurements or a sophisticated 3-D simulation code). The downstream inductance (i.e., the "*load inductance*") could change quite significantly from one experiment to the next, with different custom hardware and/or targets being installed to meet various experimental objectives. Thus, the utility of this calculation technique is
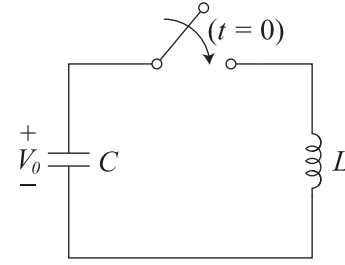
that the inductance budget for a new experimental load design can be rapidly evaluated and an experiment can be simulated with a full circuit model simply by summing the load and machine inductances. Note, however, that care must be taken to ensure that the proper handoff/reference point is being used (i.e., r_{out} in Fig. 4). This requires good communication between machine engineers and load/target designers.

To minimize L, there are a few things to consider. The first and easiest thing to keep in mind is that one always wants to minimize the overall axial translation Δz. Second, if a Δz translation must be done (e.g., to provide diagnostic access to the load), then it is often best to locate the Δz translation at a large radius to reduce the associated increase in inductance. To understand why this is the case, consider (11) and (14) and evaluate $L(r_{in})$ for a constant A–K gap spacing $d = r_{out} - r_{in}$ and a constant/given $\Delta z = h$; the inductance will be smaller at larger r_{in}. Third, if a combination of axial Δz and radial Δr translation must be done, then a *curved* power feed that is optimized for minimal inductance can be found using (15) [64], [65]. Optimized power feeds are often evaluated while simultaneously considering several other design constraints (e.g., avoiding other experimental equipment and/or diagnostics). More often than not, though, a simple *conical* power feed is not far from the optimum and in fact works quite well in practice [66].

At this point, we have L, C, and V, but we still need to calculate $I(t)$. To do this, we use the simple LC circuit shown in Fig. 5. For the simplicity of this tutorial, we will assume that the circuit's electrical resistance is zero ($R = 0$) and that $L = $ constant $\neq L(t)$. As we will see in Section V, this simple LC model is very useful for describing an LTD.

To solve this circuit for time $t > 0$, we begin by writing the voltage across the inductor. From basic physics/circuits [and/or (1)], we know this to be

$$V = L\dot{I}. \quad (16)$$

Next, the displacement current "through" the capacitor is

$$I = -C\dot{V}. \quad (17)$$

Differentiating the capacitor current with respect to time gives

$$\dot{I} = -C\ddot{V}. \quad (18)$$

Plugging this result for $\dot{I}$ back into (16) gives

$$V = (-LC)\ddot{V}. \tag{19}$$

This is just the equation for a simple harmonic oscillator, which has the solution

$$V = V_0 \cdot \cos(\omega t). \tag{20}$$

This solution can be verified by differentiating with respect to time once and twice to get

$$\dot{V} = -\omega V_0 \cdot \sin(\omega t) \tag{21}$$
$$\ddot{V} = -\omega^2 V_0 \cdot \cos(\omega t) = -\omega^2 V \tag{22}$$

which matches (19) above, with the circuit's resonant frequency given by

$$\omega = \frac{1}{\sqrt{LC}}. \tag{23}$$

Now, to evaluate the current pulse $I(t)$, we simply plug (21) into (17) to get

$$I = -C \cdot [-\omega V_0 \cdot \sin(\omega t)] \tag{24}$$
$$= \frac{C}{\sqrt{LC}} \cdot V_0 \cdot \sin(\omega t) \tag{25}$$
$$= \sqrt{\frac{C}{L}} \cdot V_0 \cdot \sin(\omega t) \tag{26}$$
$$= I_{\text{peak}} \sin(\omega t). \tag{27}$$

Summarizing our solution, we have a simple harmonic oscillator with the following relationships:

$$I(t) = I_{\text{peak}} \sin(\omega t) \tag{28}$$
$$I_{\text{peak}} = V_0 \sqrt{\frac{C}{L}} = \frac{V_0}{Z_0} \tag{29}$$
$$Z_0 \equiv \sqrt{\frac{L}{C}} \tag{30}$$
$$\omega = 2\pi f = 2\pi/\tau = 1/\sqrt{LC} \tag{31}$$
$$\tau = 2\pi\sqrt{LC} \tag{32}$$
$$\tau_{\text{peak}} = \tau/4 = \frac{\pi}{2}\sqrt{LC}. \tag{33}$$

Here, Z_0 is the system's characteristic impedance, I_{peak} is the peak current obtained, τ is the full-cycle time period of the resonant oscillation, and τ_{peak} is the current rise time (i.e., the time to the first current peak in the resonant oscillation). The results of this solution are plotted in Fig. 6.

Because we neglected R and made $L = $ constant $\neq L(t)$, there is no energy dissipation or absorption, and thus this solution will oscillate forever. In real HEDP experiments, the resistance can indeed be small and the inductance can indeed be approximately static in some cases (e.g., material property experiments where small material samples are only slightly compressed/deformed). This situation can stress the components of a pulsed-power system, because the oscillating energy will keep revisiting particular components continually until the energy eventually dissipates. One example is that the storage capacitors and switches can be stressed by electric fields in ways that they were not designed for; this can be particularly problematic upon voltage reversal ($V = -V_0$,
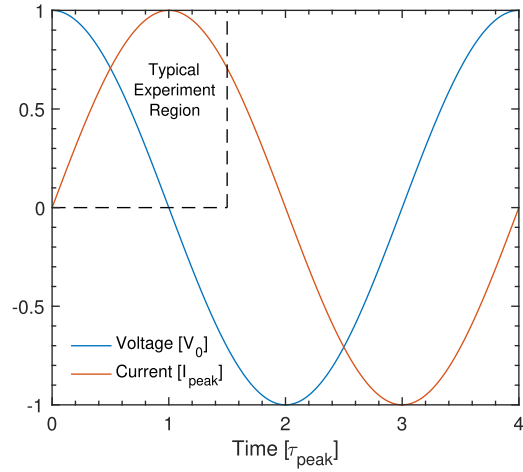

Fig. 6. The response of the circuit model in Fig. 5 for $t > 0$. The voltage and current values are in units of V_0 and I_{peak}, respectively, while the time values are in units of τ_{peak}. Note that a pulsed-power-driven HEDP experiment will typically only use the current's first rising edge and first peak; however, we plot a full period of oscillation simply to illustrate that with negligible resistance and/or material motion to dissipate and/or absorb the energy, the energy will simply oscillate back and forth between electric and magnetic fields (voltage and current); i.e., the system is resonant, and thus it will "ring" without energy dissipation and/or absorption.

at $t = 2\tau_{\text{peak}}$, in Fig. 6). Additionally, the components must support large currents (and potentially large ohmic heating) repeatedly as the current continuously flows back and forth.

If, on the other hand, our HEDP experiment involves a resistance R or a time-dependent inductance $L(t)$, then we will have energy dissipation, absorption, and conversion mechanisms that will pull energy out of the resonant LC circuit and damp the oscillations presented in Fig. 6. A dynamic $L(t)$ will arise in HEDP experiments because of material acceleration, which changes the geometry of the current carrying cavity. Note that because of $L \to L(t)$, we will also have $\dot{L} \neq 0$.

In the case of a cylindrical thin-shell implosion, the correspondence from material motion $r(t)$ to inductance $L(t)$ is given by (11) and (14) with $r_{\text{in}} \to r(t)$. By differentiating (11) and (14) with respect to time, we find a similar correspondence between $\dot{L}(t)$ and the radial implosion velocity $v(t) = \dot{r}(t)$, namely,

$$\dot{L} = -\frac{\mu_0 h}{2\pi}\left[\frac{\dot{r}(t)}{r(t)}\right]. \tag{34}$$

To evaluate $r(t)$, we use the driving azimuthal magnetic field (3) and the resulting magnetic pressure (7) and (8), operating on a cylindrical surface area $A_{\text{cyl}} = 2\pi r \cdot h$, to write an expression for the radial implosion force F_r and the radial acceleration $\ddot{r}$

$$F_r = m\ddot{r} = -p_{\text{mag}} \cdot A_{\text{cyl}} = -\left(\frac{B_\theta^2}{2\mu_0}\right) \cdot 2\pi r \cdot h$$
$$= -\left(\frac{\mu_0 I^2}{8\pi^2 r^2}\right) \cdot 2\pi r \cdot h$$
$$= -\frac{\mu_0 h I^2}{4\pi r}. \tag{35}$$

This equation is coupled to the circuit model above via $I(t)$. Additionally, because $L \rightarrow L(t)$, we must replace (16) in the circuit model above with a more general expression. That is, from the first of our two definitions of inductance (11), we have

$$L \equiv \frac{\Phi}{I} \Rightarrow \Phi = LI. \qquad (36)$$

Then, from Faraday's law, we have

$$V_L = \dot{\Phi} = \frac{d}{dt}(LI) = \dot{L}I + L\dot{I}. \qquad (37)$$

Again, care must be taken when applying (11) and (36) [and (13)]—the two methods/definitions used to derive L in these equations will produce equivalent expressions for L only when the current is a surface current, as in our present example. When the current is distributed in a conductor, the two methods are both still needed, but their interpretations change. For example, the second method (the integral of the magnetic energy density) will lead to a result where $V_L \neq \dot{L}I + L\dot{I}$; however, this method will still provide a useful expression for evaluating the rate of change of magnetic field energy in the system. The reason the two methods no longer give equivalent results is because the first method (the integral of the flux density) also includes ohmic heating contributions (note that ohmic heating must occur whenever a current is diffusing into a resistive material and is thus spatially distributed). For an example of how to use these definitions when the current is distributed in resistive metals/plasmas, see [42].

This coupled system of ordinary differential equations [(17), (35), and (37)] can then be solved numerically to find the driving voltage and current waveforms, $V(t)$ and $I(t)$, respectively, and the implosion trajectory $r(t)$ for a thin-walled, hollow cylindrical shell. Note that since the implosion's mechanical (kinetic) energy is $\mathcal{E}_{\mathrm{mech}} = (1/2) \, mv^2 = (1/2)m\dot{r}^2$, where m is the mass of the liner, and since $\dot{r}$ is related to $\dot{L}$ through (34), this cylindrical thin-shell example illustrates why $\dot{L}$ is important when considering the overall energetics of the system. A great deal of insight can be gleaned by working with and studying this model. This can be accomplished by writing a short numerical code to solve (17), (35), and (37). This exercise is strongly encouraged for interested students and researchers; it is especially recommended for those actively pursuing research in the area of pulsed-power-driven HEDP.

From (37), we see that, mathematically, $\dot{L}$ looks just like a resistance R. That is, the first term on the far right-hand side (RHS) of (37) ($\dot{L}I$, referred to as the "L-dot" voltage) is analogous to Ohm's law ($V_\Omega = IR$), with $\dot{L}$ analogous to R. In the case of $\dot{L}$, energy is partially converted into directed mechanical energy (e.g., the radial kinetic and/or compressional energy of a cylindrical Z-pinch implosion) and partially converted into the new magnetic field that must be generated to fill the changing volume/geometry of the cavity as the current-carrying cavity surfaces move (e.g., implode). In the case of R, energy is scattered by charge carriers colliding with other charge carriers and/or lattice atoms, which results in randomized particle motion and thus thermalized ohmic

heating. In both cases, the energy conversion rates from the pulsed-power machine's total supplied electromagnetic energy can be described similarly. For R, we have the familiar ohmic heating rate given by

$$P_\Omega = \frac{d\mathcal{E}_\Omega}{dt} = V_\Omega I = I^2 R. \qquad (38)$$

For the total inductive voltage, we have

$$P_L = \frac{d\mathcal{E}_L}{dt} = V_L I = \dot{L}I^2 + L\dot{I}I. \qquad (39)$$

The second term on the far RHS of (39) is the power associated with increasing the electrical current, assuming that $L(t)$ is held fixed for that particular instant in time (i.e., this is the power required to increase the magnetic field energy within the cavity assuming that the volume and geometry of the cavity are held constant at that particular instant in time). By contrast, the first term (i.e., the $\dot{L}$ power term) is the energy conversion rate given a fixed current, and it is due solely to material motion (i.e., it is due to the rate of change of the vacuum cavity's volume and shape). This term gives an expression similar to P_Ω, namely,

$$P_{\dot{L}} = \frac{d\mathcal{E}_{\dot{L}}}{dt} = \dot{L}I^2. \qquad (40)$$

Additionally, this energy conversion rate $P_{\dot{L}}$ is further equipartitioned into two distinct channels: 1) into new magnetic field and 2) into directed mechanical energy associated with the material acceleration and/or compression. This equipartitioning results in the following energy conversion rates:

$$P_{B_{\mathrm{new}}} = \frac{d\mathcal{E}_{B_{\mathrm{new}}}}{dt} = \frac{1}{2}P_{\dot{L}} = \frac{1}{2}\dot{L}I^2 \qquad (41)$$

$$P_{\mathrm{mech}} = \frac{d\mathcal{E}_{\mathrm{mech}}}{dt} = \frac{1}{2}P_{\dot{L}} = \frac{1}{2}\dot{L}I^2. \qquad (42)$$

Here, $P_{B_{\mathrm{new}}}$ is the rate of energy conversion into new magnetic field because of the material motion (i.e., the rate at which magnetic field energy must be generated to fill the growing volume of the vacuum cavity) while P_{mech} is the rate of energy conversion into the directed mechanical energy of the accelerating and/or compressing material itself—e.g., for the case of an accelerating thin shell (with no material compression), we have $P_{\mathrm{mech}} = (d/dt)(mv^2/2)$, where m is the material mass and v is the material velocity (note that for a radial Z-pinch implosion in cylindrical geometry, we have $v = dr/dt \equiv \dot{r}$).

To understand where this equipartition comes from, consider the following, which was inspired by a derivation found in [67]. The total inductive power supplied to the cavity is given by P_L in (39). Referring to (13), the total energy contained in the magnetic field at any time is given by

$$\mathcal{E}_B = \frac{1}{2}LI^2 \qquad (43)$$

and thus, with $L \rightarrow L(t)$, the rate of change of the total energy stored in the magnetic field is given by

$$P_B = \frac{d\mathcal{E}_B}{dt} = \frac{d}{dt}\left(\frac{1}{2}LI^2\right). \qquad (44)$$

Therefore, the inductive power going into just the mechanical channel (i.e., the material acceleration and/or compression channel) is given by

$$P_{\text{mech}} = P_L - P_B \tag{45}$$

$$= \dot{L}I^2 + L\dot{I}I - \frac{d}{dt}\left(\frac{1}{2}LI^2\right) \tag{46}$$

$$= \dot{L}I^2 + L\dot{I}I - \frac{1}{2}\dot{L}I^2 - LI\dot{I} \tag{47}$$

$$= \frac{1}{2}\dot{L}I^2 \tag{48}$$

$$= \frac{1}{2}P_{\dot{L}}. \tag{49}$$

Since one half of the available $P_{\dot{L}}$ power goes into P_{mech}, the remaining half of $P_{\dot{L}}$ goes into $P_{B_{\text{new}}}$ (i.e., into generating new magnetic field to fill the newly accessible cavity volume). Therefore, in summary, we have

$$P_{\text{mech}} = P_{B_{\text{new}}} = \frac{1}{2}P_{\dot{L}}. \tag{50}$$

Note that, for a system like MagLIF, the imploding liner is used to compress a substance contained within the liner (e.g., the fusion fuel inside of a MagLIF liner). This requires compressional "pdV" work to be done on the substance, where p is the pressure of the substance, and dV is the change in the volume of the substance. It is important to understand that P_{mech} already accounts for the rate at which electromagnetic energy is being converted into compressional work. For example, the backpressure of the compressing substance could be large enough to stall the continuous radial acceleration of the imploding liner, leading to a constant-velocity implosion ($\dot{r}$ = constant, and $\ddot{r} = 0$). In this case, P_{mech} is solely the rate at which pdV work is being done to compress the substance. This can be understood by considering the fact that the liner's implosion kinetic energy ($(1/2)m\dot{r}^2$) is constant, and therefore the rate at which the supplied electromagnetic energy is being converted into the kinetic energy of the imploding liner shell is zero. This means that the supplied electromagnetic power $P_{\text{mech}} = (1/2)P_{\dot{L}} = (1/2)\dot{L}I^2 > 0$ must instead be going into the compressional pdV work that is being done on the enclosed substance.

In 1-D simulations of MagLIF (e.g., [7], [42], and [43]), the fuel pressure at stagnation can become large enough to both stall and reverse the liner implosion against the driving magnetic pressure (i.e., near $r = 0$, the liner can "bounce" off of the fuel pressure and explode radially outward). Note that during this explosion, the fuel pressure actually does work on the driving magnetic field and circuit, which leads to an increase in the driver current! That is, the exploding liner performs *magnetic flux compression* (MFC) on the driving B_θ field, which increases B_θ and thus increases the corresponding drive current I via (3).

The phenomenon of explosively driven MFC is described in detail in [68]. In short, consider a system where the magnetic flux is held constant (i.e., $\Phi = LI$ = constant). When the applied magnetic pressure dominates the system dynamics, the cavity volume (see Figs. 1–3, for example) will increase by pushing the liner radially inwards, the top and

bottom electrodes upwards and downwards, respectively, and the return current conductors radially outwards. The increasing cavity volume corresponds to an increasing cavity inductance, L. This means that the current I will drop because $I = \Phi/L$ and Φ = constant. However, if a competing pressure source (e.g., the MagLIF fuel pressure at stagnation) dominates over the applied magnetic pressure, then the conductors could move in the opposite directions, thus decreasing the cavity volume, reducing the system inductance, and increasing the current— this is the principle of MFC for current amplification. This principle is used by explosively driven MFC generators to produce currents of up to 300 MA [68]! This principle is also used in MagLIF, where a flux compressed axial magnetic field is used to keep the hot fusion fuel thermally insulated from the cold liner wall that surrounds the fuel—for more information on MFC in MagLIF, see [7] and [69].

Returning to our discussion above on energy partitioning, we note that, for a system like MagLIF, the liner is usually not a thin-walled cylindrical shell. Instead, the imploding liner is a thick-walled tube, where the walls of the tube undergo material compression as the liner implodes. It is important to understand that this material compression is also accounted for by P_{mech}. In summary, P_{mech} accounts for the rate at which the supplied electromagnetic energy is being converted into the implosion kinetic energy of the liner shell and into the compressional work that is being done on both the liner wall and the substance/fuel contained within the liner. For all of these cases, the equipartitioning represented by (50) is valid. For more details on this, see [42].

From the discussion above, we see that if we have either a resistance R or a dynamic inductance $L(t)$, then we will have energy dissipation, absorption, and conversion mechanisms that will pull energy out of the resonant LC circuit and damp the oscillations presented in Fig. 6. For example, in cylindrical liner implosions, the initial liner radius and mass are usually chosen such that the liner walls reach the axis of symmetry ($r = 0$) at $t = \tau_{\text{peak}}$, so that the drive current is maximal when the liner implosion stagnates (i.e., $I = I_{\text{peak}}$ when $r = 0$). However, the rapidly growing $L(t)$ (and large $\dot{L}$) due to the rapidly decreasing $r(t)$ (and large $-\dot{r}$) can result in an "inductive dip" in the current pulse, where, just prior to τ_{peak}, the amplitude of the current waveform is rapidly reduced to a value that is significantly lower than that of I_{peak} in the static inductance case. Furthermore, as noted above, if the implosion process reverses (i.e., if the liner bounces and/or explodes radially outward), then work is done on the magnetic field, which rapidly increases the drive current (i.e., the exploding liner rapidly reverses the inductive dip). An extreme and idealistic (but illustrative) example of an inductive dip followed by current amplification is provided in Fig. 7, which is from a 1-D simulation of MagLIF on a conceptual future accelerator with a nominal $\sim$50-MA peak current [43]. The pressure generated by the powerful fusion reactions explodes the liner radially outward, which compresses the magnetic flux of the driving B_θ field, thus increasing B_θ and amplifying the current via (3).

In general, solving a system with a dynamic $L(t)$, $R(t)$, and/or material compression usually requires a numerical treatment. For a detailed example of a thick-walled MagLIF
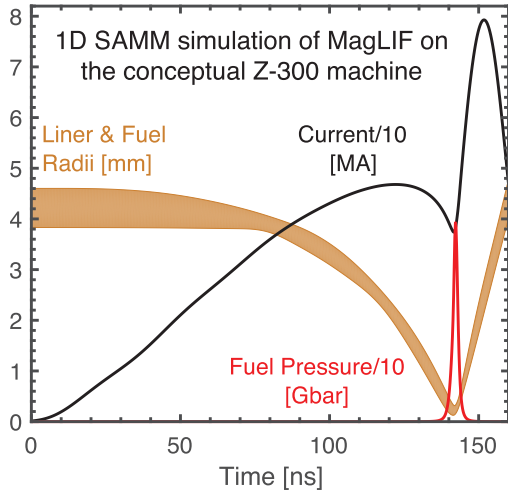
Fig. 7. An extreme and idealist (but illustrative) example of an "inductive dip" followed by current recovery and current amplification in a nominally 50-MA drive current. This example is from a 1-D SAMM simulation of MagLIF [42], [43], where the driver is Z-300 [36], a conceptual design for a future LTD-based pulsed-power facility (see Section V and Fig. 23). The inductive dip occurs during the implosion, as the load inductance (impedance) rapidly increases. The current recovery and amplification occur after stagnation. The current amplification is driven by the powerful fusion reactions, which cause the liner to explode radially outward, rapidly compressing the magnetic flux of the driving B_θ field. The compressing B_θ flux amplifies B_θ and thus amplifies the current I via (3). Also note that, although it is not shown in this plot, the L-dot voltage ($\dot{L}I$) reverses (becomes negative) when the liner begins to explode radially outwards.

liner implosion driven by an electrical current that is distributed radially throughout the liner wall and includes ohmic dissipation [i.e., where $L(t)$, $R(t)$, and material compression are included], see [42].

Referring to the oscillations presented in Fig. 6, we see that there are times when $V(t)$ and $I(t)$ are both positive (or both negative). During these times, the electrical power $P(t) = V(t) \times I(t)$ is positive, which means that electromagnetic energy is being driven into the vacuum cavity shown in Fig. 1(a). This is equivalent to saying that the Poynting vector $\mathbf{S} = \mathbf{E} \times \mathbf{B}/\mu_0$ (which is the electromagnetic energy flux) is directed radially into the cavity when both $V(t)$ and $I(t)$ are positive (or both negative). For static inductive loads ($L = \text{constant}$, $\dot{L} = 0$), and for the typical experimental region shown in Fig. 6, power and energy are driven into the cavity only when $dI/dt > 0$ (which is driven by $V(t) > 0$). When $V(t) > 0$, the magnetic flux is driven into the cavity, and $B(t)$, $I(t)$, and $\Phi(t)$ all increase together according to (3), (10), and (37) (this is the important rising edge of the current pulse). Just after peak current, $V(t) < 0$, $dI/dt < 0$, and the Poynting vector reverses, driving magnetic flux out of the cavity [$B(t)$, $I(t)$, and $\Phi(t)$ all decrease together according to (3), (10), and (37)]. For the simple LC discharge characteristics presented in Fig. 6, the maximum power delivery into the cavity occurs at $t = \tau_{\text{peak}}/2$, when both $V(t)$ and $I(t)$ are large. Note that there is no power delivery at peak current ($t = \tau_{\text{peak}}$) because $V(\tau_{\text{peak}}) = 0$.

Assuming that $L = \text{constant}$ ($\dot{L} = 0$) in Fig. 1(a), and assuming that Fig. 1(a) is drawn such that $V(t) > 0$, $dI/dt > 0$, and $I(t) > 0$, we would have a driving electric

field $\mathbf{E}$ that points downward in the vacuum region, from the top $(+)$ electrode to the bottom $(-)$ electrode. From fundamental electricity and magnetism, we know that the $\mathbf{E}$ field must be zero inside the bulk of the perfect conductors, while the primarily vacuum $\mathbf{E}$ field terminates abruptly at the metal surfaces (within an infinitesimal skin depth from the surface). The direction of the $\mathbf{E}$ field is perpendicular to the upper and lower metal surfaces because a driving voltage is applied across the upper and lower electrodes, and because tangential electric field components are not supported in perfect conductors. Additionally, because tangential electric field components are not supported in perfect conductors, we know that $|\mathbf{E}|$ must decrease to zero at the outer surface of the central metal stalk. That is, the vector $\mathbf{E}$ is pointed downward everywhere in the vacuum region of the cavity, but its magnitude $|\mathbf{E}|$ is maximal at the largest cavity radius and decreases to zero at the outer surface of the central metal stalk. Note that the zeroing of $|\mathbf{E}|$ at the central metal stalk is consistent with the fact that the stalk is a short-circuit load.

To further understand how the driving electric field relates to the magnetic field being pumped into (or out of) the cavity, consider (37). This equation comes from the integral form of Faraday's law

$$-\oint_C \mathbf{E} \cdot d\mathbf{l} = \dot{\Phi} \tag{51}$$

where C represents the curve that the path integral takes, and $d\mathbf{l}$ is an infinitesimal path element vector along C. The left-hand side (LHS) of this equation is just the inductive loop voltage V_L around the circuit C (only one time around). Note that we can construct C however we like. Thus, for convenience, we choose to make C into a rectangle that fully encloses the vacuum region on the RHS of Fig. 1(a), out to an arbitrary cavity radius r_{out}. We also set the direction of the path integral around C to be in the counterclockwise direction [to be consistent with the direction of increasing current flow $I(t) > 0$ and $\dot{I} > 0$ due to the applied voltage $V(t) > 0$ shown in Fig. 1(a)]. Next, we break up C into four line segments C_1, C_2, C_3, and C_4, which represent the four sides of the rectangular circuit C. We place the horizontal line segments C_1 and C_3 just within the metal regions of the upper and lower electrodes, respectively. Similarly, we place the vertical line segment C_2 just within the metal region of the central metal stalk. That is, these three line segments, C_1, C_2, and C_3, are all placed immediately adjacent to the vacuum region that C encloses, but they are all placed *inside* the metal. The vertical line segment C_4 then closes the circuit C by crossing the vacuum region at the specified (but arbitrary) cavity radius r_{out}. Now, since tangential electric field components are not supported in perfect conductors, and since $d\mathbf{l}$ is everywhere tangential to the metal–vacuum interface for line segments C_1, C_2, and C_3, we must have

$$\int_{C_1} \mathbf{E} \cdot d\mathbf{l} = \int_{C_2} \mathbf{E} \cdot d\mathbf{l} = \int_{C_3} \mathbf{E} \cdot d\mathbf{l} = 0. \tag{52}$$

Thus, we are left with

$$-\oint_C \mathbf{E} \cdot d\mathbf{l} = -\int_{C_4} \mathbf{E} \cdot d\mathbf{l} = |\mathbf{E}| \cdot h = V = \dot{\Phi}. \tag{53}$$

Note that since we chose the direction of our path integral to be counterclockwise around the vacuum region on the RHS of Fig. 1(a), the direction of $d\mathbf{l}$ along the line segment C_4 is upward, from the lower electrode to the upper electrode, while the direction of our applied electric field $\mathbf{E}$ is downward, from the positive upper electrode to the negative lower electrode. Since these two directions are opposite to one another, a minus sign is generated, which cancels the minus sign in Faraday's law [on the LHS of (51) and (53)]. Thus, we have $- \oint_C \mathbf{E} \cdot d\mathbf{l} = - \int_{C_4} \mathbf{E} \cdot d\mathbf{l} = |\mathbf{E}| \cdot h = V = \dot{\Phi} > 0$.

To determine the direction of the changing magnetic field associated with $\dot{\Phi}$ in (53), we apply the right-hand rule to Faraday's law. By curling our right-hand fingers counterclockwise to represent C enclosing the vacuum region on the right side of Fig. 1(a), we find that our thumb points out of the page. Thus, $\dot{\Phi}$ (and therefore $\dot{\mathbf{B}} = \dot{B}_\theta(r)\,\hat{\boldsymbol{\theta}}$) should be increasing in the direction coming out of the page for the right side of Fig. 1(a). This is consistent with the directions indicated in Fig. 1(a), where, if we start with $I = 0$ and $V = 0$, and we suddenly apply a voltage $V(t) > 0$ as indicated in Fig. 1(a) (with $+$ on top), then we will drive an increasing current into the cavity as indicated by the arrows for $I(t)$ in Fig. 1(a). This can be understood further by applying the right-hand rule to Ampère's law. In this case, our right hand thumb points in the direction of the increasing current, which is downward in Fig. 1(a). Doing this, our curling right hand fingers then indicate that, indeed, the direction of the increasing B_θ is out of the page for the right side of Fig. 1(a). This result is thus consistent with our application of the right-hand rule to Faraday's law.

To find the radial distribution of the vertical (axial) electric field in the static vacuum cavity of Fig. 1(a) (i.e., to find $|\mathbf{E}(r)| = V(r)/h$), we need to evaluate Faraday's law as a continuous function of r, rather than just for the single arbitrary radius r_{out}. That is, we need to allow the line segment C_4 to be positioned at any radial location r, rather than just r_{out}. To do this, we first write $V(r) = \dot{\Phi}(r) = L(r)\dot{I}$, where we have used (37) with $\dot{L} = 0$ for our present case of a static vacuum cavity. Next, we find an expression for $L(r)$ by using (11) and/or (14) and letting $r_{\text{out}} \to r$ and $r_{\text{in}} \to r_{\text{stalk}}$, where r_{stalk} is the radius of the central metal stalk's outer surface. Combing these results gives

$$|\mathbf{E}(r)| = \frac{V(r)}{h} = \frac{L(r)\dot{I}}{h} = \frac{\mu_0}{2\pi} \ln\left(\frac{r}{r_{\text{stalk}}}\right) \dot{I}. \quad (54)$$

Thus, $|\mathbf{E}(r)|$ and $V(r)$ vary logarithmically with r. Starting from their maximal values at the driving input end of the cavity (at the outermost radius of the cavity), they decrease logarithmically to zero at the outer surface of the central metal stalk.

From (3), we know that $|\mathbf{B}(r)| = \mu_0 I/(2\pi r)$ and that $\mathbf{B}$ is pointing into (out of) the page on the left (right) side of Fig. 1(a). Therefore, from the right-hand rule, we find that the electromagnetic energy flux is pointed radially into the cavity, with a radial distribution given by

$$\mathbf{S}(r) = \mathbf{E}(r) \times \mathbf{B}(r)/\mu_0 = \frac{\mu_0 I \dot{I}}{4\pi^2 r} \ln\left(\frac{r}{r_{\text{stalk}}}\right) (-\hat{\mathbf{r}}). \quad (55)$$
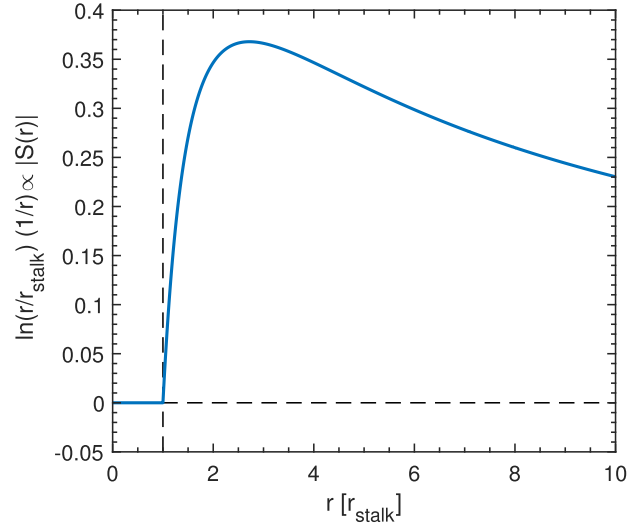

Fig. 8. Plot of $\ln(r/r_{\text{stalk}}) \cdot (1/r)$, which is proportional to $|\mathbf{S}(r)|$ for the stationary (nonimploding) cavity illustrated in Fig. 1(a). The r-axis is in units of r_{stalk}. The Poynting flux is maximal at $r = e \cdot r_{\text{stalk}} = 2.71828 \cdot r_{\text{stalk}}$ and goes to zero at $r = r_{\text{stalk}}$.

Thus, $|\mathbf{S}(r)| \propto \ln(r/r_{\text{stalk}}) \cdot (1/r)$. This radial distribution is plotted in Fig. 8, where r is in units of r_{stalk}. The radial distribution has a maximum at $r = e \cdot r_{\text{stalk}}$, where $e = 2.71828$ is Euler's (exponential) number. From large radial values inward, the Poynting flux increases to its maximum value because of cylindrical convergence (energy compression in space); however, a maximum value is reached at $r = e \cdot r_{\text{stalk}}$, rather than at $r = r_{\text{stalk}}$, because the energy flow must go to zero at $r = r_{\text{stalk}}$. The energy flow must go to zero at $r = r_{\text{stalk}}$ because the outer surface of the central metal stalk perfectly reflects all of the incoming electromagnetic energy. Since the reflected (radially outward) energy flow exactly cancels the radially inward energy flow, the net Poynting vector is zero (along with the electric field). This is again consistent with the fact that the stalk is a short-circuit load.

The picture presented above for power and energy flow must be modified slightly for the imploding case illustrated in Fig. 1(b) and (c). Because of the implosion, $L = L(t)$ and $\dot{L} \neq 0$. This generates a motional electromotive force (EMF). This motional EMF is just the L-dot voltage ($\dot{L}I$) discussed previously, which is accompanied by an electric field. As in the nonimploding case, the motion-induced electric field is vertical (axial), it exists only in the vacuum region, and it points downward, from the top electrode to the bottom electrode. Unlike the nonimploding case, however, the motion-induced electric field is maximal along a vertical line that is immediately adjacent to the imploding liner's outer surface. It is important to note that this vertical line is stationary in the lab frame, while the liner's imploding surface is moving relative to the lab frame (and thus relative to the vertical line as well). To be clear, this is still an inductive loop voltage, but the loop has an infinitesimal area $dA = h \cdot dr$, where h is the height of the moving/imploding surface [which, for simplicity, was chosen to be equal to the height of our vacuum cavity in Fig. 1(b) and (c)] and dr is the infinitesimal radial

motion that occurs during an infinitesimal time step dt. This newly created infinitesimal loop corresponds to an infinitesimal change in inductance dL. It is the rate at which this new infinitesimal loop is being created that gives rise to $dL/dt \equiv \dot{L}$ and the L-dot voltage $\dot{L}I$. Because it is an infinitesimal loop in the vacuum region, the electric field exists only in the vacuum region. Thus, despite being tangential to the moving metal surface and infinitesimally close to the moving metal surface, this electric field does not violate the electric field boundary condition, which states that tangential electric field components are not supported *inside* perfect conductors.

The motion-induced electric field infinitesimally close to the imploding liner's outer surface means that there is a current-impeding voltage drop infinitesimally close to the imploding liner's outer surface. In light of this, we rewrite (37) as

$$V_L - \dot{L}I = L\dot{I}. \tag{56}$$

Here, we now understand that V_L is the driving voltage at the source capacitors, $\dot{L}I$ is the voltage drop infinitesimally close to the liner's outer surface due to the motion of the liner's outer surface, and the difference between the two is $L\dot{I}$. Thus, we see that $\dot{L}I$ reduces the $\dot{I}$ that would occur if the liner were not imploding. For example, when the L-dot voltage infinitesimally close to the liner surface is equal to the driving voltage at the capacitors, we have $\dot{I} = 0$, and the current is constant despite the fact that we are still driving the system at the source capacitors. If the L-dot voltage exceeds the driving voltage, then $\dot{I} < 0$, and the current is decreasing despite the fact that we are still driving the system at the source capacitors—this is the "inductive dip" discussed previously.

Because of the axial electric field infinitesimally close to the imploding liner's outer surface, the radial profiles $|\mathbf{E}(r)|$, $V(r)$, and $|\mathbf{S}(r)|$ will be modified from the stationary case presented above. $|\mathbf{E}(r)|$ and $V(r)$ will still vary logarithmically with r, but they will no longer go to zero infinitesimally close to the liner's outer surface; instead, they will go to $\dot{L}I/h$ and $\dot{L}I$, respectively. Note that if $\dot{L}I$ exceeds the driving voltage, then $|\mathbf{E}(r)|$ and $V(r)$ will *decrease* logarithmically with r from the vacuum region infinitesimally close to the liner's outer surface out to the driven end of the cavity (at the outermost radius of the cavity). Also, if $\dot{L}I$ equals the driving voltage V_L, then $|\mathbf{E}|$ and V will be *spatially constant* throughout the cavity. For this spatially constant $|\mathbf{E}|$ and V case, $|\mathbf{S}(r)| = |\mathbf{E} \times \mathbf{B}(r)/\mu_0|$ will vary as $1/r$ because $|\mathbf{B}(r)| = \mu_0 I/(2\pi r)$. Having $|\mathbf{S}(r)| \propto 1/r$ would significantly modify the plot shown in Fig. 8. For example, $|\mathbf{S}(r)|$ would no longer go to zero infinitesimally close to the liner's outer surface. Instead, $|\mathbf{S}(r)|$ would be maximal infinitesimally close to the liner's outer surface.

Another interesting case occurs when a liner is imploding rapidly ($\dot{L} \gg 0$) after the time when a given machine would obtain its peak current if the machine were being discharged into a static inductive load (i.e., after the "natural" rise time of the machine). At these late times, the current is still positive [flowing downward in Fig. 1(b) and (c)], but the driving voltage and the electric field at the driven end of the cavity have both reversed [$V_L < 0$ and $\mathbf{E}$ is now pointed *upwards* at the driven end of the cavity in Fig. 1(b) and (c)]. In this

case, because $I(t) > 0$ and $\dot{L} > 0$, the L-dot voltage $\dot{L}I > 0$, and its associated motional electric field is pointed *downwards* in Fig. 1(b) and (c). As mentioned above, the magnitude of $\dot{L}I$ and its associated motional electric field are both maximal immediately adjacent to the imploding liner's outer surface. Therefore, within the vacuum cavity, the total electric field (the superposition of the motional electric field and the driving electric field) goes from positive (downwards) near the liner's imploding outer surface to negative (upwards) at the driven end of the cavity. Thus, the total electric field passes through zero (a null point) at some radius between the imploding liner's outer surface and the driven end of the cavity. The magnitude of the total electric field increases (with opposite polarities on either side of this radial null point) as the distance away from this null point (either radially inward or radially outward) increases. This example provides a nice picture of the curling $\mathbf{E}$ field that exists within the vacuum cavity. By Faraday's law, this curling $\mathbf{E}$ field is consistent with $-\partial\mathbf{B}/\partial t$ and the rapidly decreasing current that occurs when a liner implodes at these late times—i.e., at these late times, both the driving voltage and the inductive dip work together (in the same direction) to decrease the current faster than would occur if the load were a static inductive load.

For any of these imploding cases, the Poynting vector, $\mathbf{S}$, infinitesimally close to the imploding liner's outer surface is no longer zero because the electric field infinitesimally close to the liner's outer surface is no longer zero. This means that there is a net electromagnetic energy flow into the vacuum region that is infinitesimally close to the liner's outer surface. This energy flow is partially absorbed by the liner (it is no longer completely reflected, as in the nonimploding case). The energy that flows into this infinitesimal region is converted into: 1) the liner's imploding kinetic energy; 2) the compressional work that is done on both the liner walls and any substances being compressed by the liner; and 3) the energy of the new magnetic field that must be supplied to fill the newly formed infinitesimal loop immediately adjacent to the imploding liner's outer surface. This total power flow into this infinitesimal region is just the L-dot power $P_{\dot{L}} = \dot{L}I^2$ discussed previously (40). This total power flow is equipartitioned according to (50), which states that $P_{\text{mech}} = P_{B_{\text{new}}} = (1/2)P_{\dot{L}} = (1/2)\dot{L}I^2$.

The Poynting vector analysis above is useful for further illustrating how $\dot{L}$ is analogous to a resistance R. The Poynting vector can be evaluated over the bounding surface of a cylindrical resistor to find that the total electromagnetic power converted into heat by the resistor is $P_\Omega = I^2 R$ (38). Note that along the outer surfaces of both cylindrical cases ($\dot{L}$ for an imploding cylindrical liner and R for a stationary cylindrical resistor), there is an axial electric field $\mathbf{E}$ (in the direction of the current) and an azimuthal magnetic field $\mathbf{B}$. The crossed $\mathbf{E}$ and $\mathbf{B}$ fields give a Poynting vector $\mathbf{S}$ that is directed radially into the cylinders. Working through this analogy/exercise is strongly encouraged for students and researchers interested in pulsed-power and magnetically driven implosions.

To optimize power coupling to resistive loads, the driver impedance should be well matched to the load resistance [62].

From the LHS of (56), we see that the units of $\dot{L}$ are equivalent to Ω (i.e., H/s $= \Omega$). Thus, for efficient coupling of the driver energy to the kinetic and/or compressional energy of an imploding liner, the driver impedance should be well matched to the intended $\dot{L}$ impedance. Since a driver has a finite impedance, and since the liner implosion starts with zero initial velocity, the liner is initially not well matched to the driver— initially, the stationary liner reflects all of the power from the driver, because a stationary liner is a short-circuit load. As the liner begins to accelerate radially inward, the $\dot{L}$ value increases, and the liner's $\dot{L}$ impedance becomes better matched to the driver impedance. It is possible that the implosion velocity becomes so large that $\dot{L}$ exceeds the driver impedance. If $\dot{L}$ becomes much larger than the driver impedance, then the liner will again reflect much of the incoming electromagnetic power, but in this case, the imploding liner will look like an open circuit, rather than a short circuit.

Throughout the $|\mathbf{E}(r)|$ and $V(r)$ discussion above, the electric field was purely *axial* (vertical). This was because we were analyzing purely *radial* power feeds (i.e., the purely radial power feeds illustrated in Fig. 1). Here, however, we note that if the power feed is not purely radial, then nonaxial (nonvertical) electric fields will arise. For example, consider a purely coaxial system consisting of two concentric cylindrical conductors, an inner conductor and an outer conductor, separated by vacuum. Let's further assume that the system geometry is static and that the axes of the two conductors are aligned with the vertical $\hat{\mathbf{z}}$ axis of a cylindrical coordinate system. In between the two conductors is a purely radial A–K gap. Initially (at $t = 0$), the current and voltage are both zero. At the top end of the line, we apply a conducting "shorting cap" across the A–K gap to terminate the line [see, for example, the uppermost horizontal electrode in Fig. 3, which spans the radial A–K gap of the final (coaxial) section of the power feed]. At the bottom end of the line, for $t > 0$, we apply a driving voltage $V(t)$ across the radial A–K gap, which results in a purely *radial* electric field throughout the purely *coaxial* cavity. If the center conductor in a coaxial system is negative (cathode), then we call this *negative polarity*, and the electric field will point in the direction of $-\hat{\mathbf{r}}$ (note that, with the exception of the dense plasma focus, most pulsed-power-driven HEDP experiments are conducted in negative polarity).

Because this purely coaxial system is cylindrically symmetric, we again drive a current $I(t)$ that results in a purely azimuthal magnetic field $|\mathbf{B}(r)| = |B_\theta(r)| = \mu_0 I/(2\pi r)$. The electric field, however, is no longer constant across the A–K gap (i.e., $\mathbf{E}$ is no longer constant in the direction of $\mathbf{E}$). Instead, we have $|\mathbf{E}(r)| = |E_r(r)| \propto 1/r$. Nonetheless, for $V(t) > 0$ during the typical experimental period shown in Fig. 6, the crossed $\mathbf{E}$ and $\mathbf{B}$ fields result in a Poynting vector $\mathbf{S} = \mathbf{E} \times \mathbf{B}/\mu_0$ that is directed upwards and into the coaxial vacuum cavity. As in our previous analyses, the magnitude of the vacuum electric field ($|\mathbf{E}| = |E_r|$ in this case) must go to zero at the end of the line (at the shorting cap) because tangential electric fields (radial electric fields in this case) are not supported at the surface of perfect static conductors.

To find the radial distribution of the radial electric field $|\mathbf{E}(r)| = |E_r(r)| \propto 1/r$, we use the relationships that describe a cylindrical capacitor of length ℓ with a total charge $-Q$ stored on the inner conductor and $+Q$ stored on the outer conductor. Starting with the integral form of Gauss's law for a cylindrically symmetric coaxial system, we get

$$\oint_A \mathbf{E} \cdot d\mathbf{A} = -E_r \cdot 2\pi r \cdot \ell = \frac{-Q}{\epsilon_0}$$
$$\Rightarrow E_r(r) = \frac{Q/\epsilon_0}{2\pi r \cdot \ell}. \tag{57}$$

Here, $d\mathbf{A}$ is an infinitesimal surface area element on the outer surface of the inner conductor. Note that $\mathbf{E} \cdot d\mathbf{A}$ produces a minus sign because $d\mathbf{A}$ is directed outward normal to the outer surface of the inner conductor while the electric field is pointed radially inward for an inner conductor with $-Q$.[1] Next, we use

$$V = -\int_{r_{\text{in}}}^{r_{\text{out}}} \mathbf{E} \cdot d\mathbf{r} = \frac{Q/\epsilon_0}{2\pi \cdot \ell} \int_{r_{\text{in}}}^{r_{\text{out}}} \frac{1}{r} dr$$
$$= \frac{Q/\epsilon_0}{2\pi \cdot \ell} \ln\left(\frac{r_{\text{out}}}{r_{\text{in}}}\right). \tag{58}$$

Note that since $Q = CV$, the capacitance of this cylindrical coaxial system is

$$C = \frac{\epsilon_0 \cdot 2\pi \cdot \ell}{\ln\left(\frac{r_{\text{out}}}{r_{\text{in}}}\right)}. \tag{59}$$

Combining (57) and (58) to eliminate Q gives the radial dependence of the radial electric field in a static coaxial line

$$|\mathbf{E}(r)| = |E_r(r)| = \frac{V}{r \cdot \ln\left(\frac{r_{\text{out}}}{r_{\text{in}}}\right)}. \tag{60}$$

Note, however, that in this equation, the inductive voltage V varies axially along the length of the line, thus $|E_r(r)| \rightarrow |E_r(r, z)|$. The axial variation can be found by using $V(z) = L(z)\dot{I}$ [(37) with $\dot{L} = 0$], where $L(z)$ is given by (11) and/or (14) with $h \rightarrow z_{\text{top}} - z$. Here we have replaced the arbitrary line-length parameters h and/or ℓ with $z_{\text{top}} - z$, where z_{top} is the position of the shorting cap at the top of the line, and z is the continuous axial position variable *within* the cavity. Substituting $V(z) = L(z)\dot{I}$ into (60) gives

$$|\mathbf{E}(r, z)| = |E_r(r, z)| = \frac{\mu_0 \dot{I}}{2\pi} \frac{z_{\text{top}} - z}{r}. \tag{61}$$

---

[1]Note the similarity between (57) for a radial electric field in cylindrical geometry ($E_r(r) = (1/\epsilon_0)\hat{Q}/(2\pi r)$) and (3) for an azimuthal magnetic field in cylindrical geometry ($B_\theta(r) = \mu_0 I/(2\pi r)$). Instead of $\mu_0 I$, with $I = dQ/dt$ being the total current enclosed by a circle of radius r, we have $(1/\epsilon_0)\hat{Q}$, where ϵ_0 is the permittivity of free space and $\hat{Q} = Q/\ell$ is the total charge per unit length, or *linear charge density*, enclosed by a circle of radius r. We can also make use of a *surface charge density* $\rho_s = Q/(2\pi r \cdot \ell)$ to write (57) as $\mathbf{E} = E_r \hat{\mathbf{r}} = (1/\epsilon_0)\rho_s$. This is the electric boundary condition which states that $\mathbf{E}$ is essentially equivalent to the surface charge density ρ_s at the interface between a perfect conductor and vacuum (where the equivalence is given through the proportionality constant $1/\epsilon_0$). This electric boundary condition is analogous to the magnetic boundary condition discussed previously [see (4) and (5) as well as Fig. 2], which states that $\mathbf{B}$ is essentially equivalent to the *surface current density* $\mathbf{J}_s$ at the interface between a perfect conductor and vacuum (where this equivalence is given through the proportionality constant constant μ_0).

This result shows that, within the coaxial vacuum cavity, the radial electric field $|E_r(r,z)|$ varies *linearly* with $z_{top} - z$ and decreases to zero at the shorting cap (at $z = z_{top}$). The maximum value of $|E_r(r,z)|$ is at the bottom (input end) of the line, where the voltage is applied, and at the smallest radius possible (i.e., at the outer surface of the inner conductor, where $r = r_{in}$).

Using (3) and (61), we find that the Poynting flux is once again a function of r, though this time it is directed upwards and it is also a function of z

$$\mathbf{S}(r,z) = \mathbf{E}(r,z) \times \mathbf{B}(r)/\mu_0 = \frac{\mu_0 I \dot{I}}{4\pi^2} \frac{z_{top} - z}{r^2} \hat{\mathbf{z}}. \quad (62)$$

This equation is for a purely coaxial feed. It should be contrasted with (55), which is for a purely radial feed.

If we place a radially imploding (or exploding) liner at the end of our purely coaxial line, then we will generate an *axial* electric field adjacent to the liner's imploding (or exploding) surface. This is again because of the motion-generated L-dot voltage ($\dot{L} I$). Additionally, as the liner implodes inward (or explodes outward), the feed will no longer be purely coaxial (there will be both coaxial and radial line segments). This complicates the picture described above, because both axial and radial electric field components will be present. In general, and in practice, power feeds are rarely purely axial or purely radial. They will be some combination of both, often involving curves and stepwise transitions like those illustrated in Figs. 3, 4, 10, 16, 18(a), and 19(a). In evaluating complex feeds, the electric field lines in the feed can often be sketched/estimated reasonably well by ensuring that the electric field lines terminate on conducting surfaces in directions that are normal to the conducting surfaces. In other words, we must ensure that any tangential electric field components decrease to zero infinitesimally close to the conducting surfaces (unless the conducting surface is moving). Though the electric field lines can be sketched/estimated, it is often best to seek computational tools to avoid being fooled by $1/r$ effects in these cylindrical systems.

In pulsed-power-driven HEDP experiments, charged particles and low-density plasmas can exist within the A–K gaps of the vacuum cavities (power feeds). For example, the intense ohmic heating of the electrodes (due to the intense current densities) can result in plasma generation near the electrodes. Additionally, neutral particles in the A–K gaps, due to imperfect vacuum systems and residual background gases, can become photoionized during the experiment. Furthermore, the intense electric fields in the A–K gaps can pull charged particles out of the electrodes/electrode plasmas and into the A–K gaps by mechanisms such as field emission and explosive emission. The electric and magnetic fields can then accelerate the charged particles in the A–K gap according to the Lorentz force equation

$$\mathbf{F} = q(\mathbf{E} + \mathbf{v} \times \mathbf{B}). \quad (63)$$

If $\mathbf{E}(r)$ accelerates the charged particles across the A–K gap at some radius that is larger than the intended target radius, then a shunt current loss has occurred. This is also a power loss, because the magnetic energy associated with the shunted current does not make it to the intended target at the center of the machine. Shunt current losses are prevented (or at least strongly mitigated) in pulsed-power-driven HEDP experiments by the process of *self-magnetic insulation*.

Self-magnetic insulation occurs when the current densities on the electrode surfaces are high enough for the corresponding magnetic field in the A–K gap to be strong enough to prevent charged particles from crossing the A–K gap. For example, consider a positively charged particle initially at rest. As the $\mathbf{E}$ field begins to accelerate the particle across the A–K gap via the $q\mathbf{E}$ term in the Lorentz force equation (63), the particle velocity $\mathbf{v}$ begins to increase in the direction of $\mathbf{E}$, which is towards the cathode. This increases the redirecting $q\mathbf{v} \times \mathbf{B}$ term in the Lorentz force equation because $\mathbf{E}$ (and thus the initial $\mathbf{v}$) is perpendicular to $\mathbf{B}$. Now, if the $\mathbf{B}$ field in the A–K gap is strong enough (i.e., if the current density on the electrode surface is high enough), then the redirecting $q\mathbf{v} \times \mathbf{B}$ term can become strong enough to turn the particle around before the particle reaches the cathode. Once the particle has reversed directions, the $\mathbf{E}$ field begins decelerating the particle until the particle returns to rest. After returning to rest, the particle has been displaced from its initial position, in the direction of $\mathbf{E} \times \mathbf{B}$. The process then repeats. The result is a repeating cycloidal orbit with sharp cusps. If instead of initially being at rest, the charged particle has some initial velocity perpendicular to $\mathbf{B}$, then the resulting orbit is a drifting circular orbit, and the sharp cusps are replaced with loops. These curved gyro orbits occur because the redirecting $q\mathbf{v} \times \mathbf{B}$ force is always perpendicular to both $\mathbf{v}$ and $\mathbf{B}$. The resulting "*E cross B drift*" ($\mathbf{v}_{drift} = \mathbf{E} \times \mathbf{B}/B^2$ [70]) is in the direction of the Poynting vector $\mathbf{S} = \mathbf{E} \times \mathbf{B}/\mu_0$.

Because $\mathbf{v}_{drift}$ is in the direction of $\mathbf{E} \times \mathbf{B}$, the charged particle drifts are driven into a static cavity when the voltage and current are both positive (or both negative). For example, charged particles are driven into a static cavity during the rising edge of a fast current pulse. This would be radially inward for a purely radial feed, axially upwards for a purely coaxial feed (where the coaxial feed is driven at the bottom end of the feed), or a combination of both radially inward and axially upwards for a combined radial and axial feed. After peak current, when the voltage reverses (along with the $\mathbf{E}$ field) and the current is still positive (along with the $\mathbf{B}$ field), the charged particles are driven out of the cavity. For the case of a purely radial power feed that is static [e.g., Fig. 1(a)], the drift velocity's radial distribution is given by

$$|\mathbf{v}_{drift}(r)| = |v_r(r)| = \left| \frac{\mathbf{E}(r) \times \mathbf{B}(r)}{B^2(r)} \right| = \left| \frac{E(r)}{B(r)} \right|$$
$$= \frac{r\dot{I}}{I} \ln\left(\frac{r}{r_{stalk}}\right). \quad (64)$$

Since this is for a purely radial and static power feed, $\mathbf{E}(r)$ is given by (54), while $\mathbf{B}(r)$ is given by (3) for any power feed that is azimuthally symmetric. Thus, $|\mathbf{v}_{drift}(r)| \propto \ln(r/r_{stalk}) \cdot r$. This radial distribution increases monotonically with r, which should be contrasted with the peaked distribution given by $|\mathbf{S}(r)| \propto \ln(r/r_{stalk}) \cdot (1/r)$ [see (55) and Fig. 8].

For power feeds/loads that are in motion and for power feeds with coaxial components, (64) needs to be modified. For example, consider the case described above for a purely radial feed, where a liner is imploding after the "natural" rise time of the machine, while $I(t)$ is still positive. As discussed above, the total $\mathbf{E}(r)$ field has a null point at some radius in the power feed, with increasing values of opposite polarities on either side of this null point. Thus, $\mathbf{v}_{\text{drift}}(r) = \mathbf{E}(r) \times \mathbf{B}(r)/B^2(r)$ will also have a null point at this radius, with $\mathbf{v}_{\text{drift}}(r)$ being directed radially inward for radii less than the radius of the null point and being directed radially outward for radii greater than the radius of the null point. Note that the electromagnetic energy flux also goes through a null point at this radius, since $\mathbf{S}(r) = \mathbf{E}(r) \times \mathbf{B}(r)/\mu_0$. As another example, consider the case of a purely coaxial and static feed. In this case, we would have to use (61) for $\mathbf{E}$, and thus $|\mathbf{v}_{\text{drift}}| \to |\mathbf{v}_{\text{drift}}(r,z)| = |v_z(r,z)|$.

The charged particles drifting at $\mathbf{v}_{\text{drift}} = \mathbf{E} \times \mathbf{B}/B^2$ do not easily cross the A–K gap. Instead, they are part of a self-magnetically insulated flow, which is in the direction of the electromagnetic power flow $\mathbf{S} = \mathbf{E} \times \mathbf{B}/\mu_0$. An example of a self-magnetically insulated flow that is often studied is the flow of a negative cloud of electrons (i.e., a nonneutral plasma) [71]–[75]. This type of flow is sometimes referred to as *Brillouin* flow, after [71]. Here, the electron cloud connects to the negative electrode (cathode) and partially fills the A–K gap. With higher currents and lower applied voltages, the electron cloud is pinned closer to the cathode. The thickness of the cloud (or electron flow layer) is found by balancing the sum of the electric and magnetic field pressures (energy densities) at the anode with the magnetic field pressure at the cathode (there is no electric field pressure at the cathode, because $\mathbf{E} \to 0$ at the cathode due to the shielding effect of the electron cloud). Note that the electric field energy density $\epsilon_0 E^2/2$ at the anode is associated with the voltage applied to the A–K gap, while the magnetic energy densities $B^2/(2\mu_0)$ at the anode and cathode are associated with the current flowing in the anode and cathode, respectively. There is a difference between the anode current I_a and cathode current I_k because some of the nominal cathode current is carried by the electron flow layer *within* the A–K gap (i.e., $I_k + I_f = I_a$, where I_f is the current carried in the electron flow layer).

Balancing the field pressures for an electron flow layer can also be used to find a so-called *flow impedance*, which effectively relates the applied voltage V to I_f by instead relating V to the associated currents I_a and I_k (where I_a and I_k are associated with I_f because $I_f = I_a - I_k$). This is typically done while accounting for space-charge effects. The characteristic impedance of a transmission line with charged particles in the A–K gap is lower than that of a pure vacuum transmission line, because the A–K gap is effectively decreased by the flowing space-charge layer.

In well-designed machines, and in first-order approximations, flow impedance effects can often be ignored, but not always. For example, significant effects can occur at large impedance discontinuities in the transmission line structures (more will be said about this in Section IV). A detailed discussion on flow impedance and other important processes that can occur within the A–K gaps of pulsed-power-driven

HEDP experiments (e.g., charge exchange processes involving neutral particles, electrode surface chemistry and contamination [76], [77], the inverse skin effect [78], [79], etc.) are beyond the scope of this tutorial. However, interested students and researchers should be aware of these phenomena, as they are areas of active research. More information on these topics can be found in [71]–[79].

Before closing this discussion, it should be noted that the overall drift of charged particles in the A–K gap can be further modified by ∇B, curved $\mathbf{B}$, and $d\mathbf{E}/dt$ effects. These drifts are the so-called *grad-B*, *curved vacuum field*, and *polarization* drifts, respectively [70]. In some cases, these drifts can enhance shunt current losses across the A–K gap. Shunt current losses reduce the magnetic field at the liner's outer surface, which reduces the magnetic pressure that drives the implosion. Here we also note that, for imploding systems, the motional electric field, which is strongest near the imploding liner's outer surface, can become strong enough to overcome the magnetic insulation near the imploding liner, resulting in shunt current losses close to the imploding liner. This is especially likely during an inductive dip, when the current and the corresponding magnetic insulation are both reduced. Strong motional electric fields can also lead to charged particle beams (i.e., electron and ion beams) in the axial direction near the imploding liner. This is sometimes observed in experiments by strong x-ray emission emanating from the anode structures closest to an imploding liner or Z-pinch target. The x-rays are the result of intense electron beams bombarding the anode structures. Furthermore, in deuterium Z-pinch implosions, ion beams consisting of deuterons and/or tritons can be generated, and beam-target fusion products are generally observed [53]. Both the motional electric field effects and the various charged particle drifts discussed above can be estimated using simple analytic calculations. They can also be evaluated using more sophisticated particle-in-cell simulations.

In Sections IV–VI, we will be discussing various ways of configuring the switches and capacitors of a pulsed-power system—i.e., we will be discussing various pulsed-power *architectures*. These discussions will include both the more traditional Marx-generator/pulse-forming-line approach to pulsed power (e.g., the Z machine) as well as some more recent LTD-based approaches (where an LTD cavity is very similar to the simple *LC* model presented above in this section). Throughout these discussions, and regardless of the machine architecture, it will be helpful to keep in mind that voltages V are combined in series for voltage addition, currents I are combined in parallel for current addition, and both voltages and currents are increased together for power amplification (since $P_{\text{electric}} = V \times I$). It will also be helpful to keep in mind that, regardless of the machine architecture, pulsed power for HEDP applications is almost always about energy compression in both *time* and *space*. Energy compression in *time* is achieved by a sequence of storage and switching techniques. That is, energy is stored over a particular timescale and then discharged over a faster time scale to achieve power amplification. This works because power is the rate of energy delivery, $P = \Delta\mathcal{E}/\Delta t$, so by making Δt very small, we can
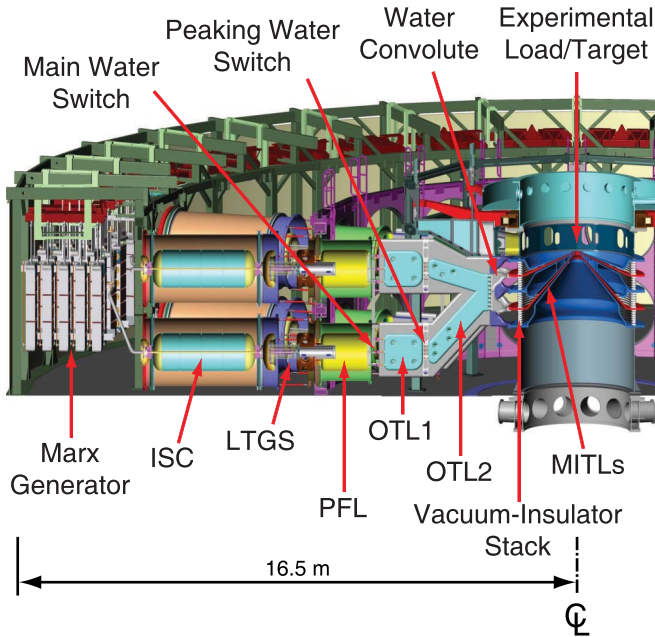
Fig. 9. Cross-sectional drawing of one radial half of the Z-pulsed-power facility (this is *not* an LTD facility). The various components/stages are described in the text. A zoomed-in drawing of the vacuum section (containing the water–vacuum insulator stack, the MITLs, and the experimental load/target region) is provided in Fig. 10. (Source: [80].)

Fig. 10. Cross-sectional drawing of one radial half of the Z vacuum section. (Source: [80].)

make P very large for a finite amount of energy $\Delta\mathcal{E}$. Energy compression in *space* is achieved by storing lots of electrical charge Q at a large radius (e.g., around the outer perimeter of a given machine) and then focusing the discharge current $I = dQ/dt$ to a small radius to achieve large current densities $J(r, t)$ (or equivalently large dQ/dt per unit area). Based on our discussion above for fast 100-ns pulses, the large current densities are associated with large magnetic fields $B(r, t)$, large magnetic pressures $p_{\mathrm{mag}}(r, t) = B^2(r, t)/(2\mu_0)$, and large magnetic energy densities $\mathcal{E}_B(r, t) = p_{\mathrm{mag}}(r, t)$. Furthermore, the process of target implosion and stagnation further compresses energy in both *time* and *space*.

IV. BRIEF REVIEW OF THE Z-PULSED-POWER FACILITY (NOT AN LTD)

Before describing LTDs for HEDP applications, we first describe the Z machine (which is not an LTD) to provide a basis for comparison. The Z machine is presently the world's state-of-the-art pulsed-power facility for studying HEDP. The architecture of the Z machine is illustrated in Figs. 9 and 10 [1], [2]. Prior to pulsing the machine, electrical charge is stored in the capacitors of 36 *Marx generators*, which reside around the perimeter of the machine in a tank filled with oil for electrical insulation (see the left side of Fig 9). The outer diameter of this tank is about 33 m (100 ft).

The Marx generator circuit was patented by Erwin Marx in 1923 [81], [82]. The operating principles behind a simple unipolar Marx generator are illustrated in Fig. 11. Essentially, capacitors are charged in parallel and discharged in series through gas-filled spark-gap switches. During the discharge,
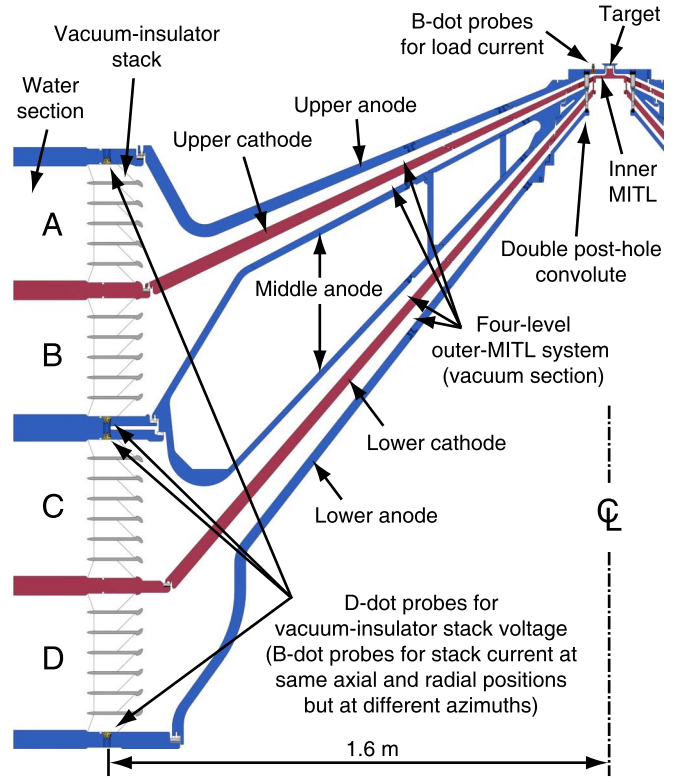
at the output end of the generator, the voltage is amplified to roughly nU_0, where U_0 is the charging voltage and n is the number of capacitors (stages). Also during discharge, the system's equivalent inductance is nL and the system's equivalent capacitance is C/n, where L and C are the inductance and capacitance values for the individual spark-gap switches and capacitors, respectively. Note that this fast reconfiguration from parallel to series (referred to as the Marx *erecting*) effectively increases the system's characteristic impedance: $Z_0 = \sqrt{L/C} \rightarrow n\sqrt{L/C}$. A single Marx generator can therefore be thought of as a high-impedance system, which is useful for driving large voltages into high-impedance loads; however, as we will see, the impedance of a Marx-generator-driven system can be lowered by using several Marx generators in parallel.

The unipolar circuit of Fig. 11 is shown here for its simplicity in illustrating the basic operating principles of a Marx generator. However, the Marx generators on the Z machine are actually of the bipolar type illustrated in Fig 12. In contrast to the unipolar circuit of Fig. 11, the bipolar circuit of Fig. 12 is a bit more complicated. For example, two separate charging lines must be maintained, one at $+U_0$ and one at $-U_0$. Nevertheless, the operating principles are essentially the same (i.e., the capacitors of a given polarity are charged in parallel and then the entire circuit is discharged in series). The benefits of a bipolar circuit are that, relative to the unipolar circuit, the bipolar circuit requires half the number of stages/switches, which reduces the Marx generator's overall size, cost, and inductance.
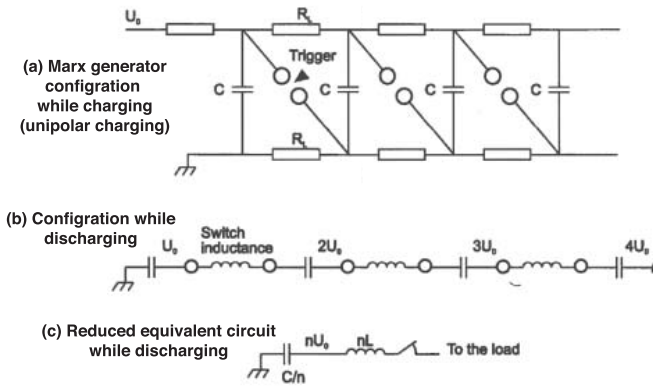
Fig. 11.   The operating principles of a simple unipolar Marx generator. (a) Prior to the discharge triggering event, the capacitors are charged in parallel at a charging voltage U_0, through charging resistors R_L, and the gas-filled spark-gap switches are in an open state. (b) Upon the triggering event, the switches close, and the capacitor configuration changes from parallel to series. (c) A reduced equivalent circuit after the triggering event. (Source: [83].)
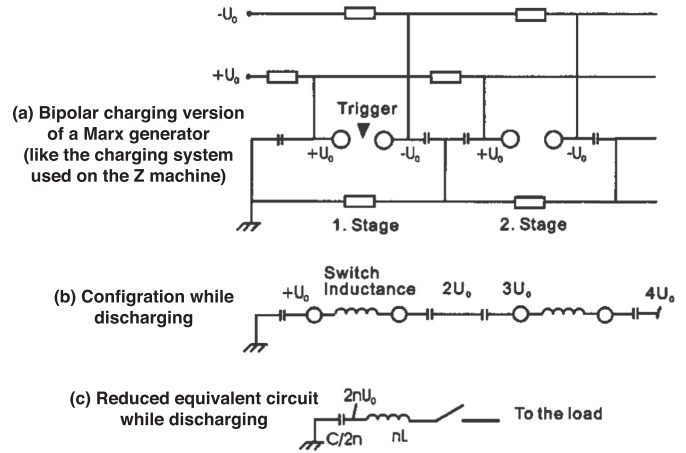

Fig. 12.   The operating principles of a bipolar Marx generator. The Marx generators on the Z machine are bipolar. Relative to the unipolar Marx generator (Fig. 11), the bipolar Marx generator requires half the number of stages/switches, which reduces the Marx generator's overall size, cost, and inductance. (a) Prior to the discharge triggering event, the capacitors are charged in parallel at a charging voltage of either $+U_0$ or $-U_0$, and the gas-filled spark-gap switches are in an open state. (b) Upon the triggering event, the switches close, and the capacitor configuration changes from parallel to series. (c) A reduced equivalent circuit after the triggering event. Note that n shown here for the bipolar circuit would be half the value of n shown for the unipolar circuit of Fig. 11 when generating the same total output voltage. (Source: [83].)

Each Marx generator on the Z machine contains sixty 2.6-μF capacitors. These capacitors can be charged to $U_0 = \pm 100$ kV. Thus, the generator output voltage can be as high as $V_{\text{out}} = 60 \cdot 100$ kV $= 6$ MV. Additionally, with 36 Marx generators on the Z machine, the resulting total electrical energy storage prior to an experiment can be as high as $\mathcal{E}_{\text{store}} = 36 \cdot 60 \cdot (1/2)CU_0^2 = 28$ MJ. (This is about as much energy as running a 100-W lightbulb for a few days, but it is still enough energy to cause significant damage as well as health and safety concerns when it is discharged very rapidly. For example, the energy release from a stick of dynamite is about 1 MJ.)

Because of the large 2.6-μF capacitors (and because of the large inductance of the large capacitors and switches), the Marx generators on Z have a relatively long rise time $\tau_{\text{peak}} \sim [(nL)(C/n)]^{1/2} \sim \sqrt{LC} \sim 1$ μs (cf. Figs. 11 and 12). The use of large capacitors results in a long rise time for two primary reasons: 1) for a given initial charge voltage, larger capacitors have more charge to transfer, since $Q = CV$; and 2) the capacitor discharge rate ($I = dQ/dt$) for a discharge into an inductive channel is limited by the voltage across the capacitor V and the inductance of the discharge channel L, since $dI/dt = V/L$ and thus $I(t) = \int_0^t (dI/dt')dt' = \int_0^t (V/L)dt'$. From the previous expression, note that the discharge rate $I(t)$ could be increased (and thus the rise time τ_{peak} could be decreased) by decreasing the channel inductance L. However, this is often difficult to do in practice, since the discharge channel in this case would be the current-carrying plasma channel that forms when a gas-filled spark-gap switch breaks down to close the switch, and there are practical limits to how small the inductance of this breakdown channel can be made. Thus, for a given initial charge voltage and for a given discharge channel inductance, larger capacitors simply take longer to discharge. As we mentioned above, though, the time scales of interest for many HEDP applications are $\sim$100 ns. Thus, pulse compression is needed.

On Z, pulse compression is achieved primarily through the use of pulse-forming lines (PFLs). The operating principles behind a PFL are illustrated in Fig. 13, while more general transmission line theory is provided in Appendix C. On Z, the long, $\sim$1-μs, output pulse from a given Marx generator is used to charge a coaxial PFL (labeled as "ISC" for *intermediate storage capacitor* in Fig. 9). When the ISC is fully charged, a laser-triggered gas switch (LTGS) is closed, and the ISC begins discharging into a shorter coaxial PFL (labeled as "PFL" in Fig. 9). The discharge time of the ISC is roughly 200 ns, while the discharge time of the subsequent PFL is roughly 100 ns; hence, the ISC is approximately twice the physical length of the subsequent PFL. Both the ISC and the PFL are water insulated to maximize the energy storage as well as to achieve the desired pulse duration in a physically short line length. Water is a good choice for the dielectric/insulating medium for several reasons. First, water can be pumped into or out of the large metal ISC and PFL structures. This makes servicing the ISCs and PFLs more manageable. Also, if an arc occurs in the water, producing carbon and other contaminating particulates in the water, then the water can be easily filtered, cleaned, and/or replaced. Second, water has a high dielectric permittivity ϵ, and the electric field energy stored in a capacitor is given by $\mathcal{E}_E = (1/2)CV^2 \propto \epsilon$ [cf. (9) and (59)]. Thus, more energy can be stored in a water dielectric medium than in vacuum, for example. Third, a higher permittivity means that a physically shorter length of transmission line can be used for a given pulse duration, since the pulse duration scales as $\sqrt{LC} \propto \sqrt{\epsilon}$. This reduces the material costs and the physical space needed to fit a machine of a given electrical energy and pulse duration.
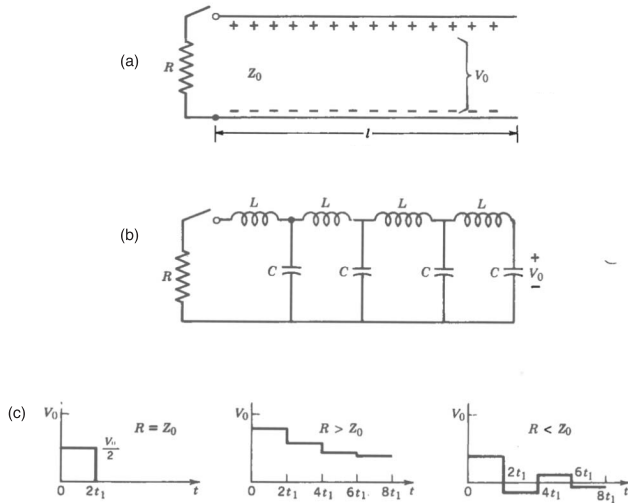
Fig. 13. Illustrations representing the operating principles of a pulse-forming line (PFL). Prior to the discharge triggering event, the long transmission line, with a characteristic impedance Z_0 (see Appendix C), is charged from one end (the input end) while the other end (the output/load end) is connected to a high-power switch, which is in an open state. Once the line is fully (and uniformly) charged to the desired voltage, V_0, the charging supply is disconnected from the input end of the line. This leaves both ends of the now fully charged line in an open state. At this point, the output switch is triggered closed. This allows the charged transmission line to start discharging into the load (or into a larger pulsed-power system's next stage). For a matched load ($R = Z_0$), the open-circuit charging voltage V_0 is split evenly across the two equal impedances (Z_0 and R), which are now in series with each other. The result is that a voltage $V_0/2$ appears across the load R for a duration $\tau_d = 2t_1$, where t_1 is the one-way transit time of the line (see Appendix C). The duration is twice the electrical length of the line because this is the time it takes for an electromagnetic wave, with a voltage amplitude of $-V_0/2$, to propagate from the disturbance (from the output end of the line where the switch has closed) back up the line to the now open-circuited charging end of the line, where it is then fully reflected back towards the load end of the line. Upon returning to the load, the voltage is zeroed. This phenomenon occurs because of *transit time isolation*—i.e., the minimal time required for information to propagate from one end of the line to the other is limited by the speed of light in the medium, and the speed of light in the medium *is* the propagation velocity of the electromagnetic wave that is launched when the output switch is closed. That is, the charging end of the line knows nothing about the switch closing until the backward-propagating electromagnetic wave reaches the charging end of the line. Thus, the charging end of the line remains at a value of V_0 until the backward-propagating $-V_0/2$ wave reaches the charging end. Because of the superposition principle in fundamental electricity and magnetism, voltages add linearly. Thus, on the first pass, the backward-propagating $-V_0/2$ wave consumes half of the line's initial $+V_0$. Then, after reflecting off of the open-circuited charging end of the line, the now forward-propagating $-V_0/2$ wave consumes the line's remaining $+V_0/2$, which reduces the line's voltage to zero just behind the wavefront. For cases where $R \neq Z_0$, longer duration discharges ($R > Z_0$) and/or ringing discharges ($R < Z_0$) can occur. (Source: [62].)

Referring to Fig. 9, we see that each Marx generator is connected in series to a single ISC-PFL combination. We refer to this arrangement as a Marx-generator/PFL module. The Z machine contains 36 Marx-generator/PFL modules. These 36 modules are arranged electrically in parallel with each other, through a series of connecting structures downstream of the modules. Each module feeds power radially inward from the machine's outer tank towards the machine's vacuum section, where experimental loads (or "targets") are positioned.

From Fig. 9, we see that each PFL is discharged through a self-breaking main water switch into a flat and balanced triplate structure called "output transmission line 1" (OTL1). Each OTL1 is discharged through a peaking water switch into a second flat and balanced triplate structure called "output transmission line 2" (OTL2). The OTL2s combine pairs of OTL1 outputs into single OTL2 outputs through a simple "Y" connection. Each of the 36 OTL2 inputs has an impedance of 6.4 Ω, while each of the 18 OTL2 outputs has an impedance of $(6.4/2)\,\Omega = 3.2\,\Omega$ [1]. Considering the 36 parallel Marx-generator/PFL modules (or the 18 parallel OTL2 outputs), these impedances result in an overall Z facility driver impedance of $Z_z = (6.4/36)\,\Omega = (3.2/18)\,\Omega = 0.18\,\Omega$ [1].

From Fig. 9, we see that the OTL2 outputs feed the water convolute. In pulsed power, *convolutes* make complex ("convoluted") electrical connections, which usually involve some complex 3-D geometry to reduce the number of parallel current paths in the system. On the Z machine, the water convolute makes the "convoluted" connections from the 18 electrically parallel OTL2 outputs to the 4 electrically parallel levels of the water–vacuum insulator stack. The water convolute also rotates the driving electric fields by approximately 90°, from being approximately horizontal in the OTL2 triplate structures to being approximately vertical in the water–vacuum insulator stack [1]. Note that on the Z machine, there is also a second convolute, called the "double post-hole convolute," which resides in the vacuum section of the machine (see Fig. 10); this convolute is described in more detail below.

The water–vacuum insulator stack separates the water-insulated section of the machine from the vacuum-insulated section of the machine (see Figs. 9 and 10). At this interface, the three metal anodes and the two metal cathodes are insulated from each other by four stacks of alternating dielectric insulator rings and metal voltage-grading rings (the grading rings "float" electrically between the anode and cathode potentials). The water–vacuum insulator stack is connected to four electrically parallel, vacuum, self-magnetically insulated transmission lines (self-MITLs) [84].

In the vacuum section, the four-level MITL system is combined into a single inner MITL feed by a double post-hole convolute (~1 ft in size). Vertical anode posts (gray) passing through the cathode holes (red) of the convolute combine the four anode plates (blue) together into the single top electrode of the inner MITL feed. The cathode "*skirt*" (which is the red cylinder residing just within the radial position of the gray anode posts) combines the two cathode plates (red) into the single bottom electrode of the inner MITL feed. Finally, the inner MITL feed connects to the experimental load under test (e.g., a Z-pinch target or a material sample for a material properties experiment).

In Fig. 10, the four power levels of the MITL system are indicated by the labels A, B, C, and D. It may seem confusing at first that there can be four power levels and only two cathode plates (red) and, likewise, that there can be four power levels and only three anode plates (blue). However, the key to understanding this is to recall that we are dealing with surface currents, due to our 100-ns time scales, and the image presented in Fig. 10 represents only one azimuthal slice of a structure that is azimuthally continuous about the center line. Thus, one cathode plate (red) can serve two power levels

by using the top and bottom surfaces of the cathode plate independently. The same goes for the middle anode plate.

The reason that four parallel MITLs and a double post-hole convolute are used in the vacuum section, rather than just a single MITL and no post-hole convolute, is that the multilevel arrangement reduces the overall inductance of the vacuum section. This can be understood by first considering the inductance of a single level, L_{single}. Then, with four of these levels in parallel with each other, the equivalent inductance of the four-level MITL system is $L_{\text{equiv}} = L_{\text{single}}/4$. This helps to maximize the amplitude and shorten the rise time of the current pulse delivered to the load.

The use of a post-hole convolute also means that the power flow coming from the MITL section will experience a large impedance discontinuity at the convolute. The magnetically insulated electron flow in each of the four MITL levels can be lost to the anode posts in the convolute. This represents a shunt current loss. This loss occurs because magnetic insulation is lost in the convolute. Magnetic insulation is lost in the convolute because magnetic nulls (regions where $B = 0$) exist in the A–K gaps of the convolute. The magnetic nulls are the result of a topological change in the **B** field, which is the result of combining four parallel current paths into a single current path. Because of the loss of flow electrons, it is important to keep the electron flow impedance as high as possible to keep the electron flow current as low as possible (which keeps the current loss in the convolute as low as possible). Establishing a better understanding of convolute physics is presently a very important area of research at Sandia [85]–[88], especially when considering the construction of new machines with currents much larger than today's Z facility [36].

Note that even though we are reviewing the Z facility as an example of a Marx-generator/PFL-based architecture, much of this discussion will be germane to an LTD-based design as well. This includes the use of water insulation for greater energy storage and transmission as well as the use of a water–vacuum insulator stack, a multilevel MITL system, a post-hole convolute, and an inner MITL final feed. Here we also note that the ISCs and PFLs in the Z facility are essentially cylindrical capacitors that are discharged into the inductive vacuum cavity of the machine. Thus, this system is similar to (but not exactly equivalent to) our simple LC model discussed in Section III. The PFL discharge is different from a simple LC discharge because the series inductance and the parallel capacitance of the PFL are distributed along the physical length of the PFL. This is represented by the LC ladder network shown in Fig. 13(b). The distributed LC network leads to the transit-time-isolated discharge characteristics presented in Fig. 13. The result is a more "flat-topped" voltage pulse than that generated by a simple LC discharge. The difference in voltage waveforms corresponds to a difference in current waveforms as well. In Marx-generator/PFL-based architectures, the current waveform is often well approximated by a sine-squared waveform [i.e., $I(t) \approx I_0 \sin^2(\omega t)$], while the simple LC discharge produces a sine waveform [i.e., $I(t) = I_0 \sin(\omega t)$]. It is important to note that the time to peak electrical power [$P(t) = V(t) \times I(t)$] for the sine and the sine-squared current pulses into a static inductive load are,
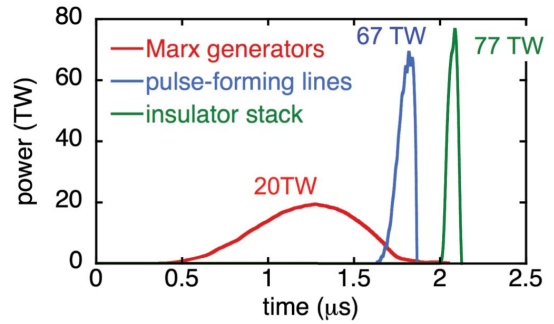

Fig. 14. Power flow through three stages of the Z machine. These stages correspond to those shown in Fig. 9. This figure illustrates the principle of power amplification through pulse compression in time.

respectively, $(1/2)\tau_{\text{peak}}$ and $(2/3)\tau_{\text{peak}}$, where τ_{peak} is the time to peak current. This means that the time of peak electrical power is closer to the time of peak electrical current for the sine-squared pulse. Since the time of peak electrical current is often the time of peak magnetic pressure, this timing could be important for various Z-pinch loads (see the discussion at the end of [89], for example). In Section V, we will see that LTDs are very similar to our simple LC model of Section III, thus LTDs produce a sine-shaped current waveform (unless special LTD pulse-shaping techniques are employed; see, for example, Fig. 24 as well as [30] and [35], where [35] in particular discusses how to generate "flat-topped" square-wave-like voltage and current pulses from an LTD).

When thinking about all of the various stages and connections in the Z machine, it is helpful to recall what we mentioned at the end of Section III: voltages are combined in series for voltage addition, currents are combined in parallel for current addition, both voltages and currents are increased together for power amplification, and pulsed-power for HEDP applications usually involves energy compression in both *time* and *space*. For example, in a Marx generator, the voltage is amplified from U_0 to nU_0 via a fast parallel-to-series reconfiguration. This is a voltage amplification factor of $n = 60$ for the Marx generators on the Z machine. Additionally, since the Marx capacitors on the Z machine are charged from the power grid on a time scale that is ~1 min and discharged in an output pulse that is ~1 μs, this is an example of energy compression in *time*.

Another example of energy compression in *time* is the use of PFLs. The power amplification due to the PFLs on Z is illustrated in Fig. 14. Recalling that the Z machine stores ≈20 MJ of electrical energy in its fully charged Marx generators, we see that this energy is spread out broadly across ~1 μs when the Marx generators discharge. This results in a relatively low peak power of only 20 TW. The PFLs, however, then reduce the pulse length from ~1 μs down to ~100 ns, while simultaneously conserving much of the total energy in the pulse. This pulse compression technique amplifies the peak power to roughly 80 TW (more than the power generating capacity of the entire world's power plants combined).

As an example of current amplification, consider the Z machine's 36 parallel current paths (from the 36 parallel Marx generator/PFL modules) as they are combined into a single current path at the load. Thus, the overall current

amplification factor for the machine is roughly 36. These parallel path connections occur at the following locations in the machine: 1) at the OTL1 to OTL2 transition (taking 36 parallel current paths down to 18 for a current amplification factor of 2); 2) at the water convolute (taking 18 parallel current paths down to 4 for a current amplification factor of 4.5); and 3) at the double post-hole convolute section (taking the 4 parallel MITL levels down to a single inner MITL feed for a current amplification factor of 4). Note that this process is also an example of energy compression in *space*. That is, consider all of the electrical charge Q stored in the Marx generator capacitors around the perimeter of the machine (which is 33 m in diameter). This stored charge is discharged in an electrical current $I = dQ/dt \sim 25$ MA that is focused towards the load at the center of the machine (usually a load/target with ~ 1 cm scale size). This results in very intense current densities $J(r, t)$ (or dQ/dt per m^2), very intense magnetic field pressures $p_{\text{mag}} = B^2/(2\mu_0)$, and very large energy densities $\mathcal{E}_B(r, t) = p_{\text{mag}}(r, t)$. And, as mentioned above, the process of target implosion and stagnation further compresses energy in both time and space.

Here we also note that the trigger timing for each of the 36 parallel Marx generator/PFL modules can be controlled nearly independently of one another (for example, by changing the relative timings of the 36 laser-triggered gas switches). Because of this, and because the currents from the 36 modules add approximately linearly, the Z facility is capable of delivering custom-designed pulse shapes to loads. The duration of these pulse shapes can be extended out to ~ 1 μs.

In the end, the Z pulsed-power facility delivers ~ 3 MV to the vacuum section of the machine, with an overall driver impedance of about 0.18 Ω. This results in an electrical current pulse that rises from 0 to 25 MA in ~ 100 ns (or a shaped pulse that can be modulated out to ~ 1 μs; note that the voltage and driver impedance change somewhat for longer pulse shapes [1]). This current pulse is applied to various loads to generate magnetic drive pressures on the order of 100's of Mbar. The various loads investigated enable research efforts in ICF [7], [10], [90]–[92], pulsed-power physics [27], Z-pinch physics [93], [94], radiation effects [15], radiation physics [13], [14], laboratory astrophysics [95], dynamic material properties [96]–[98], and other HEDP applications [90], [99]. The Z accelerator is also very efficient, coupling upwards of 15% of its stored ≈ 20 MJ of electrical energy to well-matched loads—i.e., delivering roughly 1–3 MJ to well-matched loads. This is equivalent to a few sticks of dynamite going off in the vacuum chamber of the machine every experiment. This energy release produces a harsh debris environment that must be mitigated for sensitive experimental equipment, including sensitive diagnostics.

In addition to the Z facility at Sandia, there are several university-scale Marx-generator/PFL-based pulsed-power machines that are used to study HEDP. Some examples (see Fig. 15) include the ~ 1-MA, 250-ns MAGPIE generator at Imperial College London, U.K. [100], [101], the ~ 1-MA, 100-ns ZEBRA generator at the University of Nevada, Reno [102], [103], and the ~ 1-MA, 100-ns COBRA generator at Cornell University [104]. Note that MAGPIE uses four Marx

generators and four coaxial PFLs, ZEBRA uses a single Marx generator and a single coaxial PFL, and COBRA uses two Marx generators and four coaxial PFLs. The driver impedance of these Marx/PFL-driven systems is typically characterized by

$$Z_{\text{driver}} = \frac{Z_{\text{pfl}}}{N_{\text{pfls}}} \quad (65)$$

where Z_{pfl} is the characteristic impedance of a single coaxial PFL (see Appendix C) and N_{pfls} is the number of PFLs connected in parallel at the load. Thus, the driver impedance for MAGPIE is $Z_{\text{magpie}} = (5/4)\,\Omega = 1.25\,\Omega$, the driver impedance for ZEBRA is $Z_{\text{zebra}} = (1.9/1)\,\Omega = 1.9\,\Omega$, and the driver impedance for COBRA is $Z_{\text{cobra}} = (1.8/4)\,\Omega = 0.45\,\Omega$. The total pre-shot capacitance of these facilities is about 67 μF for MAGPIE and about 43 μF for ZEBRA and COBRA. The total preshot energy storage for these facilities is ~ 100–300 kJ, depending on the charge voltage used (which is typically in the range of 70–100 kV).

Before leaving this section, we note that the PFL storage and switching complexity in a traditional Marx-driven system are needed only to reduce the pulse rise time from ~ 1 μs to ~ 100 ns. As we will see, the beauty of an LTD-based system is that these pulse compression techniques (with their inherent energy inefficiencies) are no longer needed. This is because the LTD generates a pulse that is already ~ 100 ns right from the primary storage capacitors, due to the use of many small (and therefore fast) storage capacitors arranged electrically in parallel with each other.

V. INTRODUCTION TO LINEAR TRANSFORMER DRIVERS

The architecture of a single, modern LTD cavity is very similar to the illustrations shown in Fig. 1, where many fast switches and capacitors are distributed around the perimeter of an inductive, cylindrical metal cavity. During our discussion of a simple LC model, presented in Section III, we noted that in order to achieve a high-amplitude, fast-rising current pulse (to achieve the highest drive pressure at the fastest rate), we needed to have a system with low L and large C (large C for large charge storage Q). What makes modern LTD cavities special is that the switches, capacitors, power feed, and load are all packaged together very compactly *within* the metal cavity itself, while simultaneously achieving very low L and large C through the use of many parallel channels of small and fast capacitors and switches.

An example of the efficient, highly parallel packaging within an LTD cavity is presented in Fig. 16. This single-cavity LTD system is the Michigan Accelerator for Inductive Z-pinch Experiments (MAIZE) at the University of Michigan [29]. The low L and large C is achieved by distributing many small and fast capacitors and switches around the perimeter of the 3-m-diameter machine. The use of many small capacitors (and switches) in parallel keeps the overall L low while simultaneously providing a large effective surface area for a large overall C. The large C enables a large overall charge storage $Q = CV$. During a discharge, all of the Q in these capacitors is rapidly focused towards the load at the center of the machine to achieve a high current density J (i.e., high dQ/dt per m^2).
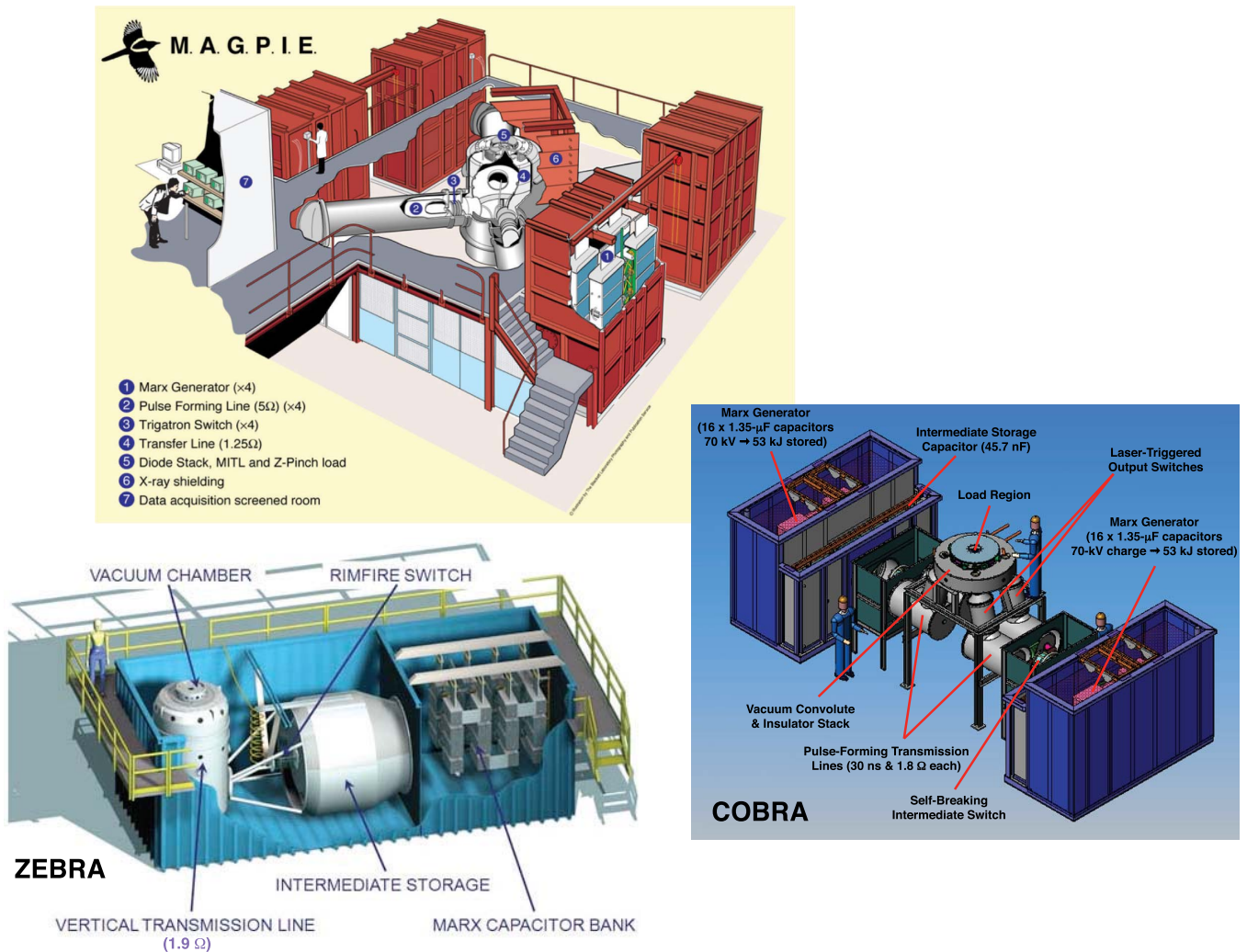
Fig. 15. Graphical representations of some of the largest university-scale (∼1 MA) Marx-generator/PFL-based facilities used for studying HEDP (these are *not* LTD facilities). Shown are the ∼1-MA, 250-ns MAGPIE generator at Imperial College London, U.K. [100], [101], the ∼1-MA, 100-ns ZEBRA generator at the University of Nevada, Reno [102], [103], and the ∼1-MA, 100-ns COBRA generator at Cornell University, [104].

The small overall inductance on MAIZE is also obtained by keeping the volume of the vacuum power feed small. That is, both the A–K gap spacing d and the overall axial translation from the capacitors to the load Δz are kept small. The result is a power feed that is primarily radial. Note that there is some small Δz in the MAIZE power feed of Fig. 16 (top), such that the load is lifted just above the horizontal plane of the capacitors and switches, but this is done solely to provide the diagnostics with an unobstructed side-on view of the load during an experiment. Also note that if a Δz translation such as this must be done, then it is best to locate the translation at a large radius to reduce the associated increase in inductance. To understand why this is the case, consider (11) and (14) and evaluate $L(r_{in})$ for a constant A–K gap spacing $d = r_{out} - r_{in}$ and a constant/given $\Delta z = h$; the inductance will be smaller at larger r_{in}. For this reason, most of the Δz translation on MAIZE is done at a large radius (i.e., right near the capacitors)—see Fig. 16 (top).

The capacitors and switches distributed around the perimeter of an LTD cavity are grouped together in power units called *bricks*. Each brick consists of two capacitors (a top and bottom capacitor) connected electrically in series with each other through a gas-filled spark-gap switch.[2] The MAIZE facility consists of 40 bricks, thus MAIZE has 80 capacitors and 40 spark-gap switches (see Fig. 16). LTD bricks (and the capacitors and switches that comprise them) continue to be developed to this day. For example, Sandia has now developed a brick capable of storing up to 800 J of electrical energy and supplying up to 5 GW of electrical power [see Fig. 17(a)].

Bricks are also now being used to drive various applications directly (i.e., without an LTD cavity). For this reason, bricks represent a true LTD spinoff technology. Some examples include bricks driving very long coaxial cables, such that the bricks are transit-time isolated from the loads. By connecting several of these brick-driven cable lines together in parallel at the load, precise control over pulse shaping can be achieved. These machines are typically referred to as cable pulsers [105].

---

[2]Note that it is not necessary for bricks to have two capacitors. See [23] and [38] for examples of bricks with just a single capacitor.
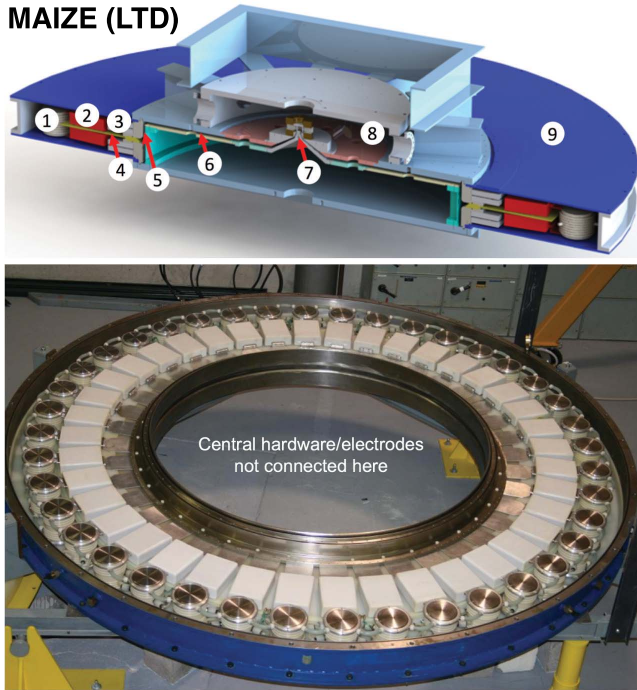
Fig. 16. (top) Cross section of the 3-m-diameter MAIZE LTD [29]. 1: spark gap switch—40 such switches in the LTD. 2: 40-nF capacitor—80 such capacitors in the LTD. 3: iron core—2 cores in the LTD. 4: high voltage insulator. 5: coaxial transmission line section. 6: radial transmission line section. 7: load region with conical power feed. 8: 1-m-diameter vacuum chamber. 9: oil chamber. (bottom) Photograph of the MAIZE cavity (without the lid, center electrodes, load, or vacuum chamber). This photo shows the 40 power units called *bricks* distributed around the perimeter of the machine. Each brick consists of two capacitors (a top and bottom capacitor) and one gas-filled spark-gap switch. In this photograph, only the top capacitors can be seen (white squares). Additionally, the tops of the spark-gap switches can be seen (shiny circles next to the white square capacitors).

Bricks are also now being used to drive X-pinches for portable and efficient radiography sources [106], [107].

An equivalent circuit model for a brick is presented in Fig. 17(b). One of the capacitors in a brick is charged to $+V_c$ while the other is charged to $-V_c$. When the spark-gap switch is closed, the capacitor voltages add in series with each other so that the output voltage is

$$|V_0| = 2|V_c|. \tag{66}$$

In some sense, then, the brick can be thought of as a two-stage unipolar Marx generator or a single-stage bipolar Marx generator (cf. Figs 11 and 12). Also note that since the capacitors are in series with each other, the capacitance of each brick is

$$C_{\text{brick}} = \frac{C_{\text{cap}}}{2} \tag{67}$$

where C_{cap} is the capacitance of a single capacitor within the brick.

On MAIZE, the capacitors are each 40 nF, which means that $C_{\text{brick}} = 20$ nF. Since there are 40 bricks in parallel on MAIZE ($N_{\text{bricks}} = 40$), we have $C = N_{\text{bricks}} \times C_{\text{brick}} = 800$ nF. Typically, to minimize the damage on MAIZE, the capacitors are charged to no more than $V_c = \pm 70$ kV, so that $|V_0| = 2|V_c| \leq 140$ kV. For a well-matched, low-inductance load on MAIZE,
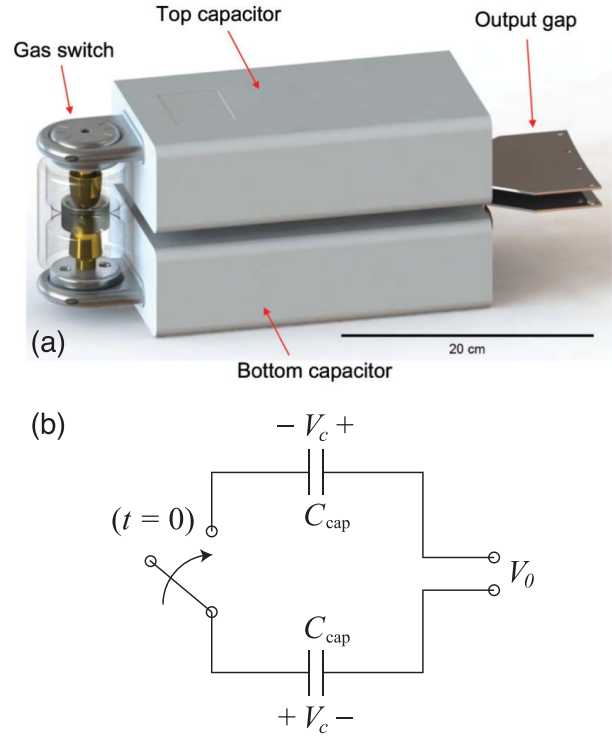
Fig. 17. (a) A Sandia brick design capable of storing up to 800 J of electrical energy and supplying up to 5 GW of electrical power. (b) An equivalent circuit model for a single brick.

we typically have $L \approx 20$ nH. Thus, plugging these values into our simple LC model from Section III, we find $Z_0 = \sqrt{L/C} \approx 0.16$ Ω, $I_{\text{peak}} = V_0/Z_0 \approx 900$ kA, and $\tau_{\text{peak}} = (\pi/2)\sqrt{LC} \approx 200$ ns. These results agree reasonably well with experiments conducted on MAIZE [29], [108]–[112], especially given the simplicity of the LC model. Note that with $V_c = \pm 70$ kV ($|V_0| = 2|V_c| = 140$ kV), the initial energy stored in the MAIZE capacitors is

$$E_{\text{store}} = \frac{1}{2}CV_0^2 \approx 8 \text{ kJ}. \tag{68}$$

Also note that MAIZE is capable of $V_c = \pm 100$ kV, in which case $E_{\text{store}} \approx 16$ kJ. Additionally, in the near future, we are looking to upgrade MAIZE to 80-nF capacitors and higher voltage switches. In this case, with $V_c = \pm 100$ kV, MAIZE would have $Z_0 \approx 0.11$ Ω, $I_{\text{peak}} \approx 1.8$ MA, $\tau_{\text{peak}} \approx 280$ ns, and $E_{\text{store}} \approx 32$ kJ, all from a 3-m-diameter package.

One thing that is not shown in the brick circuit model of Fig. 17 is that each brick has its own inductance L_{brick} and resistance R_{brick}. However, all of the bricks in an LTD cavity are combined in parallel, thus $L_{\text{equiv}} = L_{\text{brick}}/N_{\text{bricks}}$ and $R_{\text{equiv}} = R_{\text{brick}}/N_{\text{bricks}}$. For MAIZE, $N_{\text{bricks}} = 40$, $L_{\text{brick}} \approx 240$ nH, and $R_{\text{brick}} \approx 660$ mΩ; therefore, $L_{\text{equiv}} \approx 6$ nH and $R_{\text{equiv}} \approx 16.5$ mΩ [110]. This means that about half of the overall ≈20-nH LTD cavity inductance on MAIZE is from the bricks and the outer regions of the power feed, while the remaining half comes from the inner power feed and the load. Note that the outer ≈10-nH inductance on MAIZE is essentially fixed, while the inductance of the inner power feed and load can vary significantly from one experimental

configuration to the next—e.g., from 8 to 23 nH for some of the configurations tested on MAIZE so far [110]. Also note that the L/R time on MAIZE is $\tau_{L/R} = L/R \approx 1.2 \ \mu s \gg \tau_{peak}$ (meaning the voltage is primarily an inductive voltage: $V \approx L\dot{I} + I\dot{L} \gg IR$) while the RC time constant is $\tau_{RC} = RC \approx 26$ ns $\ll \tau_{peak}$ (meaning the capacitors can discharge and recharge fast enough to support resonant oscillations). Thus, the effect of R is small and the discharge dynamics of the LTD cavity will be dominated by the simple LC characteristics described above; that said, R is not zero, and thus some damping of the resonant oscillations will occur. Finally, we note that the inductance of a single brick L_{brick} is predominantly due to the switch's inductance, since the switch's inductance is much larger than the capacitor's inductance (i.e., $L_{brick} = L_{switch} + L_{cap} \approx L_{switch}$, since $L_{switch} \gg L_{cap}$).

It is important to understand that the LTD's rise time τ_{peak} is largely determined by the rise time of the bricks themselves; i.e., $\tau_{peak} \sim \tau_{brick} \equiv (\pi/2)(L_{brick}C_{brick})^{1/2}$. The reason for this can be understood as follows. Since the bricks are connected electrically in parallel within the LTD cavity, we have $L_{equiv} = L_{brick}/N_{bricks}$ and $C = N_{bricks}C_{brick}$. Using L_{rest} to represent the inductance of everything other than the bricks, we have

$$\tau_{peak} = \frac{\pi}{2}\sqrt{LC} = \frac{\pi}{2}\sqrt{(L_{rest} + L_{equiv})C}$$
$$= \frac{\pi}{2}\sqrt{\left(L_{rest} + \frac{L_{brick}}{N_{bricks}}\right)(N_{bricks}C_{brick})}$$
$$= \frac{\pi}{2}\sqrt{L_{rest}N_{bricks}C_{brick} + L_{brick}C_{brick}}. \quad (69)$$

If we now neglect L_{rest} (i.e., if we assume a low-impedance load and a low-impedance power feed), then we have

$$\tau_{peak} \sim \frac{\pi}{2}\sqrt{L_{brick}C_{brick}} \equiv \tau_{brick}. \quad (70)$$

This result states that the LTD's overall rise time τ_{peak} is largely independent of the number of bricks used, since N_{bricks} cancels out of (70). That is, as more bricks are placed electrically in parallel with each other, the reduction in $L = L_{rest} + L_{equiv}$, due to the reduction in L_{equiv}, almost exactly compensates for the increase in C, thus leaving $\tau_{peak} = (\pi/2)\sqrt{LC}$ largely unchanged. The fact that the overall rise time τ_{peak} is largely determined by τ_{brick} means that in order to have a fast rise time, we need to have small values of both L_{brick} and C_{brick}. In practice, a machine designer typically controls the rise time of a facility by selecting an appropriate value for C_{brick} and then compensating for this selection by also selecting an appropriate number of bricks to be placed electrically in parallel with each other, since $C = N_{bricks}C_{brick}$. This is done because the values for C_{brick} and N_{bricks} are typically easier to control than the value of $L_{brick} \approx L_{switch}$. For example, there is a practical minimum to how small (and thus how fast) $L_{brick} \approx L_{switch}$ can be made.

Another important scaling to be aware of is that the LTD's peak current I_{peak} is largely determined by both N_{bricks} and the current of each brick, $I_{brick} = V_0/Z_{brick} = V_0(C_{brick}/L_{brick})^{1/2}$, where $Z_{brick} \equiv (L_{brick}/C_{brick})^{1/2}$.

This scaling can be seen from

$$I_{peak} = \frac{V_0}{Z_0} = V_0\sqrt{\frac{C}{L}} = V_0\sqrt{\frac{C}{L_{rest} + L_{equiv}}}$$
$$= V_0\sqrt{\frac{N_{bricks}C_{brick}}{L_{rest} + L_{brick}/N_{bricks}}}. \quad (71)$$

If we again neglect L_{rest}, then we have

$$I_{peak} \sim V_0 N_{bricks}\sqrt{\frac{C_{brick}}{L_{brick}}} = N_{bricks}I_{brick}. \quad (72)$$

This scaling is consistent with the fact that multiple current channels add linearly when combined in parallel.

Referring to (70) and (72), we find that if we want a current pulse with both a large amplitude and a short rise time (i.e., a large I_{peak} and a short τ_{peak}), then we need a large number of bricks connected electrically in parallel, where each brick has a small inductance and a small capacitance. That is, we want N_{bricks} to be large for a large I_{peak}, and we want L_{brick} and C_{brick} to be small for a short τ_{peak}. Again we note that the small individual brick capacitance (small C_{brick}) is compensated for by the large number of bricks in parallel (large N_{bricks}). This compensation maintains the large overall capacitance needed for a large amplitude current pulse (i.e., a large I_{peak} requires a large $C = N_{bricks}C_{brick}$). If we instead want a long τ_{peak} with our large I_{peak}, then the large $C = N_{bricks}C_{brick}$ required for our large I_{peak} can be obtained with either a large value of N_{bricks} or a large value of C_{brick} (or both). In many cases, a large value of N_{bricks} can be traded for a large value of C_{brick}, and vice versa, depending on the capacitor sizes available and the overall packaging constraints of the LTD.

A defining characteristic of LTD cavities is that their components (i.e., their switches, capacitors, power feed, and load) are fully enclosed in the cavity's metal casing. This means that electromagnetic fields and other noise sources straying from the cavity are minimized. This reduces interference with other experimental equipment outside of the casing, even when the equipment is in close proximity to the cavity.

In order to fully enclose the pulsed power fields within the metal casing, the LTD concept relies on the use of ferromagnetic cores with high magnetic permeability μ. These cores are used to increase the inductance of an alternative (undesired/parasitic) current path that is in parallel with the primary (desired) current path, which runs to the load. In essence, the cores act as ferromagnetic "chokes." There are typically two cores per LTD cavity (see Fig. 18).

To understand the two parallel current paths within an LTD cavity, see Figs. 17 and 18 and consider the geometry of the brick's output electrodes (Fig. 17). To be clear, we are still talking about surface currents; however, the output electrodes of the bricks occupy only discrete azimuthal locations about the centerline of the LTD (i.e., the discrete number of bricks means that the metal of the bricks' output electrodes is not azimuthally continuous about the centerline of the cavity). This means that the surface currents flowing out of the brick's capacitors can flow onto either the top or bottom surfaces of
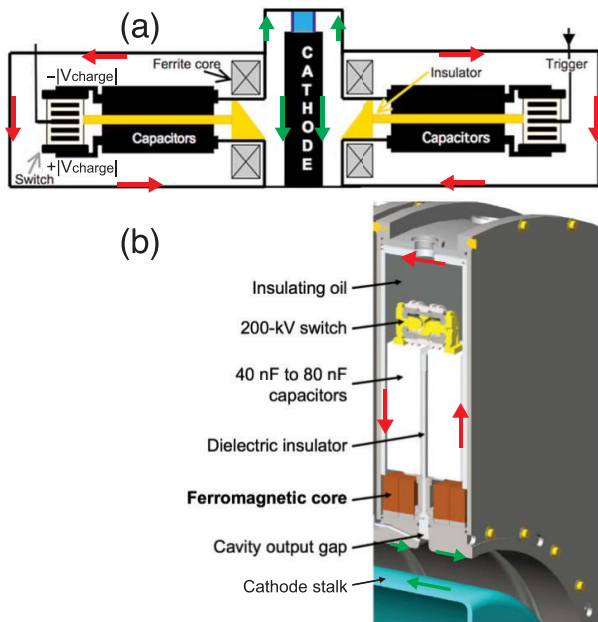
Fig. 18. (a) An axisymmetric cross section including two bricks (left and right), ferromagnetic cores, and other components housed inside an LTD casing. (Source: [32].) (b) A 3-D model of a brick, ferromagnetic cores, and other components housed within an LTD cavity. (Source: [36].) These graphics illustrate the two possible surface current paths within an LTD cavity. They also illustrate how the high-μ ferromagnetic cores increase the inductance (impedance) of the undesired/parasitic surface current path (red arrows) and force the current to take the desired lower inductance surface current path through the load (green arrows). This arrangement with high-μ cores is necessary if one wants to completely enclose all of the pulsed-power fields within the LTD's metal casing while minimizing the overall volume of the casing. Note that in (a) (and in Fig. 17), before the switch is closed, the top of the switch is charged to $-|V_{\text{charge}}|$, the bottom of the switch is charged to $+|V_{\text{charge}}|$, and both of the brick's output electrodes are at dc ground potential (grounded through the LTD's metal casing for the long timescales associated with charging). When the switch is closed, the potential difference across the switch drops rapidly to zero, pushing the brick's top output electrode to $+|V_{\text{charge}}|$ and the brick's bottom output electrode to $-|V_{\text{charge}}|$. The resulting direction of the positive surface current flow during the discharge is as indicated by the red and green arrows in (a) and (b).

the brick's upper and lower output electrodes. For example, current can flow out of the top capacitor onto the top surface of the brick's upper electrode. This surface current can then take the undesired/parasitic path that encircles the brick and returns to the bottom capacitor by flowing onto the bottom surface of the brick's bottom electrode. This parasitic path is along the inner surface of the LTD's metal casing, including the inner surface of the LTD's outer wall, which is at a machine radius that is larger than the radial location of the bricks. For the desired current path through the load, the current would flow out of the top capacitor onto the bottom surface of the brick's top electrode, and it would return to the bottom capacitor by flowing onto the top surface of the brick's bottom electrode. For both paths, the circuit is completed through the closed spark-gap switch.

If the high-μ cores were not used, and the volume encircled by the parasitic current path was filled with vacuum, then we would have $\mu = \mu_0$. In this case, the parasitic current path could have an inductance that is comparable to that of the load, which would then divert much of the overall machine current away from the load. The fact that the parasitic path could have

a low inductance, when filled with vacuum, can be understood by referring to (11) and (14) and again considering the case of $L(r_{\text{in}})$ for a constant A–K gap spacing $d = r_{\text{out}} - r_{\text{in}}$ and for a given/constant axial extent $h = \Delta z$; we would again find that the inductance is reduced as r_{in} is increased. However, we can raise the inductance of this parasitic large-radius current path simply by filling the volume of this path with a ferromagnetic material that has $\mu \gg \mu_0$. To see this, we can again refer to (11) and (14); only this time, we let $\mu_0 \to \mu \gg \mu_0$.

In practice, the ferromagnetic cores are often premagnetized prior to an LTD pulse. That is, prior to an LTD pulse, a separate and independent premagnetization generator is used to drive the B_θ field within the cores to run in a direction that is antiparallel to the direction of the B_θ field generated by the LTD itself during the LTD discharge. This is done so that, during the LTD pulse, the LTD's driving B_θ field must do work to reverse the direction of the fields in the ferromagnetic cores. Essentially, premagnetization maximizes μ and thus maximizes the inductance of the parasitic current path prior to the LTD pulse. To understand why this maximizes μ, recall that ferromagnetic materials exhibit hysteresis in their $B = \mu H$ curves, where B is the magnetic flux density, and H is the magnetizing magnetic field intensity [62]. Additionally, since we are dealing with pulsed currents, there is a time-lag effect. In this case, μ can be treated as a complex quantity, with a real part and an imaginary part (or, equivalently, the complex μ relates a complex B to a complex H through its magnitude and phase information). During the LTD pulse, the B_θ field generated by the LTD begins to reverse the field within the premagnetized cores. As the B_θ field within the cores begins to align with the driving B_θ field generated by the LTD pulse, the value of μ in the cores begins to fall along the trajectory specified by the core material's complex hysteresis curve. Once the B_θ fields within the cores have fully aligned with the B_θ field generated by the LTD pulse, the cores are said to have *saturated*. At saturation, μ is minimized, and thus saturation should be avoided. In fact, if μ falls too rapidly relative to the LTD's pulse duration, then the isolation from the parasitic current path can be lost during the LTD pulse, and much of the LTD's total current can then be diverted into the parasitic path, rather than to the load. Thus, it is important to design an LTD with enough core material for the desired LTD pulse length and amplitude, so that this "core saturation" condition can be avoided. It is also important to note that associated with the cores are resistive-like energy losses due to the hysteresis curve and Eddy currents [33]; these losses can be modeled using a resistor element $R_{\text{core}}(t)$ in the circuit modeling of an LTD (see, for example, [32], [33], and [110]).

The low L and high C of an LTD cavity means that a *single* LTD cavity is a low-impedance driver, since $Z_{\text{cavity}} = (L_{\text{cavity}}/C_{\text{cavity}})^{1/2}$ [see (30)]. However, another advantage of the LTD packaging is that it enables several *cavities* to be stacked on top of one another to form an LTD *module* (see Fig. 19). Stacking multiple cavities together in series increases the impedance and output voltage of the overall driver while leaving the current nominally unchanged. The module output voltage increases linearly with the number of cavities used because the cavity output gaps are stacked on top
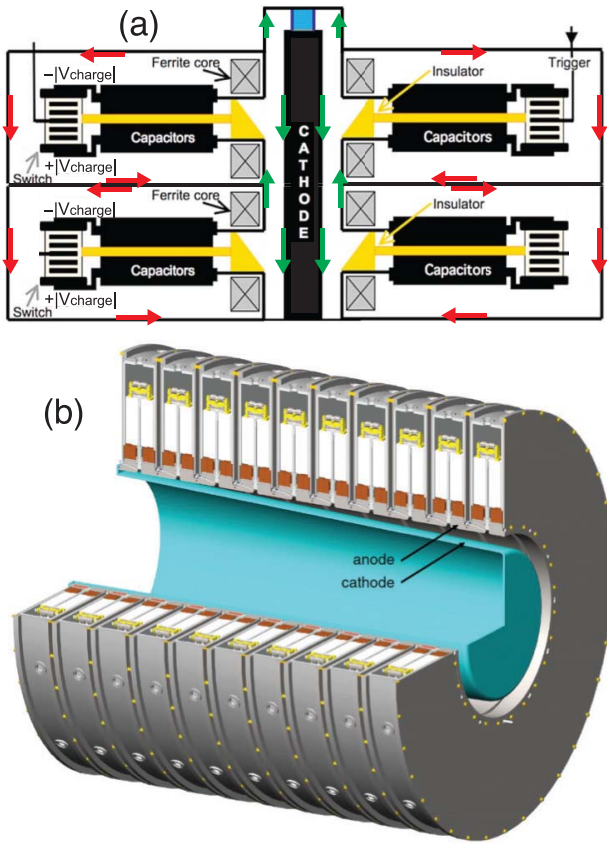
Fig. 19. (a) Illustration of two LTD cavities stacked on top of one another to form a two-cavity LTD *module*. (Source: [32].) This axisymmetric cross-sectional representation illustrates how the desired load current channel (green arrows) flows relative to the undesired, parasitic current channels (red arrows). (b) A 10-cavity LTD *module* design by Sandia National Laboratories. Here one can see the output gaps from each cavity stacked on top of one another, forming the anode path, which surrounds the central cathode stalk. Stacking the output gaps in series like this increases the voltage of the overall driver (think of batteries being stacked on top of one another with the $\pm$ polarities all aligned). Additionally, and again because of the series configuration, the inductances of the cavities add together, while the effective capacitance of the module is reduced. Thus, the characteristic impedance of the module is proportional to the number of cavities in the module. (Source: [36].)

of one another—think of batteries being stacked on top of one another with the $\pm$ polarities all aligned—this is essentially the same operating principle as that of an inductive voltage adder (IVA) [113][3]

$$V_{\text{module}} = N_{\text{cavities}} \cdot V_{\text{cavity}}. \tag{73}$$

The module inductance also increases linearly with the number of cavities used. To understand this, consider the increase in overall cavity volume as more cavities are stacked on top of one another. All of this volume must be filled with magnetic flux, and this volume increases linearly with the number of identical cavities used in the module. Thus, the overall module inductance is

$$L_{\text{module}} = N_{\text{cavities}} \cdot L_{\text{cavity}}. \tag{74}$$

[3]Note that one of the primary differences between an IVA and an LTD is that the prime-power generation for an IVA is generated external to the IVA cavity, often requiring Marx generators and PFLs, whereas an LTD's prime-power is generated *within* the LTD cavity itself.

Conversely, the series arrangement means that the equivalent capacitance of the module is reduced in proportion to the number of identical cavities used

$$C_{\text{module}} = C_{\text{cavity}}/N_{\text{cavities}}. \tag{75}$$

Therefore, the characteristic impedance of the module is proportional to the number of identical cavities used

$$Z_{\text{module}} = \sqrt{\frac{L_{\text{module}}}{C_{\text{module}}}} = N_{\text{cavities}} \cdot \sqrt{\frac{L_{\text{cavity}}}{C_{\text{cavity}}}}$$
$$= N_{\text{cavities}} \cdot Z_{\text{cavity}}. \tag{76}$$

Since both the voltage and the impedance increase together with the number of cavities, the peak current remains unchanged from that of a single LTD cavity

$$I_{\text{module}} = \frac{V_{\text{module}}}{Z_{\text{module}}} = \frac{N_{\text{cavities}} \cdot V_{\text{cavity}}}{N_{\text{cavities}} \cdot Z_{\text{cavity}}} = I_{\text{cavity}}. \tag{77}$$

Interestingly, while the impedance increases with the number of cavities, the rise time to peak current remains unchanged from that of a single LTD cavity

$$\tau_{\text{module}} = \frac{\pi}{2}\sqrt{L_{\text{module}}C_{\text{module}}} = \frac{\pi}{2}\sqrt{L_{\text{cavity}}C_{\text{cavity}}}$$
$$= \tau_{\text{cavity}}. \tag{78}$$

Since the nominal $I_{\text{module}} = I_{\text{cavity}}$ and $\tau_{\text{module}} = \tau_{\text{cavity}}$, and since for HEDP applications we are usually seeking large peak currents with short rise times, one may wonder: what is the advantage of stacking multiple cavities together? The answer has to do with something called machine *"stiffness."* If a high-impedance load is used on a low-impedance (or "soft") driver like a single-cavity LTD, then the resulting current pulse could be significantly distorted from the nominal current obtained when using a well-matched (low impedance) load. That is, for a soft, low-impedance, single-cavity LTD driving a high-impedance (high-inductance) load, we could have $L_{\text{load}} \gg L_{\text{cavity}}$ and $Z_{\text{load}} \gg Z_{\text{cavity}}$, so that

$$L_{\text{system}} = L_{\text{cavity}} + L_{\text{load}} \approx L_{\text{load}} \tag{79}$$
$$Z_{\text{system}} = Z_{\text{cavity}} + Z_{\text{load}} \approx Z_{\text{load}}. \tag{80}$$

Then, with $V_{\text{system}} \approx V_{\text{cavity}}$ and $C_{\text{system}} \approx C_{\text{cavity}}$, we would end up with

$$I_{\text{system}} = \frac{V_{\text{system}}}{Z_{\text{system}}} \approx \frac{V_{\text{cavity}}}{Z_{\text{load}}} \ll I_{\text{cavity}} \tag{81}$$
$$\tau_{\text{system}} \approx \frac{\pi}{2}\sqrt{L_{\text{load}}C_{\text{cavity}}} \gg \tau_{\text{cavity}}. \tag{82}$$

However, if we stack multiple LTD cavities together in series, so that $L_{\text{module}} \gg L_{\text{load}}$ and $Z_{\text{module}} \gg Z_{\text{load}}$, then we could instead have

$$L_{\text{system}} = L_{\text{module}} + L_{\text{load}} \approx L_{\text{module}} \tag{83}$$
$$Z_{\text{system}} = Z_{\text{module}} + Z_{\text{load}} \approx Z_{\text{module}}. \tag{84}$$

Now, with $V_{\text{system}} \approx V_{\text{module}}$ and $C_{\text{system}} \approx C_{\text{module}}$, we would have

$$I_{\text{system}} = \frac{V_{\text{system}}}{Z_{\text{system}}} \approx \frac{V_{\text{module}}}{Z_{\text{module}}} = I_{\text{module}} = I_{\text{cavity}} \tag{85}$$
$$\tau_{\text{system}} \approx \frac{\pi}{2}\sqrt{L_{\text{module}}C_{\text{module}}} = \tau_{\text{module}} = \tau_{\text{cavity}}. \tag{86}$$

Therefore, when driving a high-impedance (high-inductance) load, we can sustain the nominal current pulse of an LTD module, which is equivalent to the nominal current pulse of a single LTD cavity, by increasing the number of cavities stacked together in the module.

By making the current pulse more robust and independent of the load impedance, we are increasing the "*stiffness*" of the generator. The machine stiffness can be particularly important in applications involving Z-pinch implosions, where the impedance (inductance) of the Z-pinch load is often initially very low but then increases rapidly as the Z-pinch plasma tube implodes to small radius. The impedance (inductance) of the load increases rapidly because the current flows at the radius of the imploding plasma tube $r(t)$, and the resulting load inductance is given by (11) and/or (14) with $r_{in} \rightarrow r(t)$. As mentioned in Section III (see Fig. 7), this rapid increase in load impedance results in an "inductive dip" in the current pulse. A stiffer driver will have a smaller inductive dip than a softer driver. A smaller inductive dip is generally considered "good," since more current is usually desired for driving the load harder. However, a stiffer driver comes at the expense of more cavities. Thus, design tradeoffs must be made between pinch performance and machine cost. In some cases, the magnetic pressure at stagnation might not be very important, thus fewer cavities per module could be used. One of the nice things about LTD technology is the flexibility in choosing (designing) a suitable driver impedance for the particular application.[4]

Combining (70), (78), and (86), we find that

$$\tau_{system} \approx \tau_{module} = \tau_{cavity} \sim \tau_{brick}. \tag{87}$$

Thus, the rise time of the overall LTD system is largely determined by the rise time of the individual bricks themselves. This is particularly true for small load impedances (i.e., $Z_{load} \ll Z_{cavity} < Z_{module} \approx Z_{system}$). This is an important point to keep in mind when designing an LTD system. It is difficult to significantly alter the inductance of a single brick (where $L_{brick} \approx L_{switch}$), thus a machine designer's ability to control the rise time of a facility comes primarily from the designer's choice of capacitor size. The selection of smaller capacitors results in shorter rise times. The selection of smaller capacitors also means that a larger number of capacitors (and thus bricks) must be used in parallel to maintain the large overall $C_{cavity} = N_{bricks} C_{brick}$ [or $C = nC_i$ in (9)] needed for producing large amplitude current pulses [see also the discussion surrounding (72)]. Note once again, however, that by using many small capacitors (bricks) in parallel, we are also reducing the overall system inductance, since a single cavity inductance scales as $L_{cavity} \sim L_{brick}/N_{bricks} \approx L_{switch}/N_{bricks}$. This leads to the rise time scaling result shown in (87),

---

[4]Note that if a generator is stiffer than necessary for a particular application, then some of the excess inductively stored magnetic energy can be recovered using an adapter device called a load-current multiplier (LCM) [114]. This device acts as an impedance transformer to better match the driver impedance to the load impedance. For example, an LCM was used to nearly double the current (from 0.9 to 1.7 MA) into planar wire-array loads and planar foil loads on the relatively stiff ZEBRA generator at the University of Nevada, Reno [115]. See [114] for more details on the LCM device.
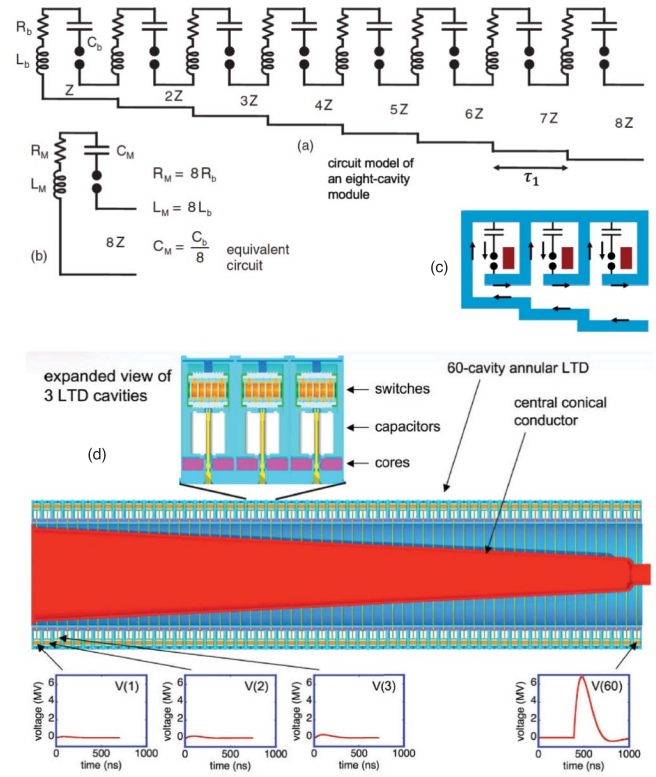

Fig. 20. Illustrations of impedance matching within a module. (a) and (b) Equivalent circuits for an 8-cavity module. (c) Schematic illustrating the current flow in a 3-cavity module. (d) A 60-cavity module with a center conductor (red cathode stalk) that decreases in radius from left to right. This increases the characteristic impedance of the coaxial transmission line in a way that matches the growing cumulative impedance of the module for a forward propagating wave that travels from left to right through the module. The result is a purely forward-going, amplified voltage pulse at the output end of the module: $V_{module} \approx N_{cavities} \cdot V_{cavity}$. (Source: [27] and [116].)

since $\tau_{cavity} = (\pi/2)(L_{cavity} C_{cavity})^{1/2} \sim \tau_{brick}$ [see also the discussion surrounding (69) and (70)].

The electromagnetic wave that propagates through an LTD module has a finite speed of propagation. For this reason, the triggering of the individual cavities should be controlled such that each successive cavity is triggered τ_1 after the preceding cavity, where τ_1 is the one-way transit time of the wave passing by a given cavity. In this way, the voltage is amplified as the electromagnetic wave propagates through the module. Also, in order to achieve very little back reflection, the characteristic impedance of the module should be continuously and smoothly increased to match the increasing impedance of the module (as seen by the wave) as the wave propagates down the module. This is illustrated by the equivalent circuit models and module graphics presented in Fig. 20. Full electromagnetic simulations have shown that indeed a forward-going wave propagates through an impedance-matched module with very little back reflection and very high efficiency ($\eta \approx 70\%$; see Fig. 21) [116], [117]. For detailed explanations on how impedance matching works in these systems, see [113, Sec. B1] and [118, Appendix].

In an alternative arrangement, a post-hole convolute can be used to connect the cavities together within a multicavity
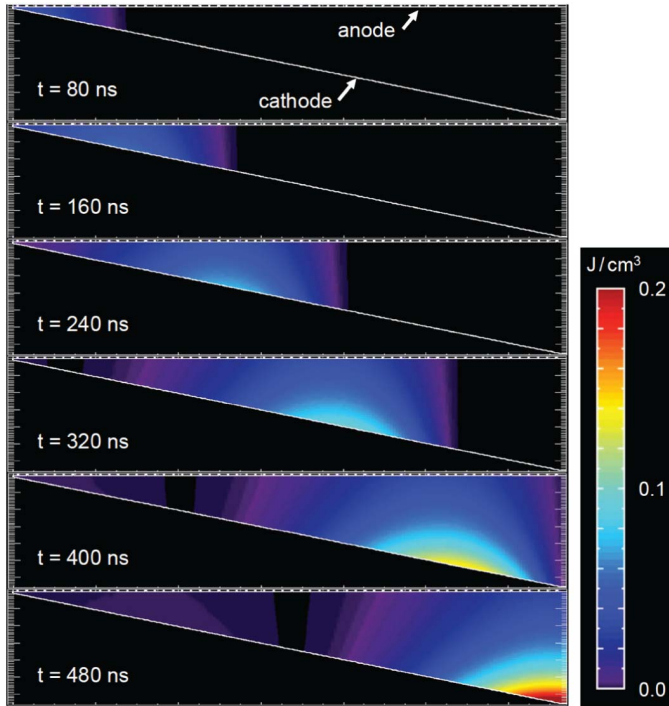
Fig. 21. 2-D LSP simulation results illustrating an electromagnetic pulse propagating down an impedance-matched LTD module with very little back reflections. (Source: [116] and [117].)
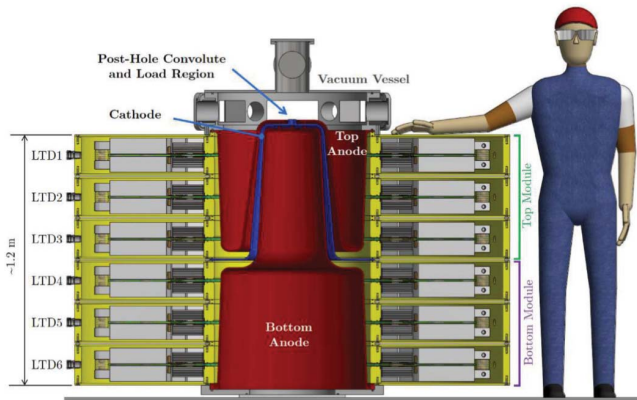

Fig. 22. The HADES LTD design being developed at the University of Rochester. This six-cavity LTD design combines both series voltage addition and parallel current addition to drive 1 MA in 150 ns into a 20-nH inductive load in an ultracompact footprint. The cavities are grouped together into a top module of three cavities and a bottom module of three cavities. The three cavities within each module are connected together in series so that $V_{\text{module}} \approx 3V_{\text{cavity}} \approx 6|V_{\text{charge}}|$. The top and bottom three-cavity modules are then combined in parallel through the use of a post-hole convolute near the load region so that $I_{\text{load}} \approx 2I_{\text{module}}$. (Source: [119].)

LTD module. With a post-hole convolute, the cavities are connected in parallel rather than in series, thus the cavity currents are added together rather than the cavity voltages. A post-hole convolute is implemented in the HADES LTD design at the University of Rochester (see Fig. 22) [119].

Another way to connect LTDs together in parallel, and thus amplify the driver current, is to connect the outputs of multiple LTD modules together in parallel [26]. This is one of the design principles behind the recently proposed Z-300 and Z-800 drivers (see Fig. 23) [36]. Like the present Z machine,

Z300:
- 48 MA, 320 TW delivered
- 48 MJ stored
- 30–80 MJ simulated fusion yield
- 35 m in diameter (size of Z today)
- 2970 LTD cavities

LTD-based architectures
(Linear Transformer Driver)

Z800:
- 60 MA, 890 TW delivered
- 130 MJ stored
- 0.2–1 GJ simulated fusion yield
- 52 m in diameter
- 5400 LTD cavities

Conceptual High Fusion Yield Machines
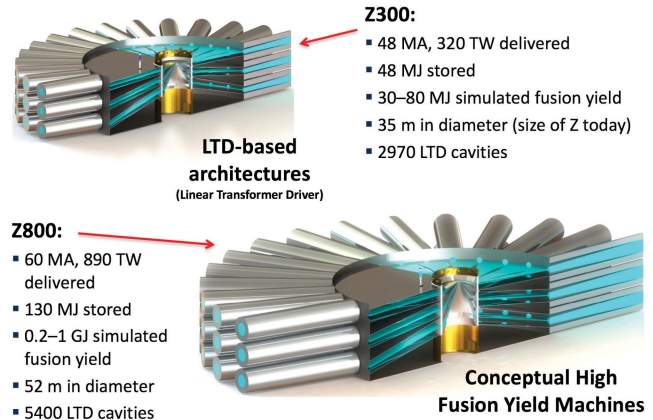
Fig. 23. The conceptual Z-300 and Z-800 super accelerator designs from [36]. Multiple cavities are stacked in series to achieve voltage amplification within modules, and multiple modules are combined in parallel to achieve current amplification within the overall super accelerator. (Source: [36].)

these designs still employ a multilevel MITL vacuum section, where various levels are again connected via a post-hole convolute. In Z-300 and Z-800, there are actually six MITL levels connected via a triple post-hole convolute. Also note that these super accelerator architectures employ thousands of LTD cavities, thus LTD reproducibility and reliability are key to the success of such designs. Fortunately, LTDs can be designed to be reproducible and reliable, which has been demonstrated experimentally, as shown in Fig. 24(a) [32]. Additionally, through various triggering sequences of the individual bricks within a cavity, the individual cavities within a module, or the individual modules within an accelerator, custom pulse shapes can be generated, as shown in Fig. 24(b) [30]. Also, by replacing some number of the main bricks in a cavity with faster bricks, square-wave-like "flat-topped" pulses can be generated from a single LTD cavity, as shown in Fig. 24(c) and (d) [35]. The flat-topped pulses are obtained by setting $\tau_{\text{brick}} = 3 \cdot \tau'_{\text{brick}} = (3\pi/2)(L'_{\text{brick}} C'_{\text{brick}})^{1/2}$, where τ_{brick} is the rise time of the main bricks, and τ'_{brick}, L'_{brick}, and C'_{brick} are the rise time, inductance, and capacitance of the faster bricks, respectively. The faster bricks provide the third harmonic in a Fourier series representation of the desired square wave. Note that the pulse-shaping techniques described in [30] and [35] are in addition to the pulse-shaping technique mentioned previously and described in [105], where bricks are used directly to drive long, transit-time-isolated coaxial cables.

In closing this section, we contrast an LTD-based system with a Marx-based system. We begin by contrasting a single LTD cavity with a single Marx generator. Essentially, the difference is that a single LTD cavity is a low-impedance driver, while a single Marx generator is a high-impedance driver. This is due to the parallel capacitor (and switch) configuration during an LTD discharge versus the series capacitor (and switch) configuration during a Marx discharge. For this discussion, we will consider an LTD "brick" as we have throughout this tutorial (i.e., as two capacitors and a switch). To be consistent with this brick (and bipolar charging) arrangement, we will select the bipolar Marx configuration (Fig. 12) for our comparison. From Fig. 12, we see that
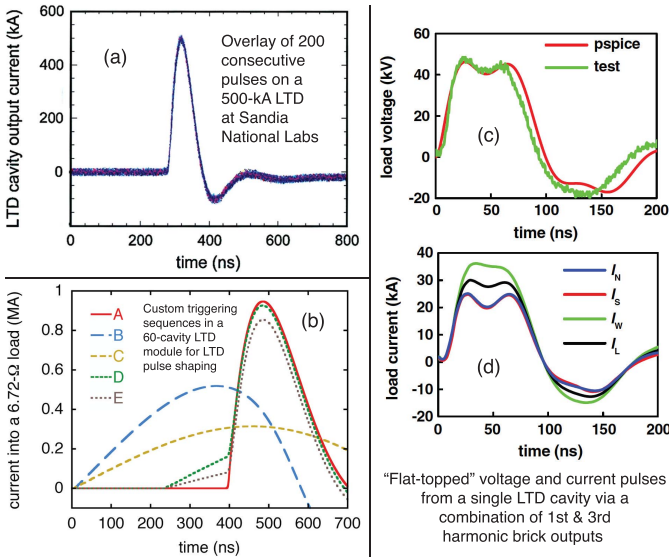
Fig. 24. Some qualities of LTD technology include (a) reproducibility and reliability (Source: [32]) and (b)–(d) versatility in generating custom pulse shapes [Source for (b): [30]. Source for (c) and (d): [35]].

each "stage" consists of two capacitors and a switch. Thus, each individual power unit (or "brick") in an LTD cavity is equivalent to each individual power unit (or "stage") in a Marx generator (as long as the same capacitors and switches are used for both architectures, which we will assume for our discussion here). Now, a single LTD cavity is many individual power units arranged in parallel during a discharge. Thus, a single LTD cavity is a low-impedance driver with $Z_{cavity} = (1/N_{bricks})(L_{brick}/C_{brick})^{1/2} = (1/N_{units})Z_{unit}$. By contrast, a single Marx generator is many individual power units arranged in series during a discharge. Thus, a single Marx generator is a high-impedance (and stiff) driver with $Z_{marx} = N_{stages}(L_{stage}/C_{stage})^{1/2} = N_{units}Z_{unit}$. Note, however, that the driver impedance (and voltage) of an LTD-based system can be increased by stacking many LTD cavities together in series to form an LTD module, while the driver impedance of a Marx-based system can be decreased (and the current increased) by connecting several Marx generator outputs together in parallel (e.g., the 36 Marx generators in parallel on the Z facility). Thus, the driver impedance of an LTD-based system can be made equivalent to the driver impedance of a Marx-based system. For example, if the number of LTD cavities stacked in series ($N_{cavities}$) is set such that $N_{cavities} = N_{bricks}$, where N_{bricks} is the number of bricks per cavity, and if the number of Marx generators used in parallel ($N_{marx,\parallel}$) is set such that $N_{marx,\parallel} = N_{stages}$, where N_{stages} is the number of stages per Marx generator, then we will have $Z_{module} = Z_{marx,\parallel} = Z_{brick} = Z_{stage} = Z_{unit}$.

Note that, regardless of the configuration used (e.g., series versus parallel and/or Marx versus LTD), the rise time of the overall facility is largely set by the rise time of the individual power units for the same reasons that we discussed previously (i.e., $\tau_{peak} = (\pi/2)\sqrt{LC} = (\pi/2)(L_{unit}C_{unit})^{1/2} = \tau_{unit}$). Thus, as in our discussions surrounding (69), (70), (72), and (87), a machine designer's ability to control the rise time of a given facility (either an LTD-based facility or a Marx-based facility) comes primarily from the designer's choice of

capacitor size. The selection of smaller capacitors results in shorter rise times (and vice versa). Furthermore, the selection of parallel (series) configurations sets the driver impedance and voltage to lower (higher) values and the current to higher (lower) values. The total energy stored is set by the charge voltage and the total number of capacitors used in the facility.

Comparing Figs. 11 and 20, we see that, from an equivalent circuit standpoint, an LTD module could appear as being very similar to a Marx generator. Traditionally, though, the Marx generators used for HEDP applications are comprised of capacitors with very large individual capacitance values (e.g., compare the 2.6-μF capacitors used in the Marx generators on the Z facility with the 40-nF capacitors used in the MAIZE LTD cavity). The result is that traditional Marx generators have longer rise times than modern (fast) LTDs, and thus traditional Marx-driven systems usually require pulse compression (PFLs). Additionally, the LTD's prime power is generated from within the LTD cavity itself, and because modern LTDs use small capacitors and small switches, many such capacitors and switches can be packaged very efficiently within the LTD cavity itself. The result is that a modern LTD module can be more compact and efficient than traditional Marx-driven systems. For example, the cavity architecture of a traditional IVA [113] is very similar to the cavity architecture of an LTD (both systems use ferromagnetic cores, for example). However, an LTD module is generally more compact and efficient than an IVA, because IVA cavities are driven by Marx generators that are external to the cavity, thus requiring large external oil tanks for the Marx generators and large external water lines (PFLs) for pulse compression [18]. As another example of the compactness and efficiency of an LTD-based system, consider the use of LTD modules in super accelerators like the conceptual Z-300 and Z-800 designs (see Fig. 23). These designs have no need for pulse compression, since the current pulse rise time is ~100 ns right from the LTD bricks. By contrast, the current pulse rise time from the Marx generators on today's Z facility is ~1 μs. By comparing Figs. 23 and 9, we see that the complexity associated with pulse compression on today's Z facility could be replaced by a more efficient LTD-based module, with impedance matching employed throughout the system. Notably, the diameter of the Z-300 design is approximately equal to the diameter of today's Z facility, but Z-300 would be expected to deliver nearly 50 MA of current to a MagLIF load (which is roughly twice that of today's Z facility). Further note, however, that one of the big challenges in building and operating a large LTD-based system such as Z-300 or Z-800 is that these super accelerators will require thousands of LTD cavities working together (see Fig. 23), where each cavity houses ~20 bricks (i.e., 20 switches and 40 capacitors).

Recently, the development of an LTD spinoff technology, called an impedance-matched Marx generator (IMG), has further blurred the lines between an LTD module and a Marx generator [118] (see Fig. 25). Like an LTD module, the IMG's prime power is generated within its own cavity. Additionally, because small capacitors are used in both IMGs and LTDs, the IMG is a fast generator like the modern LTD. Unlike an LTD module, however, the IMG is not comprised
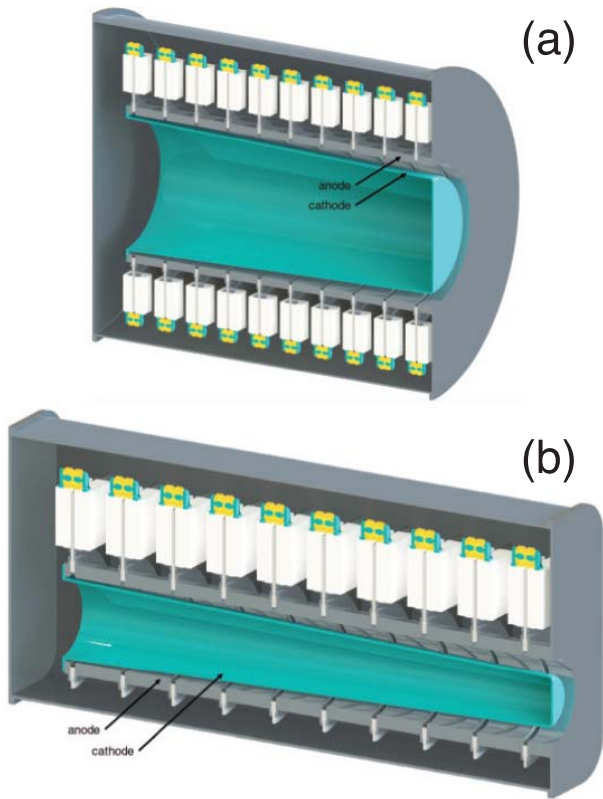
Fig. 25. An LTD spinoff technology called an Impedance-matched Marx Generator (IMG) [118]. (a) Full coaxial 10-stage IMG [118]. (b) 10-stage, single-brick-per-stage IMG [118]. IMGs save cost and weight by removing the parasitic current path at each stage and therefore removing the need for heavy, expensive ferromagnetic cores (compare with Figs. 18 and 19). (Source: [118].)

of individual cavities stacked together. This eliminates the parasitic current path around the casing of each individual cavity. By eliminating the parasitic current paths at each stage, the IMG has no need for ferromagnetic cores, saving cost and weight. A particularly compact implementation of the IMG that could be very useful for high-impedance applications, such as high-power microwave sources [120] and flash X-ray radiography sources [17], is the single-brick-per-stage design shown in Fig. 25(b) [118].

VI. LTD-DRIVEN HEDP RESEARCH FROM AROUND THE WORLD

The LTD concept was pioneered in 1995–1997 at the High Current Electronics Institute (HCEI), in Tomsk, Russia, by Boris M. Kovalchuk *et al.* [23]. LTDs have since been called "the greatest advance in prime-power generation since the invention of the Marx generator in 1924" [116]. The original concept [23] used bricks with only one capacitor and only two bricks per cavity. The use of only two bricks in parallel ($N_{\text{bricks}} = 2$) meant that very large capacitors ($C_{\text{cap}} = C_{\text{brick}} = 4 \ \mu\text{F}$) had to be used to obtain the large overall LTD capacitance ($C = N_{\text{bricks}}C_{\text{bricks}}$) required for a large overall peak current (I_{peak}). Additionally, these large bricks had a relatively large inductance (L_{brick}). Taken together, the large $L \sim L_{\text{brick}}/N_{\text{bricks}}$ and the large $C = N_{\text{bricks}}C_{\text{bricks}}$ resulted in a current pulse with a relatively long rise time: $\tau_{\text{peak}} =$

$(\pi/2)\sqrt{LC} \sim (\pi/2)(L_{\text{brick}}C_{\text{brick}})^{1/2} \sim 1 \ \mu\text{s}$. An example of this longer rise time LTD technology is the 5-MA, 700-ns Sphinx machine at the Center d'Etudes de Gramat in Gramat, France [121] (note that this machine is presently being decommissioned after many years of productive Z-pinch research [122]). Subsequently, the use of many bricks per cavity (large N_{bricks}), where each brick has a small inductance (L_{brick}) and a small capacitance ($C_{\text{brick}} = C_{\text{cap}}/2 = 20$ nF), was proposed for the development of fast rise time LTDs ($\tau_{\text{peak}} \sim 100$ ns) [24]–[26] (see the 40 bricks in the MAIZE LTD in Fig. 16, for example). Perhaps the first submicrosecond LTD tested by HCEI is the IMRI-5 facility [24]. This facility remains in use to this day and has accumulated nearly two decades worth of research on gas-puff Z-pinches for X-ray production [123]–[125]. This long track record provides a good example of the robustness of an LTD facility. HCEI continues to develop LTD technology, including the development of air-insulated (rather than oil insulated) LTD cavities [38]. Air-insulated LTDs are not as powerful or compact as oil insulated LTDs, but they are much easier to service and maintain.

In the mid-2000's, a collaboration was developed between HCEI, Sandia National Laboratories, and the University of Michigan (UM) to bring LTD technology to the United States. In 2006–2007, a module of five 1-MA, 100-ns LTD cavities was tested at HCEI with resistive and electron-beam diode loads [28]. In July 2007, one of these HCEI cavities was shipped to UM, becoming the MAIZE facility and the first 1-MA, 100-ns LTD in the United States [29]. In 2008, 10 more 1-MA, 100-ns LTD cavities were shipped to Sandia, becoming part of the Mykonos facility [32] (see Fig. 26). Sandia continues to develop LTD technology to this day, including the development of low-loss ferromagnetic cores, low-inductance spark-gap switches [126], [127], multi-cavity LTD modules [32], [36] (see Mykonos facility in Fig. 26), and LTD spinoff technologies such as LTD brick-driven cable pulsers [105] and IMGs [118].

As mentioned above, the 3-m-diameter MAIZE facility delivers nominal electromagnetic pulses of order 1 MA, 100 ns, 100 kV, 10 kJ, and 0.1 TW (see Fig. 16). Note that since MAIZE is a single low-impedance LTD cavity ($Z_{\text{maize}} = 0.16 \ \Omega$; see Section V), the current pulse waveform is often significantly affected by the load impedance. This should be contrasted with other MA-class university drivers, such as MAGPIE [100], [101], ZEBRA [102], [103], and COBRA [104], which are stiffer generators and thus less affected by load impedance [see discussions regarding (65) and Fig. 15].

The HEDP research program on MAIZE presently includes: 1) the study of implosion instabilities in thin-walled liners (cylindrical foils) [128]–[130], which are relevant to MagLIF; 2) the development of diagnostic instruments and techniques that can be transferred to Z and NIF; 3) a collaboration with the University of Nevada, Reno to study wire-array Z-pinches for X-ray source development [109], [110]; 4) the study of power flow within LTDs and the coupling of LTDs to high-energy-density (HED) matter in general; 5) the study of magnetized plasma flows for laboratory astrophysics; and 6) an effort to create and study
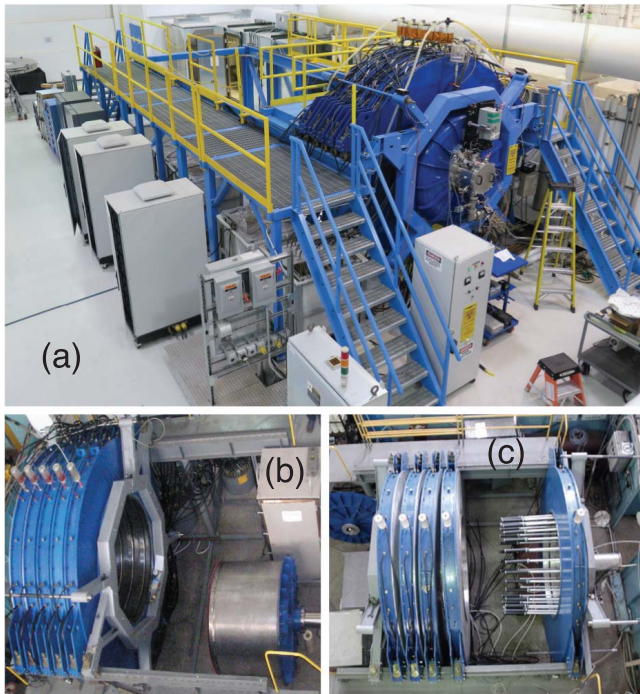
Fig. 26. Photographs of the multicavity, 1-MA Mykonos LTD facility at Sandia National Laboratories. (a) An assembled five-cavity LTD module. (b) and (c) Five cavities being assembled/disassembled into a five-cavity LTD module. (Source: [32].)
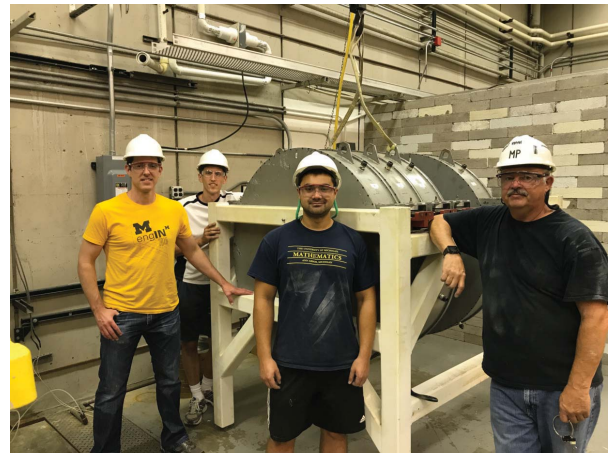

Fig. 27. The early days of the BLUE pulsed-power facility at UM. These four LTD cavities were previously part of the 21-cavity Ursa Minor facility at Sandia National Laboratories [18], [34], [131], [132]. They arrived at Michigan on August 21, 2017. This technology transfer is part of Sandia's Stevenson-Wydler Gift Program. (Pictured from left to right: Ryan McBride, Nick Jordan, Steven Exelby, and Mark Perreault.)
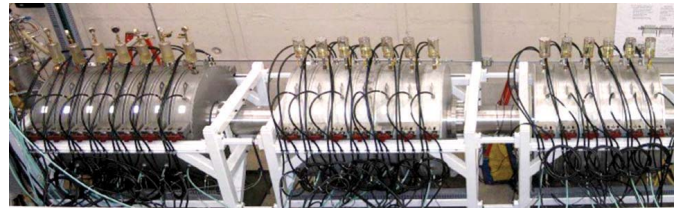

Fig. 28. Photograph of 20 stacked cavities of the 21-cavity Ursa Minor facility at Sandia National Laboratories. Four of these cavities are now being assembled into a variable cavity LTD module (1, 2, 3, or 4 cavities) called BLUE at UM. (Source: [18].)

Fig. 29. Photograph of the 500-kA, 500-ns LTD at the Weizmann Institute of Science in Israel.

pulsed fusion neutron sources (e.g., deuterium gas-puff Z-pinches and/or dense plasma focuses) as well as pulsed X-ray sources (e.g., gas-puff Z-pinches with noble gases).

In addition to MAIZE (Fig. 16), UM is presently building a second LTD facility. This second facility, called BLUE (Bestowed LTD from the Ursa-minor Experiment), will consist of four 1.25-m-diameter cavities (see Fig. 27). Like MAIZE, these four cavities were originally fabricated in Russia, at HCEI. Most recently, these four cavities were part of the 21-cavity Ursa Minor facility at Sandia National Laboratories (see Fig. 28) [18], [34], [131], [132]. Ursa Minor consisted of both HCEI cavities and Sandia-built cavities. The facility is now being repurposed to serve new missions.

The four cavities on BLUE will be assembled such that experiments can be driven with 1, 2, 3, or 4 cavities stacked together. This will enable researchers to *directly* investigate the effects of driver impedance (machine stiffness) on pinch performance. A multicavity module also enables cavity coupling issues to be investigated. Having multicavity LTD modules located at universities is important for student training and fundamental research, especially since future accelerators like Z-300 and Z-800 will require thousands of LTD cavities working together [36] (see Fig. 23).

Another LTD that has been operating for some time now is the 500-kA, 500-ns LTD at the Weizmann Institute of Science in Israel. This LTD is used primarily for gas-puff Z-pinch experiments and spectroscopy development (see Fig. 29 as well as [133] and [134]).

The University of California, San Diego (UCSD) has a 250-kA, 150-ns LTD called GenASIS [135] (see Fig. 30).

This LTD is used for liner/foil experiments [136] and for X-pinch experiments [137]. In addition to GenASIS, UCSD is assembling a second LTD facility, called LTD-III (see Fig. 31). LTD-III consists of a 20-brick cavity that produces ∼1 MA with a rise time of 200 ns into a low-inductance load. The cavity was extensively tested at Sandia National
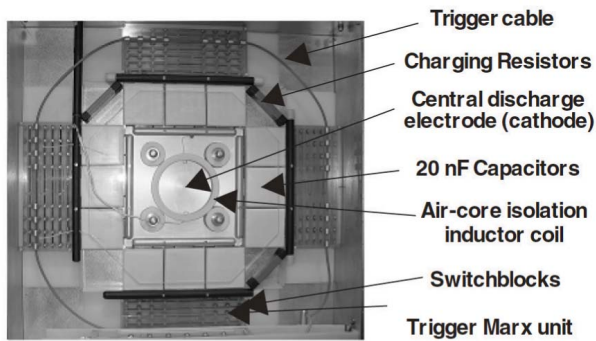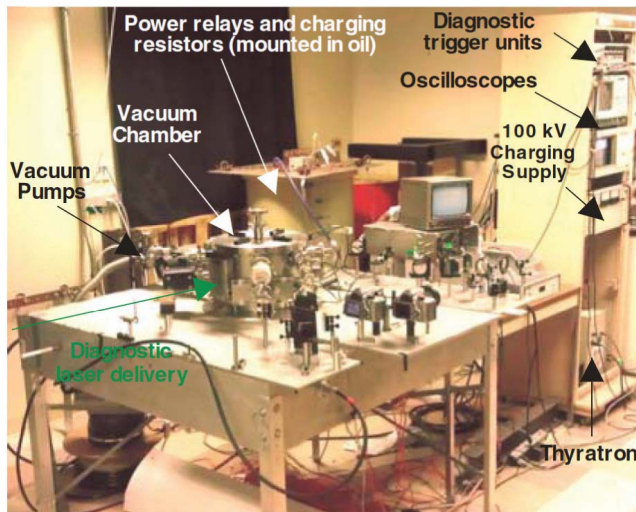
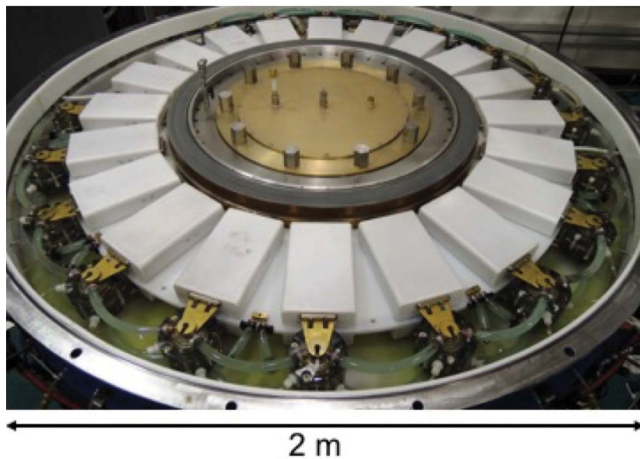Fig. 30.   Photograph of the 250-kA, 150-ns GenASIS LTD at UCSD. (Source: [135].)

Fig. 31.   Photograph of the ∼1-MA, 200-ns LTD-III generator [138], which is now being assembled at UCSD.

Laboratories [138] and is now being assembled at UCSD to perform metallic liner and gas-puff Z-pinch experiments.

A recent collaboration between the University of New Mexico (UNM) and the Naval Research Laboratory (NRL) has led to the development of the 200-kA, 60-ns, air-insulated Lobo LTD at UNM (see Fig. 32). This dry-brick/dry-LTD was originally developed for NRL by Dr. R. Spielman and others at Raytheon Ktech in Albuquerque, NM. Initial characterizations

Fig. 32.   Photograph of the 200-kA, 60-ns Lobo LTD at UNM in Albuquerque.
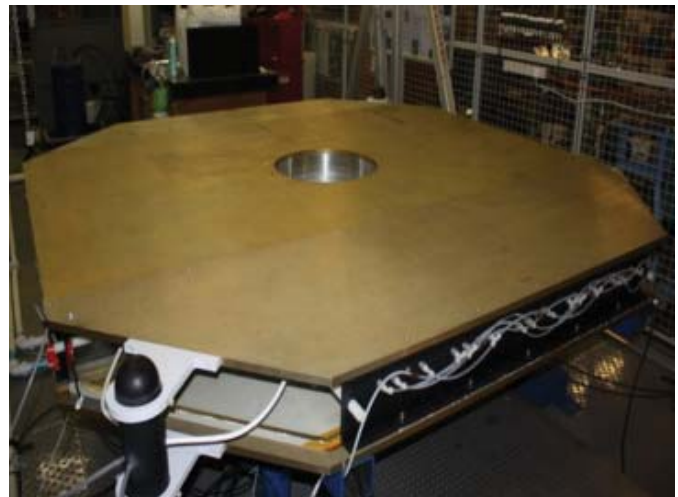
Fig. 33.   Photograph of the 2-MA, 500-ns Mach LTD at Imperial College London, U.K.

have been completed with multiple loads ($<1\ \Omega$, $3\ \Omega$, $10\ \Omega$). The HEDP research program on Lobo includes: 1) X-pinch studies for radiography; 2) dense plasma focus and gas-puff Z-pinch development; and 3) time and space resolved spectroscopy, interferometry, and X-ray imaging.

The somewhat larger 2-MA, 500-ns Mach LTD is presently being used at Imperial College London, U.K. (see Fig. 33). This LTD is air and plastic insulated, and thus it requires no oil or noxious gases. Its load region accepts multiple attachment heads so that experiments can be conducted in air, gas, liquid, or vacuum. Mach is presently being used to study both isentropic and shock compression of materials. Additionally, dense plasma focus development is underway.

As an example of an LTD spinoff technology, a novel two-brick X-pinch radiography driver has been developed at Idaho State University (see Fig. 34) [107]. An X-pinch is formed when two or more fine wires are crossed in the shape of an "X" and an intense current pulse is driven through the wires [139], [140]. At the location where the wires cross (at the "X" point), the current density and magnetic
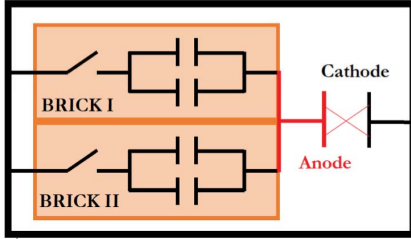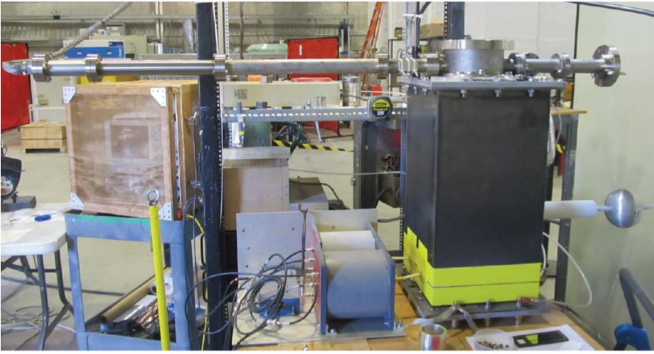
Fig. 34. Photograph and schematic of the two-brick X-pinch pulser at Idaho State University.

pressure are very large. This drives an implosion from a region that is small in both axial and radial extent. As the implosion stagnates and/or "pinches," an intense ~1-ns burst of X-rays is emitted. This enables point-projection radiography. The two-brick X-pinch pulser idea is potentially very useful because of its smallness and portability. For example, this two-brick pulser can be positioned to radiograph other HEDP experiments.

In Fig. 22, the 1-MA, 150-ns HADES LTD design from the University of Rochester is presented [119]. The HADES facility is presently under construction. The HADES design consists of a small, modular, and portable multicavity LTD *module*, which incorporates both series and parallel electrical connections to achieve 1 MA in 150 ns into a 20-nH inductive load, all in a very small footprint. Because of its series connections, HADES will approach the stiffness of the COBRA facility at Cornell (to within about 50%), where COBRA uses a Marx generator/PFL architecture to drive 1 MA in 100 ns into a 25-nH inductive load [104]. This is important to point out because there is a general misconception that LTDs are always "soft" drivers relative to Marx generator/PFL designs; however, we again emphasize that the "stiffness" of an LTD is largely determined by the number of cavities stacked together in series.

The research program on HADES will involve the study of matter at extremes (e.g., both HED matter as well as "*warm dense matter*"). Because of its compact footprint, HADES could be more easily installed at modern particle-accelerator-based light sources such as the Linac Coherent Light Source (LCLS) at the SLAC National Accelerator Laboratory. By locating HADES at LCLS, precise X-ray probes could be used to interrogate the states of matter created by HADES.

VII. Conclusion

It is an exciting time to be involved with pulsed-power-driven HEDP research. The field is growing, with new LTD-based facilities appearing all over the world. Both LTD-based facilities and Marx-generator/PFL-based facilities are enabling experiments in Z-pinch physics, nuclear fusion, material properties, radiation science, laboratory astrophysics, and more. Additionally, there is a strong possibility that the next super accelerator in the United States (i.e., Z-next) will be based on an LTD architecture (e.g., the Z-300 and Z-800 designs). Hopefully, the tools provided in this tutorial will help researchers parse the literature and begin calculating and evaluating their own new pulsed-power designs for HEDP applications.

Appendix A
More Formal Derivation of (3)

From Maxwell's equations, we begin with Ampère's law without the displacement current term

$$\nabla \times \mathbf{B} = \mu_0 \mathbf{J}. \tag{88}$$

Dotting both sides with a differential area element $d\mathbf{A}$ and integrating both sides over the total area A, we have

$$\int_A (\nabla \times \mathbf{B}) \cdot d\mathbf{A} = \int_A \mu_0 \mathbf{J} \cdot d\mathbf{A}. \tag{89}$$

Now, invoking the cylindrical symmetry illustrated in Figs. 1 and 2, we can set the arbitrary area A to be the area enclosed by a circle with radius r in the vacuum region surrounding the central metal stalk in Figs. 1 and 2. This way, all of the current $I = J_{sz} \cdot 2\pi r$ flows through the surface area A in a direction that is normal to A, and thus the RHS of (89) becomes

$$\int_A \mu_0 \mathbf{J} \cdot d\mathbf{A} = \mu_0 I_{\text{enclosed}}(r) = \mu_0 I. \tag{90}$$

For the LHS of (89), we invoke Stokes' theorem and cylindrical symmetry to get

$$\int_A (\nabla \times \mathbf{B}) \cdot d\mathbf{A} = \oint_C \mathbf{B} \cdot d\mathbf{l} = B_\theta \oint_C dl = B_\theta \cdot 2\pi r \tag{91}$$

where C is the path along the circle enclosing area A. Equating (90) and (91) and solving for B_θ gives the magnetic field throughout the vacuum regions illustrated in Figs. 1 and 2

$$B_\theta(r) = \frac{\mu_0 I_{\text{enclosed}}(r)}{2\pi r} = \frac{\mu_0 I}{2\pi r}. \tag{92}$$

As mentioned in Section II of this tutorial, the requirements for this result to be valid are that the system be cylindrically symmetric and that the current I be the total current enclosed by a circle of radius r. This result does **not** require an infinitely thin, infinitely long, current carrying wire. Pulsed-power drivers for HEDP applications are usually very cylindrically symmetric systems, so these relationships are important to remember.

Appendix B
Two Alternative Methods for Deriving (7)

A. Method 1

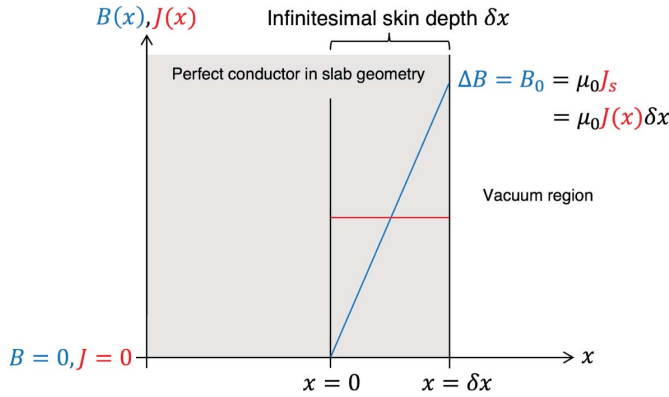Here we consider the ideal interface shown in Fig. 35 between a perfectly conducting metal to the left of the interface

Fig. 35. A perfectly conducting metal slab in planar geometry with a current density $J(x)$ running uniformly within an infinitesimal skin depth δx. The current density vector $\mathbf{J}(x)$ and the magnetic field vector $\mathbf{B}(x)$ are tangential to the interface surface and perpendicular to one another; i.e., $\mathbf{J}(x) \perp \mathbf{B}(x)$.

and a perfect vacuum to the right of the interface. A uniform current density J (in A/m^2) flows within an infinitesimal skin depth δx of the metal's surface. The surface current density is then $J_s = J \cdot \delta x$ (in A/m). Since we have assumed that the magnetic field was initially zero, the magnetic boundary condition for a perfect conductor [cf. Fig. 2 as well as (4) and (5)] states that

$$\Delta B = B_0 = \mu_0 J_s \tag{93}$$

where B_0 is the value of the magnetic field at the vacuum–metal interface. To first order, the magnetic field goes *linearly* from zero (within the metal's bulk) to B_0 (at the vacuum–metal interface) within the infinitesimal skin depth δx; thus, we can write

$$B(x) = B_0 \cdot \frac{x}{\delta x} \quad \text{(for } 0 \leq x \leq \delta x\text{)}. \tag{94}$$

To find the total magnetic force (i.e., the total Lorentz force) acting on the interface, we must integrate the $\mathbf{J} \times \mathbf{B}$ force density over the entire volume of the interface

$$F = \int_0^W \int_0^L \int_0^{\delta x} J \cdot B(x) \, dx \, dy \, dz \tag{95}$$

$$= WL \cdot J \cdot B_0 \cdot \frac{1}{\delta x} \int_0^{\delta x} x \, dx \tag{96}$$

$$= A \cdot J \cdot B_0 \cdot \frac{x^2}{2 \cdot \delta x} \Big|_0^{\delta x} \tag{97}$$

$$= A \cdot \frac{1}{2} \cdot J \delta x \cdot B_0 \tag{98}$$

$$= A \cdot \frac{1}{2} \cdot J_s B_0 \tag{99}$$

where $A = WL$ is the total surface area of the interface. This result states that the total magnetic force acting on the interface (i.e., the $\mathbf{J} \times \mathbf{B}$ force density integrated over the entire volume of the interface) is exactly 1/2 of the product $J_s B_0 A$—we emphasize this point because the factor of 1/2 can be surprising (i.e., the force is not simply $J_s B_0 A$, as one might expect). The next step is to divide the total magnetic force F by the total surface area A to get the magnetic force per unit area, which

is the magnetic pressure

$$p_{\text{mag}} = \frac{F}{A} = \frac{1}{2} J_s B_0. \tag{100}$$

Using the boundary condition in (93), we finally get

$$p_{\text{mag}} = \frac{B_0^2}{2\mu_0}. \tag{101}$$

B. Method 2

Here we begin with the boundary condition in (93) to write

$$\Delta B = \mu_0 J_s = \mu_0 (J \delta x). \tag{102}$$

Letting $(\Delta B / \delta x) \rightarrow (\partial B / \partial x)$, we have

$$\frac{\partial B}{\partial x} = \mu_0 J \tag{103}$$

$$B \frac{\partial B}{\partial x} = \mu_0 J B \tag{104}$$

$$\frac{\partial}{\partial x} \left(\frac{B^2}{2\mu_0} \right) = J B \tag{105}$$

$$\nabla p_{\text{mag}} = |\mathbf{J} \times \mathbf{B}| \tag{106}$$

where

$$p_{\text{mag}} = \frac{B^2}{2\mu_0}. \tag{107}$$

APPENDIX C
TRANSMISSION LINE THEORY FOR UNDERSTANDING PULSE FORMING LINES

From (11) and (59), we can write the distributed inductance and capacitance per unit length for a coaxial transmission line as

$$\hat{L} = \frac{L}{h} = \frac{\mu_0}{2\pi} \ln \left(\frac{r_{\text{out}}}{r_{\text{in}}} \right) \tag{108}$$

$$\hat{C} = \frac{C}{\ell} = \frac{\epsilon_0 \cdot 2\pi}{\ln \left(\frac{r_{\text{out}}}{r_{\text{in}}} \right)}. \tag{109}$$

From standard transmission line theory [62], the propagation velocity of a transverse electromagnetic (TEM) wave through a transmission line is

$$v_{\text{prop}} = \frac{1}{\sqrt{\hat{L}\hat{C}}} = \frac{1}{\sqrt{\mu\epsilon}} = \frac{c}{\sqrt{\mu_r \epsilon_r}}. \tag{110}$$

This is simply the speed of light through a medium with a magnetic permeability $\mu = \mu_0 \mu_r$ and a dielectric permittivity $\epsilon = \epsilon_0 \epsilon_r$, where μ_r is the relative magnetic permeability (relative to vacuum), ϵ_r is the relative permittivity (relative to vacuum), and $c = 3 \times 10^8$ m/s is the speed of light in vacuum. For some of the most commonly used insulating materials (e.g., water), $\mu \approx \mu_0$ (i.e., $\mu_r \approx 1$). This means that the one-way transit time of a transmission line is given by

$$t_1 = \frac{\ell}{v_{\text{prop}}} = \ell \sqrt{\mu\epsilon} \approx \frac{\ell \sqrt{\epsilon_r}}{c} \tag{111}$$

where ℓ is the physical length of the transmission line. Thus, for a desired PFL output pulse length $\tau_d = 2t_1$ (cf. Fig. 13),

we can use a shorter line length ℓ if we use a larger ϵ_r. For water at room temperature, we have $\epsilon_r \approx 80$.

From standard transmission line theory [62], the characteristic impedance of a transmission line is $Z_0 = \sqrt{L/C}$. Thus, for a coaxial PFL, we have

$$Z_{\text{pfl}} = Z_0 = \sqrt{\frac{L}{C}} = \frac{1}{2\pi}\sqrt{\frac{\mu}{\epsilon}} \cdot \ln\left(\frac{r_{\text{out}}}{r_{\text{in}}}\right) \qquad (112)$$

where L and C are again given by (11) and (59), and r_{out} and r_{in} are the outer and inner radii of the coaxial PFL electrodes, respectively. Thus, we can obtain a lower impedance PFL if we use a material with a larger ϵ_r (e.g., water). We can also control the impedance by varying the ratio $r_{\text{out}}/r_{\text{in}}$.

R. D. McBride, P. C. Campbell, S. M. Miller, J. M. Woolstrum, N. B. Ramey, A. P. Shah, B. J. Sporer, N. M. Jordan, Y. Y. Lau, and R. M. Gilgenbach are with the Department of Nuclear Engineering and Radiological Sciences, University of Michigan, Ann Arbor, MI 48109 USA (e-mail: mcbrider@umich.edu).

W. A. Stygar, M. E. Cuneo, D. B. Sinars, M. G. Mazarakis, J. J. Leckbee, M. E. Savage, B. T. Hutsel, J. D. Douglass, M. L. Kiefer, B. V. Oliver, G. R. Laity, M. R. Gomez, D. A. Yager-Elorriaga, and S. G. Patel are with Sandia National Laboratories, Albuquerque, NM 87185 USA.

B. M. Kovalchuk and A. A. Kim are with the Institute of High Current Electronics, Russian Academy of Sciences, Tomsk 634055, Russia

P.-A. Gourdain is with the Extreme State Physics Laboratory, Department of Physics and Astronomy, University of Rochester, NY 14627 USA.

S. N. Bland is with the Blackett Laboratory, Department of Physics, Imperial College London, London SW7 2BW, U.K.

S. Portillo is with the Department of Electrical and Computer Engineering, University of New Mexico, Albuquerque, NM 87131 USA.

S. C. Bott-Suzuki and F. N. Beg are with the Center for Energy Research, University of California, San Diego, CA 92093 USA.

Y. Maron is with the Faculty of Physics, Weizmann Institute of Science, Rehovot 76100, Israel.

R. B. Spielman is with the Department of Physics, Idaho State University, Pocatello, ID 83209 USA.

D. V. Rose and D. R. Welch are with Voss Scientific Inc., Albuquerque, NM 87108 USA.

J. C. Zier and J. W. Schumer are with the U.S. Naval Research Laboratory, Washington, DC 20375 USA.

J. B. Greenly is with the Laboratory of Plasma Studies, Cornell University, Ithaca, NY 14853 USA.

A. M. Covington is with the Nevada Terawatt Facility, Department of Physics, University of Nevada, Reno, NV 89557 USA.

A. M. Steiner is with Lockheed Martin Aeronautics Company, Palmdale, CA 93599 USA.

References

[1] M. E. Savage *et al.*, "Status of the Z pulsed power driver," in *Proc. 18th Int. Pulsed Power Conf.*, Chicago, IL, USA, Jun. 2011, pp. 983–990.

[2] D. V. Rose *et al.*, "Three-dimensional electromagnetic model of the pulsed-power Z-pinch accelerator," *Phys. Rev. ST Accel. Beams*, vol. 13, no. 1, p. 010402, 2010.

[3] T. R. Boehly *et al.*, "Initial performance results of the OMEGA laser system," *Opt. Commun.*, vol. 133, nos. 1–6, pp. 495–506, Jan. 1997, doi: 10.1016/S0030-4018(96)00325-2.

[4] L. J. Waxer *et al.*, "High-energy petawatt capability for the omega laser," *Opt. Photon. News*, vol. 16, no. 7, pp. 30–36, Jul. 2005, doi: 10.1364/OPN.16.7.000030.

[5] C. A. Haynam *et al.*, "National ignition facility laser performance status," *Appl. Opt.*, vol. 46, no. 16, pp. 3276–3303, Jun. 2007. [Online]. Available: http://ao.osa.org/abstract.cfm?URI=ao-46-16-3276

[6] O. A. Hurricane *et al.*, "Fuel gain exceeding unity in an inertially confined fusion implosion," *Nature*, vol. 506, no. 7488, pp. 343–348, 02 2014, doi: 10.1038/nature13008.

[7] S. A. Slutz *et al.*, "Pulsed-power-driven cylindrical liner implosions of laser preheated fuel magnetized with an axial field," *Phys. Plasmas*, vol. 17, no. 5, p. 056303, 2010.

[8] S. A. Slutz and R. A. Vesey, "High-gain magnetized inertial fusion," *Phys. Rev. Lett.*, vol. 108, p. 025003, Jan. 2012. [Online]. Available: http://link.aps.org/doi/10.1103/PhysRevLett.108.025003

[9] M. E. Cuneo *et al.*, "Magnetically driven implosions for inertial confinement fusion at Sandia National Laboratories," *IEEE Trans. Plasma Sci.*, vol. 40, no. 12, pp. 3222–3245, Dec. 2012.

[10] M. R. Gomez *et al.*, "Experimental demonstration of fusion-relevant conditions in magnetized liner inertial fusion," *Phys. Rev. Lett.*, vol. 113, p. 155003, Oct. 2014, doi: 10.1103/PhysRevLett.113.155003.

[11] M. R. Martin *et al.*, "Solid liner implosions on Z for producing multi-megabar, shockless compressions," *Phys. Plasmas*, vol. 19, no. 5, p. 056310, 2012, doi: 10.1063/1.3694519.

[12] R. W. Lemke *et al.*, "Probing off-Hugoniot states in Ta, Cu, and Al to 1000 GPa compression with magnetically driven liner implosions," *J. Appl. Phys.*, vol. 119, no. 1, p. 015904, 2016. [Online]. Available: http://scitation.aip.org/content/aip/journal/jap/119/1/10.1063/1.4939675

[13] J. E. Bailey *et al.*, "Radiation science using Z-pinch x rays," *Phys. Plasmas*, vol. 9, p. 2186, Jan. 2002.

[14] G. A. Rochau *et al.*, "Radiating shock measurements in the Z-pinch dynamic Hohlraum," *Phys. Rev. Lett.*, vol. 100, no. 12, p. 125004, 2008.

[15] B. Jones *et al.*, "Implosion dynamics and K-shell X-ray generation in large diameter stainless steel wire array Z pinches with various nesting configurations," *Phys. Plasmas*, vol. 15, no. 12, p. 122703, 2008.

[16] B. Jones *et al.*, "The effect of gradients at stagnation on K-shell X-ray line emission in high-current Ar gas-puff implosions," *Phys. Plasmas*, vol. 22, no. 2, p. 020706, 2015

[17] J. Maenchen, G. Cooperstein, J. O'Malley, and I. Smith, "Advances in pulsed power-driven radiography systems," *Proc. IEEE*, vol. 92, no. 7, pp. 1021–1042, Jul. 2004.

[18] J. Leckbee *et al.*, "Linear Transformer Driver (LTD) research for radiographic applications," in *Proc. IEEE Pulsed Power Conf.*, Jun. 2011, pp. 614–618.

[19] M. D. Knudson *et al.*, "Direct observation of an abrupt insulator-to-metal transition in dense liquid deuterium," *Science*, vol. 348, no. 6242, pp. 1455–1460, 2015, doi: 10.1126/science.aaa7471.

[20] J. E. Bailey *et al.*, "A higher-than-predicted measurement of iron opacity at solar interior temperatures," *Nature*, vol. 517, pp. 56–59, Jan. 2015.

[21] R. G. Kraus, S. Root, R. W. Lemke, S. T. Stewart, S. B. Jacobsen, and T. R. Mattsson, "Impact vaporization of planetesimal cores in the late stages of planet formation," *Nature Geosci.*, vol. 8, p. 269, Mar. 2015.

[22] G. A. Rochau *et al.*, "ZAPP: The Z astrophysical plasma properties collaboration," *Phys. Plasmas*, vol. 21, no. 5, p. 056308, 2014, doi: 10.1063/1.4875330.

[23] B. M. Koval'chuk *et al.*, "Fast primary storage device utilizing a linear pulse transformer," *Russian Phys. J.*, vol. 40, no. 12, pp. 1142–1153, Dec. 1997, doi: 10.1007/BF02524302.

[24] A. A. Kim, B. M. Kovalchuk, E. V. Kumpjak, and N. V. Zoi, "0.75 MA, 400 ns rise time LTD stage," in *12th IEEE Int. Pulsed Power Conf. Dig. Tech. Papers*, vol. 2, Jun. 1999, pp. 955–958.

[25] M. G. Mazarakis and R. B. Spielman, "A compact, high-voltage e-beam pulser," in *12th IEEE Int. Pulsed Power Conf. Dig. Tech. Papers*, vol. 1, Jun. 1999, pp. 412–415.

[26] A. A. Kim and B. M. Kovalchuk, "High power direct driver for Z-pinch loads," in *Proc. 12th Symp. High Current Electron.*, G. Mesyats, B. Kovalchuk, and G. Remnev, Eds. Tomsk, Russia: Institute of High Current Electronics, 2000, p. 263.

[27] W. A. Stygar *et al.*, "Architecture of petawatt-class z-pinch accelerators," *Phys. Rev. Accel. Beams*, vol. 10, no. 3, p. 030401, Mar. 2007.

[28] A. A. Kim *et al.*, "Development and tests of fast 1-MA linear transformer driver stages," *Phys. Rev. Special Topics-Accel. Beams*, vol. 12, no. 5, p. 050402, May 2009. [Online]. Available: http://link.aps.org/doi/10.1103/PhysRevSTAB.12.050402

[29] R. M. Gilgenbach *et al.*, "MAIZE: A 1 MA LTD-driven Z-pinch at the University of Michigan," in *Proc. AIP Conf.*, Jan. 2009, vol. 1088, no. 1, pp. 259–262, doi: 10.1063/1.3079742.

[30] W. A. Stygar *et al.*, "Shaping the output pulse of a linear-transformer-driver module," *Phys. Rev. Special Topics-Accel. Beams*, vol. 12, no. 3, pp. 030402-1–030402-11, Mar. 2009. [Online]. Available: https://link.aps.org/doi/10.1103/PhysRevSTAB.12.030402

[31] M. G. Mazarakis *et al.*, "High current, 0.5-MA, fast, 100-ns, linear transformer driver experiments," *Phys. Rev. ST Accel. Beams*, vol. 12, p. 050401, May 2009, doi: 10.1103/PhysRevSTAB.12.050401.

[32] M. G. Mazarakis *et al.*, "High-current linear transformer driver development at Sandia National Laboratories," *IEEE Trans. Plasma Sci.*, vol. 38, no. 4, pp. 704–713, Apr. 2010.

[33] A. A. Kim, M. G. Mazarakis, V. I. Manylov, V. A. Vizir, and W. A. Stygar, "Energy loss due to eddy current in linear transformer driver cores," *Phys. Rev. ST Accel. Beams*, vol. 13, p. 070401, Jul. 2010, doi: 10.1103/PhysRevSTAB.13.070401.

[34] J. J. Leckbee *et al.*, "Commissioning and power flow studies of the 2.5-MeV Ursa Minor LTD," in *Proc. IEEE Int. Power Modulator High Voltage Conf. (IPMHVC)*, Jun. 2012, pp. 169–173.

[35] A. A. Kim *et al.*, "Square pulse linear transformer driver," *Phys. Rev. ST Accel. Beams*, vol. 15, p. 040401, Apr. 2012. [Online]. Available: https://link.aps.org/doi/10.1103/PhysRevSTAB.15.040401

[36] W. A. Stygar *et al.*, "Conceptual designs of two petawatt-class pulsed-power accelerators for high-energy-density-physics experiments," *Phys. Rev. ST Accel. Beams*, vol. 18, no. 10, p. 110401, Nov. 2015, doi: 10.1103/PhysRevSTAB.18.110401.

[37] Z. Lin *et al.*, "Design of a 5-MA 100-ns linear-transformer-driver accelerator for wire array Z-pinch experiments," *Phys. Rev. Accel. Beams*, vol. 19, no. 3, p. 030401, Mar. 2016. [Online]. Available: https://link.aps.org/doi/10.1103/PhysRevAccelBeams.19.030401

[38] A. A. Kim *et al.*, "Review of high-power pulsed systems at the Institute of High Current Electronics," *Matter Radiat. Extremes*, vol. 1, no. 4, pp. 201–206, 2016, doi: 10.1016/j.mre.2016.08.001.

[39] J. L. Giuliani *et al.*, "Plasma pinch research on University pulsed-power generators in the United States," *IEEE Trans. Plasma Sci.*, vol. 40, no. 12, pp. 3246–3264, Dec. 2012.

[40] D. D. Ryutov, M. S. Derzon, and M. K. Matzen, "The physics of fast Z pinches," *Rev. Mod. Phys.*, vol. 72, pp. 167–223, Jan. 2000. [Online]. Available: http://link.aps.org/doi/10.1103/RevModPhys.72.167

[41] A. B. Sefkow *et al.*, "Design of magnetized liner inertial fusion experiments using the Z facility," *Phys. Plasmas*, vol. 21, no. 7, pp. 072711-1–072711-15, Jul. 2014. [Online]. Available: http://scitation.aip.org/content/aip/journal/pop/21/7/10.1063/1.4890298

[42] R. D. McBride and S. A. Slutz, "A semi-analytic model of magnetized liner inertial fusion," *Phys. Plasmas*, vol. 22, no. 5, p. 052708, 2015, doi: 10.1063/1.4918953.

[43] R. D. McBride *et al.*, "Exploring magnetized liner inertial fusion with a semi-analytic model," *Phys. Plasmas*, vol. 23, no. 1, p. 012705, 2016, doi: 10.1063/1.4939479.

[44] S. A. Slutz *et al.*, "Scaling magnetized liner inertial fusion on Z and future pulsed-power accelerators," *Phys. Plasmas*, vol. 23, no. 2, p. 022702, 2016, doi: 10.1063/1.4941100.

[45] D. B. Sinars *et al.*, "Measurements of magneto-Rayleigh-Taylor instability growth during the implosion of initially solid Al tubes driven by the 20-MA, 100-ns Z facility," *Phys. Rev. Lett.*, vol. 105, no. 18, p. 185001, Oct. 2010.

[46] D. B. Sinars *et al.*, "Measurements of magneto-Rayleigh–Taylor instability growth during the implosion of initially solid metal liners," *Phys. Plasmas*, vol. 18, no. 5, p. 056301, 2011. [Online]. Available: http://scitation.aip.org/content/aip/journal/pop/18/5/10.1063/1.3560911

[47] R. D. McBride *et al.*, "Penetrating radiography of imploding and stagnating beryllium liners on the Z accelerator," *Phys. Rev. Lett.*, vol. 109, p. 135004, Sep. 2012. [Online]. Available: http://link.aps.org/doi/10.1103/PhysRevLett.109.135004

[48] R. D. McBride *et al.*, "Beryllium liner implosion experiments on the Z accelerator in preparation for magnetized liner inertial fusion," *Phys. Plasmas*, vol. 20, no. 5, pp. 056309-1–056309-10, May 2013, doi: 10.1063/1.4803079.

[49] M. R. Gomez *et al.*, "Demonstration of thermonuclear conditions in magnetized liner inertial fusion experiments," *Phys. Plasmas*, vol. 22, no. 5, p. 056306, 2015. [Online]. Available: http://scitation.aip.org/content/aip/journal/pop/22/5/10.1063/1.4919394

[50] K. J. Peterson *et al.*, "Electrothermal instability mitigation by using thick dielectric coatings on magnetically imploded conductors," *Phys. Rev. Lett.*, vol. 112, p. 135002, Apr. 2014. [Online]. Available: http://link.aps.org/doi/10.1103/PhysRevLett.112.135002

[51] T. J. Awe *et al.*, "Experimental demonstration of the stabilizing effect of dielectric coatings on magnetically accelerated imploding metallic liners," *Phys. Rev. Lett.*, vol. 116, p. 065001, Feb. 2016. [Online]. Available: http://link.aps.org/doi/10.1103/PhysRevLett.116.065001

[52] P. F. Knapp *et al.*, "Direct measurement of the inertial confinement time in a magnetically driven implosion," *Phys. Plasmas*, vol. 24, no. 4, p. 042708, 2017, doi: 10.1063/1.4981206.

[53] J. L. Giuliani and R. J. Commisso, "A review of the gas-Puff Z-pinch as an X-ray and neutron source," *IEEE Trans. Plasma Sci.*, vol. 43, no. 8, pp. 2385–2453, Aug. 2015.

[54] D. J. Ampleford *et al.*, "Dynamics of conical wire array Z-pinch implosions," *Phys. Plasmas*, vol. 14, no. 10, p. 102704, 2007, doi: 10.1063/1.2795129.

[55] S. V. Lebedev *et al.*, "Magnetic tower outflows from a radial wire array Z-pinch," *Monthly Notices Roy. Astronomical Soc.*, vol. 361, no. 1, pp. 97–108, 2005, doi: 10.1111/j.1365-2966.2005.09132.x.

[56] F. Suzuki-Vidal *et al.*, "Formation of episodic magnetically driven radiatively cooled plasma jets in the laboratory," *Astrophys. Space Sci.*, vol. 322, nos. 1–4, pp. 19–23, Aug. 2009, doi: 10.1007/s10509-009-9981-1.

[57] P.-A. Gourdain *et al.*, "Initial experiments using radial foils on the cornell beam research accelerator pulsed power generator," *Phys. Plasmas*, vol. 17, no. 1, p. 012706, 2010, doi: 10.1063/1.3292653.

[58] P.-A. Gourdain and C. E. Seyler, "Impact of the Hall effect on high-energy-density plasma jets," *Phys. Rev. Lett.*, vol. 110, p. 015002, Jan. 2013, doi: 10.1103/PhysRevLett.110.015002.

[59] T. Byvank, J. T. Banasek, W. M. Potter, J. B. Greenly, C. E. Seyler, and B. R. Kusse, "Applied axial magnetic field effects on laboratory plasma jets: Density hollowing, field compression, and azimuthal rotation," *Phys. Plasmas*, vol. 24, no. 12, p. 122701, Dec. 2017, doi: 10.1063/1.5003777.

[60] A. J. Harvey-Thompson *et al.*, "Quantitative analysis of plasma ablation using inverse wire array Z pinches," *Phys. Plasmas*, vol. 16, no. 2, p. 022701, 2009, doi: 10.1063/1.3077305.

[61] J. D. Hare *et al.*, "Anomalous heating and plasmoid formation in a driven magnetic reconnection experiment," *Phys. Rev. Lett.*, vol. 118, p. 085001, Feb. 2017, doi: 10.1103/PhysRevLett.118.085001.

[62] S. Ramo, J. R. Whinnery, and T. Van Duzer, *Fields and Waves in Communication Electronics*, 3rd ed. Hoboken, NJ, USA: Wiley, 1994.

[63] C. R. Paul, *Inductance: Loop and Partial*. Hoboken, NJ, USA: Wiley, 2011. [Online]. Available: https://books.google.com/books?id=3a7z8TzxaDMC

[64] O. A. Hurricane, "Optimized minimal inductance transmission line configuration for Z-pinch experiments," *J. Appl. Phys.*, vol. 95, no. 8, pp. 4503–4505, 2004, doi: 10.1063/1.1687986.

[65] E. M. Waisman and M. E. Cuneo, "Minimal inductance for axisymmetric transmission lines with radially dependent anode-cathode gap," *Phys. Rev. ST Accel. Beams*, vol. 12, p. 090401, Sep. 2009. [Online]. Available: https://link.aps.org/doi/10.1103/PhysRevSTAB.12.090401

[66] P. C. Campbell *et al.*, "Diagnostic and power feed upgrades to the MAIZE facility," *IEEE Trans. Plasma Sci.*, to be published, doi: 10.1109/TPS.2018.2858796.

[67] C. W. Mendel, Jr., "Conical Z-pinch gun," *J. Appl. Phys.*, vol. 42, no. 13, pp. 5483–5491, 1971, doi: 10.1063/1.1659968.

[68] C. M. Fowler and L. L. Altgilbers, "Magnetic flux compression: A tutorial and survey," *Eur. J. Electromagn. Phenomena*, vol. 3, no. 11, pp. 305–357, 2003. [Online]. Available: http://www.emph.com.ua/11/fowler1.htm

[69] R. D. McBride *et al.*, "Implementing and diagnosing magnetic flux compression on the Z pulsed power accelerator," Sandia Nat. Lab., Albuquerque, NM, USA, Tech. Rep. SAND2015-9860, 2015.

[70] F. F. Chen, *Introduction to Plasma Physics and Controlled Fusion*, 2nd ed. New York, NY, USA: Plenum, 1984.

[71] L. Brillouin, "A theorem of Larmor and its importance for electrons in magnetic fields," *Phys. Rev. J. Arch.*, vol. 67, pp. 260–266, Apr. 1945. [Online]. Available: https://link.aps.org/doi/10.1103/PhysRev.67.260

[72] C. W. Mendel, D. B. Seidel, and S. E. Rosenthal, "A simple theory of magnetic insulation from basic physical considerations," *Laser Part. Beams*, vol. 1, no. 3, pp. 311–320, 1983. [Online]. Available: https://doi.org/10.1017/S0263034600000379

[73] P. A. Miller and C. W. Mendel, Jr., "Analytic model of Applied-*B* ion diode impedance behavior," *J. Appl. Phys.*, vol. 61, no. 2, pp. 529–539, 1987, doi: 10.1063/1.338253.

[74] C. W. Mendel, Jr., and S. E. Rosenthal, "Modeling magnetically insulated devices using flow impedance," *Phys. Plasmas*, vol. 2, no. 4, pp. 1332–1342, 1995, doi: 10.1063/1.871345.

[75] W. A. Stygar *et al.*, "Analytic model of a magnetically insulated transmission line with collisional flow electrons," *Phys. Rev. ST Accel. Beams*, vol. 9, p. 090401, Sep. 2006. [Online]. Available: https://link.aps.org/doi/10.1103/PhysRevSTAB.9.090401

[76] M. E. Cuneo *et al.*, "Results of vacuum cleaning techniques on the performance of LiF field-threshold ion sources on extraction applied-B ion diodes at 1–10 TW," *IEEE Trans. Plasma Sci.*, vol. 25, no. 2, pp. 229–251, Apr. 1997.

[77] M. E. Cuneo, "The effect of electrode contamination, cleaning and conditioning on high-energy pulsed-power device performance," *IEEE Trans. Dielectr. Electr. Insul.*, vol. 6, no. 4, pp. 469–485, Aug. 1999.

[78] M. G. Haines, "The inverse skin effect," *Proc. Phys. Soc.*, vol. 74, no. 5, p. 576, 1959, doi: 10.1088/0370-1328/74/5/310.

[79] J. Greenly, C. Seyler, and X. Zhao, "Pulsed-power driven reconnection and the inverse skin effect," in *Proc. 56th Annu. Meeting APS Division Plasma Phys.*, vol. 59, 2014, p. 133. [Online]. Available: http://meetings.aps.org/link/BAPS.2014.DPP.JP8.97

[80] R. D. McBride *et al.*, "Displacement current phenomena in the magnetically insulated transmission lines of the refurbished Z accelerator," *Phys. Rev. ST Accel. Beams*, vol. 13, no. 12, p. 120401, Dec. 2010, doi: 10.1103/PhysRevSTAB.13.120401.

[81] E. Marx, "Verfahren zur Schlagprüfung von Isolatoren und anderen elektrischen Vorrichtungen," DE Patent 455 933, Oct. 12, 1923. [Online]. Available: https://patents.google.com/patent/DE455933C/en

[82] E. Marx, "Versuche über die Prüfung von Isolatoren mit Spannungsstößen," *Elektrotech. Z.*, vol. 25, pp. 652–654, 1924.

[83] H. Bluhm, *Pulsed Power Systems*. Berlin, Germany: Springer-Verlag, 2006, doi: 10.1007/3-540-34662-7.

[84] W. A. Stygar *et al.*, "55-TW magnetically insulated transmission-line system: Design, simulations, and performance," *Phys. Rev. Special Topics-Accel. Beams*, vol. 12, no. 12, p. 120401, 2009.

[85] C. A. Jennings *et al.*, "Circuit model for driving three-dimensional resistive MHD wire array Z-pinch calculations," *IEEE Trans. Plasma Sci.*, vol. 38, no. 4, pp. 529–539, Apr. 2010.

[86] C. A. Jennings *et al.*, "Simulations of the implosion and stagnation of compact wire arrays," *Phys. Plasmas*, vol. 17, no. 9, p. 092703, 2010, doi: 10.1063/1.3474947.

[87] C. A. Jennings *et al.*, "Integration of MHD load models with circuit representations the Z generator," Sandia National Lab., Albuquerque, NM, USA, Tech. Rep. SAND2015-9860, 2013.

[88] E. A. Madrid *et al.*, "Steady-state modeling of current loss in a posthole convolute driven by high power magnetically insulated transmission lines," *Phys. Rev. ST Accel. Beams*, vol. 16, p. 120401, Dec. 2013, doi: 10.1103/PhysRevSTAB.16.120401.

[89] R. D. McBride *et al.*, "Implosion dynamics and radiation characteristics of wire-array Z pinches on the Cornell Beam Research Accelerator," *Phys. Plasmas*, vol. 16, no. 1, p. 012706, 2009. [Online]. Available: http://scitation.aip.org/content/aip/journal/pop/16/1/10.1063/1.3054537

[90] M. K. Matzen *et al.*, "Pulsed-power-driven high energy density physics and inertial confinement fusion research," *Phys. Plasmas*, vol. 12, no. 5, p. 055503, 2005.

[91] M. E. Cuneo *et al.*, "Development and characterization of a Z-pinch-driven hohlraum high-yield inertial confinement fusion target concept," *Phys. Plasmas*, vol. 8, p. 2257, Dec. 2001.

[92] W. A. Stygar *et al.*, "Theoretical z-pinch scaling relations for thermonuclear-fusion experiments," *Phys. Rev. E, Stat. Phys. Plasmas Fluids Relat. Interdiscip. Top.*, vol. 72, no. 2, pp. 026404-1–026404-21, Aug. 2005.

[93] M. E. Cuneo *et al.*, "Characteristics and scaling of tungsten-wire-array z-pinch implosion dynamics at 20 MA," *Phys. Rev. E, Stat. Phys. Plasmas Fluids Relat. Interdiscip. Top.*, vol. 71, p. 046406, Apr. 2005, doi: 10.1103/PhysRevE.71.046406.

[94] D. B. Sinars *et al.*, "Radiation energetics of ICF-relevant wire-array Z pinches," *Phys. Rev. Lett.*, vol. 100, p. 145002, Apr. 2008, doi: 10.1103/PhysRevLett.100.145002.

[95] J. E. Bailey *et al.*, "Iron-plasma transmission measurements at temperatures above 150 eV," *Phys. Rev. Lett.*, vol. 99, no. 26, p. 265002, Dec. 2007.

[96] D. H. Dolan, M. D. Knudson, C. A. Hall, and C. Deeney, "A metastable limit for compressed liquid water," *Nature Phys.*, vol. 3, pp. 339–342, Mar. 2007.

[97] M. D. Knudson, D. L. Hanson, J. E. Bailey, C. A. Hall, J. R. Asay, and C. Deeney, "Principal Hugoniot, reverberating wave, and mechanical reshock measurements of liquid deuterium to 400 GPa using plate impact techniques," *Phys. Rev. B, Condens. Matter*, vol. 69, no. 14, p. 144209, 2004.

[98] J.-P. Davis, C. Deeney, M. D. Knudson, R. W. Lemke, T. D. Pointon, and D. E. Bliss, "Magnetically driven isentropic compression to multimegabar pressures using shaped current pulses on the Z accelerator," *Phys. Plasmas*, vol. 12, no. 5, pp. 056310-1–056310-7, May 2005.

[99] M. K. Matzen, "Z pinches as intense X-ray sources for high-energy density physics applications," *Phys. Plasmas*, vol. 4, no. 5, p. 1519, 1997.

[100] I. H. Mitchell *et al.*, "A high impedance mega-ampere generator for fiber z-pinch experiments," *Rev. Sci. Instrum.*, vol. 67, no. 4, pp. 1533–1541, 1996, doi: 10.1063/1.1146884.

[101] S. V. Lebedev *et al.*, "Physics of wire array Z-pinch implosions: Experiments at Imperial College," *Plasma Phys. Controlled Fusion*, vol. 47, no. 5A, p. A91, 2005, doi: 10.1088/0741-3335/47/5A/009.

[102] B. S. Bauer *et al.*, "The dense Z-pinch program at the University of Nevada, Reno," in *Proc. AIP Conf.*, 1997, vol. 409, no. 1, pp. 153–156. [Online]. Available: http://aip.scitation.org/doi/abs/10.1063/1.53879

[103] B. S. Bauer *et al.*, "Two-terawatt Zebra Z-pinch at the Nevada terawatt facility," in *12th IEEE Int. Pulsed Power Conf. Dig. Tech. Papers*, vol. 2, Jun. 1999, pp. 1045–1047.

[104] J. B. Greenly, J. D. Douglas, D. A. Hammer, B. R. Kusse, S. C. Glidden, and H. D. Sanders, "A 1 MA, variable risetime pulse generator for high energy density plasma research," *Rev. Sci. Instrum.*, vol. 79, no. 7, p. 073501, Jul. 2008, doi: 10.1063/1.2949819.

[105] D. B. Reisman *et al.*, "Pulsed power accelerator for material physics experiments," *Phys. Rev. Special Topics-Accel. Beams*, vol. 18, no. 9, p. 090401, Sep. 2015, doi: 10.1103/PhysRevSTAB.18.090401.

[106] D. A. Yager-Elorriaga *et al.*, "Development of a compact LTD pulse generator for X-ray backlighting of planar foil ablation experiments," in *Proc. Radiat. High Energy Density Plasmas Workshop*, South Lake Tahoe, NV, USA, Jun. 2013, p. 1.

[107] R. V. Shapovalov and R. B. Spielman, "Short-circuit test data of a new 2-LTD-brick X-pinch driver at the Idaho Accelerator Center," in *Proc. IEEE Pulsed Power Conf.*, May 2015, pp. 1–3.

[108] D. A. Yager-Elorriaga, A. M. Steiner, S. G. Patel, N. M. Jordan, Y. Y. Lau, and R. M. Gilgenbach, "Technique for fabrication of ultrathin foils in cylindrical geometry for liner-plasma implosion experiments with sub-megaampere currents," *Rev. Sci. Instrum.*, vol. 86, no. 11, p. 113506, 2015. [Online]. Available: http://scitation.aip.org/content/aip/journal/rsi/86/11/10.1063/1.4935838

[109] A. S. Safronova *et al.*, "Double and single planar wire arrays on University-Scale low-impedance LTD generator," *IEEE Trans. Plasma Sci.*, vol. 44, no. 4, pp. 432–440, Apr. 2016.

[110] A. M. Steiner *et al.*, "Determination of plasma pinch time and effective current radius of double planar wire array implosions from current measurements on a 1-MA linear transformer driver," *Phys. Plasmas*, vol. 23, no. 10, p. 101206, 2016, doi: 10.1063/1.4965241.

[111] D. A. Yager-Elorriaga, P. Zhang, A. M. Steiner, N. M. Jordan, Y. Y. Lau, and R. M. Gilgenbach, "Seeded and unseeded helical modes in magnetized, non-imploding cylindrical liner-plasmas," *Phys. Plasmas*, vol. 23, no. 10, p. 101205, Oct. 2016, doi: 10.1063/1.4965240.

[112] D. A. Yager-Elorriaga *et al.*, "Discrete helical modes in imploding and exploding cylindrical, magnetized liners," *Phys. Plasmas*, vol. 23, no. 12, p. 124502, 2016, doi: 10.1063/1.4969082.

[113] I. D. Smith, "Induction voltage adders and the induction accelerator family," *Phys. Rev. Special Topics-Accel. Beams*, vol. 7, no. 6, p. 064801, Jun. 2004, doi: 10.1103/PhysRevSTAB.7.064801.

[114] A. S. Chuvatin *et al.*, "Operation of a load current multiplier on a nanosecond mega-ampere pulse forming line generator," *Phys. Rev. ST Accel. Beams*, vol. 13, p. 010401, Jan. 2010. [Online]. Available: https://link.aps.org/doi/10.1103/PhysRevSTAB.13.010401

[115] V. L. Kantsyrev *et al.*, "Radiation sources with planar wire arrays and planar foils for inertial confinement fusion and high energy density physics research," *Phys. Plasmas*, vol. 21, no. 3, p. 031204, 2014, doi: 10.1063/1.4865367.

[116] W. A. Stygar, "Conceptual designs of four next-generation pulsed-power accelerators for high-energy-density-physics experiments," in *Proc. 1st Int. Conf. Matter Radiat. Extremes*, Chengdu, China, May 2016.

[117] D. V. Rose *et al.*, "Circuit models and three-dimensional electromagnetic simulations of a 1-MA linear transformer driver stage," *Phys. Rev. ST Accel. Beams*, vol. 13, p. 090401, Sep. 2010. [Online]. Available: https://link.aps.org/doi/10.1103/PhysRevSTAB.13.090401

[118] W. A. Stygar *et al.*, "Impedance-matched Marx generators," *Phys. Rev. Accel. Beams*, vol. 20, p. 040402, Apr. 2017. [Online]. Available: https://link.aps.org/doi/10.1103/PhysRevAccelBeams.20.040402

[119] P.-A. Gourdain, M. Evans, B. Foy, D. Mager, R. McBride, and R. Spielman. (2017). "HADES: A high amperage driver for extreme states." [Online]. Available: https://arxiv.org/abs/1705.04411

[120] J. Benford, J. A. Swegle, and E. Schamiloglu, *High Power Microwaves*, 2nd ed. New York, NY, USA: Taylor & Francis, 2007.

[121] C. Mangeant *et al.*, "Status on the sphinx generator based on microsecond current risetime LTD," in *Proc. Conf. Rec. 26th Int. Power Modulator Symp., High-Voltage Workshop*, May 2004, pp. 115–118. [Online]. Available: https://ieeexplore.ieee.org/document/1433520, doi: 10.1109/MODSYM.2004.1433520.

[122] M. Caron *et al.*, "High pulsed power at CEA DAM," in *Proc. 21st IEEE Pulsed Power Conf.*, Brighton, U.K., Jun. 2017. [Online]. Available: https://indico.cern.ch/event/572801/contributions/2578345/

[123] A. V. Shishlov *et al.*, "Double gas puff Z-pinch with axial magnetic field for K-shell radiation production," in *Proc. AIP Conf.*, 2002, vol. 651, no. 1, pp. 117–122, doi: 10.1063/1.1531294.

[124] A. G. Rousskikh, A. S. Zhigalin, V. I. Oreshkin, and R. B. Baksht, "Measuring the compression velocity of a Z pinch in an axial magnetic field," *Phys. Plasmas*, vol. 24, no. 6, p. 063519, Jun. 2017, doi: 10.1063/1.4986096.

[125] R. B. Baksht, V. I. Oreshkin, A. G. Rousskikh, and A. S. Zhigalin, "Energy balance in a Z pinch with suppressed Rayleigh–Taylor instability," *Plasma Phys. Controlled Fusion*, vol. 60, no. 3, p. 035015, 2018, doi: 10.1088/1361-6587/aaa79b.

[126] J. Woodworth, J. Alexander, F. Gruner, J. Blickem, H. Anderson, and M. Harden, "Low-inductance gas switches for linear transformer drivers," *Phys. Rev.*, vol. 12, no. 6, p. 060401, Jun. 2009. [Online]. Available: https://link.aps.org/doi/10.1103/PhysRevSTAB.12.060401

[127] J. R. Woodworth *et al.*, "New low inductance gas switches for linear transformer drivers," *Phys. Rev. Special Topics-Accel. Beams*, vol. 13, no. 8, p. 080401, Aug. 2010. [Online]. Available: https://link.aps.org/doi/10.1103/PhysRevSTAB.13.080401

[128] D. A. Yager-Elorriaga *et al.*, "Evolution of sausage and helical modes in magnetized thin-foil cylindrical liners driven by a Z-pinch," *Phys. Plasmas*, vol. 25, no. 5, p. 056307, 2018, doi: 10.1063/1.5017849.

[129] A. M. Steiner *et al.*, "The electro-thermal stability of tantalum relative to aluminum and titanium in cylindrical liner ablation experiments at 550 kA," *Phys. Plasmas*, vol. 25, no. 3, p. 032701, 2018, doi: 10.1063/1.5012891.

[130] J. C. Zier *et al.*, "Magneto-Rayleigh-Taylor experiments on a MegaAmpere linear transformer driver," *Phys. Plasmas*, vol. 19, no. 3, p. 032701, 2012, doi: 10.1063/1.3690088.

[131] V. J. Harper-Slaboszewicz, J. Leckbee, P. W. Lake, and A. L. McCourt, "Effect of rod material on the impedance behavior of small aspect ratio rod pinches," *IEEE Trans. Plasma Sci.*, vol. 42, no. 9, pp. 2207–2212, Sep. 2014.

[132] V. J. Harper-Slaboszewicz *et al.*, "Parallel operation of multiple closely spaced small aspect ratio rod pinches," *IEEE Trans. Plasma Sci.*, vol. 43, no. 1, pp. 422–432, Jan. 2015.

[133] Y. Maron *et al.*, "Pressure and energy balance of stagnating plasmas in z-pinch experiments: Implications to current flow at stagnation," *Phys. Rev. Lett.*, vol. 111, p. 035001, Jul. 2013. [Online]. Available: https://link.aps.org/doi/10.1103/PhysRevLett.111.035001

[134] D. Mikitchuk *et al.*, "Mitigation of instabilities in a Z-pinch plasma by a preembedded axial magnetic field," *IEEE Trans. Plasma Sci.*, vol. 42, no. 10, pp. 2524–2525, Oct. 2014.

[135] S. C. Bott *et al.*, "250 kA compact linear transformer driver for wire array z-pinch loads," *Phys. Rev. ST Accel. Beams*, vol. 14, p. 050401, May 2011, doi: 10.1103/PhysRevSTAB.14.050401.

[136] J. C. Valenzuela, G. W. Collins, IV, D. Mariscal, E. S. Wyndham, and F. N. Beg, "Study of instability formation and EUV emission in thin liners driven with a compact 250 kA, 150 ns linear transformer driver," *Phys. Plasmas*, vol. 21, no. 3, p. 031208, 2014, doi: 10.1063/1.4865225.

[137] R. E. Madden, S. C. Bott, G. W. Collins, IV, and F. N. Beg, "Investigation of carbon X-pinches as a source for point-projection radiography," *IEEE Trans. Plasma Sci.*, vol. 37, no. 3, pp. 433–437, Mar. 2009.

[138] J. R. Woodworth *et al.*, "Compact 810 kA linear transformer driver cavity," *Phys. Rev. ST Accel. Beams*, vol. 14, p. 040401, Apr. 2011. [Online]. Available: https://link.aps.org/doi/10.1103/PhysRevSTAB.14.040401

[139] S. A. Pikuz, T. A. Shelkovenko, and D. A. Hammer, "X-pinch. Part I," *Plasma Phys. Rep.*, vol. 41, no. 4, pp. 291–342, Apr. 2015, doi: 10.1134/S1063780X15040054.

[140] S. A. Pikuz, T. A. Shelkovenko, and D. A. Hammer, "X-pinch. Part II," *Plasma Phys. Rep.*, vol. 41, no. 6, pp. 445–491, Jun. 2015, doi: 10.1134/S1063780X15060045.

R. D. McBride (M'00) received the Ph.D. degree from Cornell University, Ithaca, NY, USA, in 2009, where he conducted experimental research on wire-array z-pinch implosions using the 1-MA COBRA pulsed-power facility.

From 2008 to 2016, he was with Sandia National Laboratories, Albuquerque, NM, USA, where he held appointments as a Staff Physicist and a Department Manager. At Sandia, he conducted research in nuclear fusion, radiation generation, and high-pressure material properties using the 25-MA Z pulsed-power facility. He is currently an Associate Professor with the Department of Nuclear Engineering and Radiological Sciences, University of Michigan, Ann Arbor, MI, USA. His current research interests include plasma physics, nuclear fusion, radiation generation, pulsed-power technology, plasma diagnostics, and the dynamics of magnetically driven, cylindrically imploding systems. His research is conducted primarily within the Plasma, Pulsed Power, and Microwave Laboratory, University of Michigan, which includes two linear transformer driver (LTD) facilities: MAIZE (∼1 MA, ∼100 ns) and BLUE (∼150 kA, ∼100 ns). Most recently, his research has been focused on both experimental and theoretical studies of magnetized liner inertial fusion (MagLIF). MagLIF is presently one of the United States' three mainline approaches to studying controlled inertial confinement fusion in the laboratory.

W. A. Stygar, photograph and biography not available at the time of publication.

M. E. Cuneo, photograph and biography not available at the time of publication.

D. B. Sinars (M'04–SM'17) received the B.S. degree from the University of Oklahoma, Norman, OK, USA, in 1996, and the Ph.D. degree from Cornell University, Ithaca, NY, USA, in 2001.

He is currently the Senior Manager for the Radiation and Fusion Physics Group, Sandia National Laboratories, Albuquerque, NM, USA. He is responsible for leading and coordinating Sandia's research activities in the Inertial Confinement Fusion program as Sandia's Deputy ICF Executive. His group's research is primarily centered around experiments using the 80-TW, 20 MJ Z pulsed power facility, as well as the adjacent multi-kJ, 2-TW Z-Beamlet laser facility. He leads the development and application of intense X-ray and fusion neutron sources driven by magnetic compression, as well as the advanced X-ray imaging and spectroscopy diagnostics needed to support this research.

Dr. Sinars is a Fellow of the American Physical Society. He received the 2007 IEEE Nuclear and Plasma Sciences Society Early Achievement Award, the 2011 Department of Energy Early Career Research Program Award, and the 2011 Presidential Early Career Award for Scientists and Engineers (PECASE).

M. G. Mazarakis (M'75–LM'08) holds the bachelor's *(summa cum laude)* and master's degrees in physics from the National University of Athens, Greece, a Ph.D. degree in nuclear physics from the University of Paris (Sorbonne), Paris, France, and a second Ph.D. degree in physics from the University of Pennsylvania, Philadelphia, PA, USA.

He did post-graduate work at Princeton Physics Department, Princeton, NJ, USA, where he had the opportunity to take advance physics courses with the Nobel laureates professors J. W. Cronin and V. L. Fitch and in the University of Pennsylvania with R. J. Schrieffer. He is Principal Member of the Technical Staff in the Pulsed Power Center, Sandia National Laboratories, Albuquerque, NM, USA. Currently is the Lead Project Physicist of the high-power semiconductor diodes experiments as applied to high energy accelerators. He has done pivotal research in nuclear physics and technology, nuclear astrophysics, particle beam physics, accelerator development, z-pinch physics, and magnetic and inertial fusion, and developed and successfully directed for several years the Sandia radiographic program. Before joining Sandia National Laboratories, he was Research Physicist at the Argonne National Laboratory, Lemont, IL, USA, from 1976 to 1981, and before that, was the Vice President and the Director of the Experimental Program at the Fusion Energy Corporation (FEC), Princeton, NJ, USA. He has published over 200 papers in referee magazines and conferences.

Dr. Mazarakis is a member of the Executive Committee of the IEEE Power Modulation Conference and the Executive Committee of Plasma Sciences and Applications (ICOPS). He is also a member of the American Physical Society and the Divisions of Plasma Physics and Particle Beams.

J. J. Leckbee, photograph and biography not available at the time of publication.

M. E. Savage, photograph and biography not available at the time of publication.

B. T. Hutsel, photograph and biography not available at the time of publication.

J. D. Douglass, photograph and biography not available at the time of publication.

M. L. Kiefer received the B.A. degree from Augustana College, Rock Island, IL, USA, in 1978, and the Ph.D. degree in theoretical nuclear physics from Iowa State University, Ames, IA, USA in 1983.

He was with the Pulsed Power Sciences Center, Sandia National Laboratories, Albuquerque, NM, USA, where he was involved in pulsed power and electromagnetic effects modeling and simulation tools, developing high-performance computing and visualization capabilities, and managing technical programs and personnel in the areas of electromagnetic effects and pulsed power. He was the Lead Scientist with the Joint IED Defeat Organization, Washington, DC, USA, where he was involved in the improvised explosive device neutralization effort supporting the war efforts in Iraq and Afghanistan. He is currently with the National Nuclear Security Administration Defense Programs Science Council, Washington, DC, USA, where is involved in a temporary assignment.

B. V. Oliver (M'03–F'17) was born in Berkeley, CA, USA. He received the B.S. degree in physics from the University of California, San Diego, CA, USA, in 1988, and the M.S. and Ph.D. degrees in theoretical plasma physics from Cornell University, Ithaca, NY, USA, in 1991 and 1994, respectively.

He is currently a Senior Manager with the Radiation and Electrical Sciences Center, Sandia National Laboratories, Albuquerque, NM, USA, where he leads the Radiation Effects Sciences and Applications Group. He is involved in the development and application of intense radiation sources for use in the study of radiation effects on devices, circuits, and components subject to hostile radiation environments. This includes the development of large-scale radiation transport and plasma simulation codes, as well as high-fluence radiation experimental platforms. His current research interests include theory and simulation of intense electron and ion beam generation and propagation, magnetohydrodynamics (MHD) and electron Hall MHD, Z-pinches, X-ray radiography, radiation effects, and intense electromagnetic pulse.

Dr. Oliver is a member of the American Physical Society. He serves on the IEEE Nuclear Plasma Sciences Society Committee, the Pulsed-Power Sciences and Technology Committee, the Plasma Science and Applications Committee, and the International High Power Particle Beams Committee.

G. R. Laity (S'09–M'13) received the B.S. degree in physics and the M.S. and Ph.D. degrees in electrical engineering from Texas Tech University, Lubbock, TX, USA, in 2008, 2010, and 2013, respectively.

He is presently an Experimental Physicist at Sandia National Laboratories, Albuquerque, NM, USA, where he serves as Principal Investigator at the Sandia Z Facility, the world's largest pulsed power device, in the areas of vacuum power flow physics, z-pinch radiation sources, and magneto-inertial fusion experiments. He is an Adjunct Faculty Member with the Center for Pulsed Power and Power Electronics, Texas Tech University, and for a brief period served as a Visiting Scientist with the U.S. Air Force Research Laboratory, Albuquerque, NM, USA. He has contributed to a variety of technical topics including: pulsed power accelerator technology, high energy density physics, vacuum insulator flashover, high power electromagnetics, vacuum arc ion sources, and optical/plasma diagnostic development.

Dr. Laity is an Active Member of the IEEE and the American Physical Society and was elected to the AdCom of the IEEE Dielectrics and Electrical Insulation Society in 2018. He was General Conference Chair of the 2018 IEEE International Power Modulator and High Voltage Conference and serves on the technical program committees of multiple international conferences.

M. R. Gomez (M'06) received the Ph.D. degree in nuclear engineering and radiological sciences from the University of Michigan, Ann Arbor, MI, USA, in 2011.

He is currently a Staff Member with Sandia National Laboratories, Albuquerque, NM, USA, where he is involved in inertial confinement fusion and high-energy-density science on the Z machine. His current research interests include magnetoinertial fusion sources, power flow and current coupling in large pulsed-power drivers, and X-ray diagnostic development.

D. A. Yager-Elorriaga, photograph and biography not available at the time of publication.

S. G. Patel, photograph and biography not available at the time of publication.

B. M. Kovalchuk, photograph and biography not available at the time of publication.

A. A. Kim, photograph and biography not available at the time of publication.

P.-A. Gourdain, photograph and biography not available at the time of publication.

S. N. Bland, photograph and biography not available at the time of publication.

S. Portillo, photograph and biography not available at the time of publication.

S. C. Bott-Suzuki (M'07) received the M.Phys. degree in chemical physics and the Ph.D. degree in physics from Sheffield University, Sheffield, U.K., in 1999 and 2004, respectively.

He was a Post-Doctoral Researcher with the Imperial College London, London, U.K. before moving to the University of California San Diego (UCSD), San Diego, CA, USA, in 2006. He is currently an Associate Research Scientist with the Center for Energy Research, UCSD, and a Visiting Professor with Cornell University, Ithaca, NY, USA. He was involved in the experimental analysis of plasmas generated using pulsed-power techniques and their application in inertial fusion, basic plasma physics, and laboratory astrophysics. He has authored or co-authored over 60 journal papers.

Dr. Bott-Suzuki served as the Co-Chair for the 9th International Conference on Dense Z-Pinches, Napa, CA, USA, in 2014. He has also served in various roles for the ICOPS conference series and a Guest Editor for the Fourth and Fifth Special Issues on Z-Pinch Plasmas published in the IEEE TRANSACTIONS ON PLASMA SCIENCE.

F. N. Beg, photograph and biography not available at the time of publication.

Y. Maron, photograph and biography not available at the time of publication.

R. B. Spielman, photograph and biography not available at the time of publication.

D. V. Rose, photograph and biography not available at the time of publication.

D. R. Welch, photograph and biography not available at the time of publication.

J. C. Zier received the B.S.E. and M.S. degrees in nuclear engineering and radiological sciences (NERS), the M.S.E. degree in electrical engineering, and the Ph.D. degree in NERS (plasma physics) from the University of Michigan (UM), Ann Arbor, MI, USA, in 2005, 2007, 2008, and 2010, respectively.

He was an undergraduate student intern with Sandia National Laboratories, Albuquerque, NM, USA, and Lawrence Livermore National Laboratory, Livermore, CA, USA, where he was involved in hydrodynamic and inertial confinement fusion simulations. He was with the UM, where he was involved in the design and construction of a 100-GW linear transformer driver (LTD) facility, and also conducted the initial dynamic liner experiments using the new facility. In 2010, he joined the Pulsed Power Physics Branch, NRL, Washington, DC, USA, as a Research Physicist. He is currently a Principal Investigator with the NRL's Advanced Radiographic Sources Research Program using the mercury pulsed-power facility. His current research interests include pulsed-radiographic diodes, radiation effects sources, active detection of special nuclear materials, Z-pinch ablation dynamics, contact resistance, advanced pulsed power and LTDs, image processing, liner evolution, and magneto-Rayleigh–Taylor instability.

J. W. Schumer (M'99–SM'12) received the B.S. degree in nuclear engineering from the University of Missouri, Rolla, MO, USA, in 1992, and the M.S. and Ph.D. degrees from the University of Michigan in 1994 and 1997, respectively.

He is the Branch Head and a Senior Research Physicist in the Pulsed Power Physics Branch, Plasma Physics Division, Naval Research Laboratory (NRL), Washington, DC, USA, primarily involved in the research areas of plasma physics and nuclear science. Since coming to NRL in 1997, he has earned a reputation as being an Expert Computational Physicist by analytically and computationally modeling plasmas, vacuum and plasma-filled diodes and electron powerflow, plasma-wave interactions in microwave structures, and charged particle beams using magnetohydrodynamic, kinetic (continuum and particle-in-cell), and Monte-Carlo methods. As the Branch Head, he leads experimental and theoretical efforts across a wide area of pulsed power applications including nuclear weapons effects simulation, active detection of nuclear materials, advanced energetics, electromagnetic railgun, high-powered microwave sources, and modeling of nuclear effects in the atmosphere.

Dr. Schumer is the General Chair of the IEEE ICOPS-Beams 2014 conference, the Chair-Elect of the IEEE NPSS Plasma Science Applications Committee, and a Panelist on various senior DOE and DoD Advisory Boards for stockpile stewardship and radiation effect sciences.

J. B. Greenly, photograph and biography not available at the time of publication.

A. M. Covington, photograph and biography not available at the time of publication.

A. M. Steiner (S'10–M'17) received the B.S. degree in nuclear engineering and physics from North Carolina State University, Raleigh, NC, USA, in 2010, the M.S. degree in nuclear engineering and the Ph.D. degree in nuclear engineering and radiological sciences from the University of Michigan (UM), Ann Arbor, MI, USA, in 2012 and 2016, respectively.

He is currently a Senior Electrical Engineer with the Skunk Works Team, Lockheed Martin Aeronautics Company, Palmdale, CA, USA. He has been involved in pulsed power driver development for high-density plasma sources and large magnetic field generation from high-temperature superconductors.

P. C. Campbell, photograph and biography not available at the time of publication.

S. M. Miller, photograph and biography not available at the time of publication.

J. M. Woolstrum, photograph and biography not available at the time of publication.

N. B. Ramey, photograph and biography not available at the time of publication.

A. P. Shah, photograph and biography not available at the time of publication.

B. J. Sporer, photograph and biography not available at the time of publication.

N. M. Jordan (S'05–M'13) received the B.S.E., M.S.E., and Ph.D. degrees in nuclear engineering (with a minor in plasma physics) from the University of Michigan (UM), Ann Arbor, MI, USA, in 2002, 2004, and 2008, respectively.

He was with Cybernet Systems, Ann Arbor, MI, USA, where he was involved in microwave vehicle stopping technology. He became an Assistant Research Scientist with the Plasma, Pulsed Power, and Microwave Laboratory, UM, in 2013. His current research interests include high-power microwave devices, pulsed power, laser ablation, Z-pinch physics, and plasma discharges.

Y. Y. Lau (M'98–SM'06–F'08) received the B.S., M.S., and Ph.D. degrees in electrical engineering from the Massachusetts Institute of Technology, Cambridge, MA, USA, in 1968, 1970, and 1973, respectively.

He was involved in electron beams, coherent radiation sources, plasmas, and discharges. He is currently a Professor with the Department of Nuclear Engineering and Radiological Sciences, University of Michigan, Ann Abor, MI, USA. He has authored or co-authored more than 250 refereed publications. He holds 11 patents. His current research interests include electrical contacts, heating phenomenology, high-power microwave sources, and magneto-Rayleigh–Taylor instabilities.

Dr. Lau became a Fellow of the American Physical Society in 1986. He served as an Associate Editor (thrice) for *Physics of Plasmas* from 1994 to 2005. He was a recipient of the 1999 IEEE Plasma Science and Applications Award and the 2017 IEEE John R. Pierce Award for Excellence in Vacuum Electronics.

R. M. Gilgenbach (M'74–F'06–LF'15) received the B.S. and M.S. degrees from the University of Wisconsin–Madison, Madison, WI, USA, in 1972 and 1973, respectively, and the Ph.D. degree in electrical engineering from Columbia University, New York, NY, USA, in 1978.

He was a Technical Staff Member with the Bell Telephone Laboratories, Holmdel, NJ, USA. From 1978 to 1980, he was with the Naval Research Laboratory, Washington, DC, USA, where he was involved in gyrotron research, and the Oak Ridge National Laboratory, Oak Ridge, TN, USA, where he performed the first electron cyclotron heating experiments on a tokamak plasma. In 1980, he joined the University of Michigan (UM), Ann Abor, MI, USA, as a Faculty member and the Founder of the Plasma, Pulsed Power, and Microwave Laboratory, UM. He has supervised 50 graduated Ph.D. students. He is currently the Chihiro Kikuchi Collegiate Professor with the Nuclear Engineering and Radiological Sciences Department, UM.

Dr. Gilgenbach is a Fellow of the American Physical Society, the Division of Plasma Physics, and the American Nuclear Society. He served as the IEEE PSAC Chair from 2007 to 2008. He was a recipient of the 1997 IEEE Plasma Sciences and Applications Committee Award and the 2017 IEEE Peter Haas Pulsed Power Award. He was an Associate Editor of *Physics of Plasmas*.